

---

# **Investigation of stratospheric variability from intra-decadal to seasonal time scales**

**Hung Duy Sinh Cai**

---



München 2015



---

# **Investigation of stratospheric variability from intra-decadal to seasonal time scales**

**Hung Duy Sinh Cai**

---

Dissertation  
an der Fakultät für Physik  
der Ludwig-Maximilians-Universität  
München

vorgelegt von  
Hung Duy Sinh Cai  
aus Hongkong

München 2015

Erstgutachter: Prof. Dr. Martin Dameris

Zweitgutachter: Prof. Dr. Bernhard Mayer

Datum der mündlichen Prüfung: 04.08.2015

Wer A sagt, der muß nicht B sagen. Er kann auch erkennen, daß A falsch war.

Bertold Brecht



# Contents

<b>Zusammenfassung</b>	<b>ix</b>
<b>Abstract</b>	<b>xi</b>
<b>1 Introduction</b>	<b>1</b>
1.1 Scientific Background . . . . .	3
1.1.1 Atmospheric Waves . . . . .	3
1.1.2 Extra-Tropical Variability . . . . .	7
1.1.3 Tropical Variability . . . . .	8
1.2 Thesis Motivation and Objectives . . . . .	12
<b>2 Model description and Data</b>	<b>15</b>
2.1 MiKlip Decadal Prediction System . . . . .	15
2.1.1 MPI-ESM . . . . .	15
2.1.2 MiKlip Simulation Setup . . . . .	16
2.2 The EMAC Model System . . . . .	17
2.2.1 ECHAM5 . . . . .	18
2.2.2 MESSy . . . . .	18
2.2.3 Simulation Setups with EMAC . . . . .	18
2.2.4 Differences between MPI-ESM and EMAC . . . . .	23
2.3 Reanalysis ERA-Interim . . . . .	24
<b>3 Intra-Decadal Variability</b>	<b>27</b>
3.1 PSA of ERA-Interim . . . . .	28
3.2 Power of MiKlip Simulations . . . . .	31
3.3 Power of EMAC Simulations . . . . .	35
3.4 Summary and Discussion of Decadal PSA . . . . .	35
<b>4 Intra-Seasonal Variability</b>	<b>39</b>
4.1 Tropical Variability . . . . .	39
4.1.1 The QBO . . . . .	39
4.1.2 PSA following Wheeler et al. . . . .	41
4.1.3 Discussion of the QBO . . . . .	46

4.1.4	The SAO . . . . .	47
4.1.5	Discussion of the SAO . . . . .	49
4.1.6	Summary and Discussion of Tropical Variability . . . . .	51
4.2	Antarctic Polar Vortex Variability . . . . .	54
4.2.1	REF Climatologies . . . . .	54
4.2.2	Sea Surface Temperature (SST) Sensitivities . . . . .	57
4.2.3	Discussion of SST Sensitivities . . . . .	61
4.2.4	Gravity Wave Sensitivity . . . . .	64
4.2.5	Discussion of Gravity Wave Sensitivities . . . . .	74
4.2.6	Resolution Sensitivity . . . . .	78
4.2.7	Discussion of Resolution Sensitivities . . . . .	88
<b>5</b>	<b>Summary and Conclusions</b>	<b>93</b>
<b>A</b>	<b>Methods of Power Spectral Analysis (PSA)</b>	<b>101</b>
A.1	Hayashi Method . . . . .	101
A.2	Wheeler Method . . . . .	102
<b>B</b>	<b>Linear Least Square Regression Model</b>	<b>105</b>
<b>C</b>	<b>The Transformed Eulerian Mean (TEM) Framework</b>	<b>107</b>
	<b>Bibliography</b>	<b>109</b>

# Zusammenfassung

Die Klimavorhersage für dekadische Zeitskalen ist ein relativ neues wissenschaftliches Feld der Atmosphärenforschung. Es ist allgemeiner Konsens, dass die Stratosphäre einen wesentlichen Einfluss auf das bodennahe Klima der Erde hat. Jedoch sind hierfür die zugrunde liegenden Mechanismen teilweise unbekannt und deren Beschreibung unvollständig. Insbesondere bedarf es weitergehender Untersuchungen hinsichtlich der Rolle der Stratosphäre und deren Variabilität auf dekadischen Zeitebenen.

Ein wichtiges Charakteristikum der Atmosphärendynamik ist die Variabilität. Die vorliegende Arbeit hat zum Ziel, das Verständnis der atmosphärischen Variabilität auf intra-dekadischen wie auch intra-saisonalen Zeitskalen zu verbessern. Die Variabilität der Atmosphäre auf dekadischen Zeithorizonten wird anhand einer neuen Methode, basierend auf der sogenannten "power spectral analysis" (PSA), untersucht. Ergebnisse numerischer Simulationen des MiKlip (Mittelfristige Klimaprognosen)-Systems und des EMAC (ECHAM MESSy Atmospheric Chemistry) Modells werden Reanalysedaten gegenübergestellt, um Schwächen in den Modellsystemen aufzudecken und zu erklären.

Anhand der dekadischen PSA ist festzustellen, dass die größten Abweichungen zwischen Modellen und Reanalysen in der tropischen und südpolaren Region der Stratosphäre auftreten. Die Modellabweichungen in den Tropen sind darauf zurückzuführen, dass die Antriebe der Hauptvariabilitätsmuster der äquatorialen Region, wie zum Beispiel die Quasi-Biennalen-Oszillation (QBO) und die halbjährliche Oszillation (engl. Semi-Annual-Oscillation; SAO) nicht adäquat simuliert werden können. Insbesondere kann gezeigt werden, dass eine hohe vertikale Modellauflösung (< 1 km) von Nöten ist, um die relevanten atmosphärendynamischen Prozesse wiederzugeben, die die QBO bestimmen.

Die aus der dekadischen PSA identifizierten südhemisphärischen Modelldefizite beruhen auf einem zu schwachen antarktischen Winter- und Frühjahrs-polarwirbel. Um die Ursachen näher zu beleuchten, wurden eine Reihe von Sensitivitätsstudien durchgeführt, und zwar hinsichtlich der Meeresoberflächentemperatur, der Schwerewelleneffekte und der Modellauflösung.

Aus diesen Sensitivitätsstudien folgernd kann gezeigt werden, dass der zu schwach simulierte südhemisphärische Polarwirbel auf eine verstärkte planetare Wellenaktivität zurückzuführen ist, wohingegen im Frühjahr Modelldefizite einer verfrühten Umstellung von Winter- zu Frühjahrsbedingungen geschuldet sind. Es gibt klare Hinweise darauf, dass kleinskalige, parametrisierte Schwerewellen signifikant zu den festgestellten Modellschwächen beitragen können.

Allgemein ist festzustellen, dass die hier analysierten numerischen Modelle qualitativ in der Lage sind die dekadische Variabilität wiederzugeben. Allerdings muss hierfür eine ausreichend hohe, vertikale Auflösung berücksichtigt werden, um beispielsweise relevante Prozesse der Tropen zu erfassen. Des Weiteren bedarf es weiterer Anstrengungen hinsichtlich der Parametrisierung von kleinskaligen Scherewellen in Klimamodellen und speziell deren Effekte auf planetare Wellen, um die Simulationsergebnisse im Vergleich zu den Beobachtungen zu verbessern. Im Vordergrund solcher Arbeiten sollte die Wechselseitige Beeinflussung von planetaren Wellen und kleinskaligen Scherewellen stehen, die bisher nur unzureichend berücksichtigt werden.

# Abstract

Decadal prediction is a new scientific field emerging in the last recent years. It is generally accepted that the stratosphere can distinctly influence the climate state at the surface and relevant processes can be attributed to dynamical processes of the atmosphere. However, the exact underlying mechanisms are still ambiguous and in particular at decadal time scales the role of the stratosphere need to be clarified.

Variability is a key characteristic atmospheric dynamics. This thesis contributes to a better understanding of atmospheric variability on intra-decadal and intra-seasonal time scales. The atmospheric variability on a decadal time scales is investigated by means of a novel approach of power spectral analysis (PSA). Numerical simulations of the MiKlip (Mittelfristige Klimaprognosen; engl. decadal climate predictions) system and EMAC (ECHAM MESSy Atmospheric Chemistry) model are compared to reanalysis data sets in order to identify weaknesses of these model systems.

The decadal PSA shows that the most pronounced deviations of variability between numerical models and reanalysis data arise in the tropical region and the Southern hemispheric polar region of the stratosphere. The tropical issue can be addressed to challenges of numerical models representing the driving mechanisms of the leading variability patterns in the equatorial region such as the QBO (Quasi-Biennial Oscillation) and SAO (Semi-Annual Oscillation). In particular it is demonstrated that only models with a high vertical resolution (minimum  $< 1$  km) are capable of capturing the dynamical processes relevant to drive the QBO.

The model deficits in the Southern hemisphere identified by means of the decadal PSA, arises from a too weak simulated Antarctic polar vortex during winter and spring terms. In order to investigate the underlying causes in more detail a set of sensitivity studies were carried out, concerning the sea surface temperature, the gravity wave parameterisation and the model resolution.

Inferred from these sensitivity studies it is demonstrated that during Austral winter the simulated weak polar vortex arises from an enhanced planetary wave activity, whereas in the spring term model deficits representing the polar vortex can be attributed to a premature transitioning of winter to spring conditions. There are clear indications that the effects of small scale parameterised gravity waves significantly contribute to the detected model deficits.

Generally it can be stated that the here analysed numerical model systems are able to qualitatively capture decadal variability. However, for this purpose the model systems need

to consider an adequately high vertical resolution in order to cover the relevant processes for tropical stratospheric variability. Moreover with regard to the parameterisation of small scale gravity waves in numerical global models further research efforts are required. In particular the interaction between small scale gravity waves and planetary waves have to be considered in more detail, which has not been sufficiently done so far.

# Kapitel 1

## Introduction

Weather and climate activities substantially affect humankind. Increased hurricane activity in the North Atlantic basin since the late 1990's (Goldenberg et al., 2001), the recent prolonged Southern-United-States droughts (Svoboda et al., 2002; Monitor, 2014) and extreme events like the 2003 and 2010 European heat waves (Miralles et al., 2014) have significant environmental, social and economical implications in the near term. The need for reliable information about the weather as well as 'short term climate trends', in particular at a decadal time scale is rapidly increasing.

For this purpose the Federal Ministry of Education and Research in Germany (BMBF) launched the research programme 'MiKlip' (Mittelfristige Klimaprognosen; decadal climate predictions). The main objective of MiKlip is to set up a model system that can satisfy the requirements for a reliable decadal forecast on climate and weather and extreme weather events. Decadal climate predictions are a relative new research field emerging in the last recent years (e.g. Taylor et al., 2012; Pohlmann et al., 2013). Consequently new scientific questions are raised. For instance, it has to be clarified which processes are relevant for a realistic representation of decadal climate. Those identified processes then have to be understood and evaluated as a part of numerical prediction systems.

To date it is generally accepted that numerical models necessarily need the information of the stratosphere (the region of the atmosphere between about 10 and 50 km altitude) in order to provide a qualitatively good representation of the troposphere (e.g. Boville, 1984; Andrews et al., 1987; Runde, 2012; Holton and Hakim, 2013). For example Baldwin and Dunkerton (2001) demonstrated, that stratospheric signals can propagate downward through the entire atmosphere and eventually reach the ground, which in turn has implications on the weather of the Earth's surface. This finding illustrates quite well the direct influence of the stratosphere on the troposphere, but the underlying processes of which are still not fully understood.

Furthermore it has been shown that model simulations can considerably improve their seasonal and inter-annual predictive skill in the troposphere, if stratospheric processes are taken into account (e.g. Sigmond et al., 2013). For example a seasonal model simulation with a higher vertical stratospheric resolution can significantly reproduce a more precise seasonal temperature forecast compared to models with a coarser vertical stratospheric

resolution (Roff et al., 2011). However, on intra-decadal time scales the contribution of the middle atmosphere (the region of the atmosphere between about 10 and 100 km altitude) and in particular the stratosphere is still subject of current research and scientific discussions.

One aspect of the strong tropospheric-stratospheric coupling can be explained by dynamical processes. A characteristic component of the dynamics is the two way interaction of atmospheric waves and the mean flow. Breaking and dissipation of vertical propagating waves transfer their momentum to the mean flow, which also can be considered as a mean systematic force acting on the mean flow (Andrews et al., 1987; Holton et al., 2003; Holton and Hakim, 2013). But on the other hand, the mean flow also has a great impact on wave propagation, breaking and dissipation itself. A well known example for this is the 'Charney and Drazin' criterion, which states that large scale planetary waves only can propagate upward in westerlies (Charney and Drazin, 1961). So this two way interaction can add a substantial portion of variability and structure to atmospheric general circulation.

This variability is often referred as internal dynamical variability (e.g. Holton and Mass, 1976; Scott and Haynes, 2000; Yoden et al., 2002). Therefore internal dynamical variability is strongly characterised by a large set of different wave types. Their temporal scales can span from a few minutes to weeks and up to months with corresponding spatial extent encompassing sub-regional (meters) and global scales (thousands of kilometers). Due to feasibility and computational limits global general circulation models (GCM) are typically run with a horizontal resolution coarser than 100 km and as a consequence a considerable part of the wave spectra cannot contribute to internal variability. In order to preserve a reasonable mean climate state thesees unresolved waves have to be parameterised (e.g. Fritts and Alexander, 2003; Manzini and McFarlane, 1998; Hines, 1997a,b). For example atmospheric gravity waves are typically smaller than the common horizontal resolution of GCMs and therefore are subject of such parameterisation (CCMVal, 2010). Without consideration of parameterised small scale gravity waves, models can be challenged by some serious problems. For instance models can suffer from a too cold Southern hemispheric polar vortex during winter terms, also known as the so called cold-pole bias (CCMVal, 2010; Austin et al., 2003). Gravity wave drag in the middle atmosphere can significantly warm the stratospheric winter polar vortex and counteracts the cold-pole bias (Boville, 1984; Garcia and Boville, 1994). Going to lower latitudes, in particular the tropics, gravity waves are believed to contribute a considerable portion of the necessary momentum to force middle atmospheric oscillation pattern, such as the Quasi-Biennial Oscillation (QBO) or Semi-Annual Oscillation (SAO) (Kawatani et al., 2010a). Further it is discussed that the QBO is an important factor in forecasting the seasonal variability of the North Atlantic region, which in turn has a potential to enhance the predictive skill of numerical models on the decadal time scale (Scaife et al., 2014; Smith et al., 2012).

Our understanding of unresolved waves, in particular their driving mechanisms and effects on the general atmospheric circulation is incomplete and therefore models are challenged by a substantial uncertainty concerning internal variability, i.e. the interaction between resolved and unresolved waves and in particular their quantitative implications to the mean flow is not well understood and strongly varies between different models (Cohen

et al., 2013, 2014). Further gravity wave spectra, which are crucial for a qualitative as well as a quantitative estimation of the effects of gravity waves, are very little understood due to the small number of available observations (Fritts and Alexander, 2003).

Besides internal variability, 'external' or 'deterministic' variability plays an important role in the atmospheric state. This kind of variability results from forces, which are determined by processes originating 'outside' the atmospheric domain and thus could be considered as 'external'. For example the eleven year solar cycle (or solar activity cycle), a natural low frequency fluctuation of the intensity of solar irradiance, can alter the stratospheric ozone concentrations which in turn have significant implications for the atmospheric circulation (Dameris et al., 2006; Holton et al., 2003). Moreover significant tropical Pacific ocean anomalies occurring during the phases of the El Niño / Southern Oscillation phenomenon (ENSO) also have strong impacts on the atmospheric structure (Garny et al., 2009; Garny, 2010; Cagnazzo et al., 2009).

Nonetheless variability is a key parameter in the description of the dynamics of our climate system. For decadal forecast model systems, the internal as well as external variability is mandatory to be captured and their corresponding underlying processes have to be understood and implemented. Further the role of the stratosphere for predictions on the decadal time scale still remains an open question that requires further efforts and a deeper research.

## 1.1 Scientific Background

### 1.1.1 Atmospheric Waves

Internal variability of an atmospheric field can be determined by the underlying wave spectrum (e.g. Hayashi, 1971, 1979; Dell'Aquila et al., 2005). Atmospheric waves are periodic motions of Earth's atmosphere which have various spatial (from meters to thousands of kilometers) and temporal scales (from minutes to months). Their immediate effects on the atmospheric fields, e.g. wind, temperature, pressure or density can be identified as temporal and spatial disturbances from the background flow.

Atmospheric waves can propagate in vertical as well as in horizontal direction and are often excited at tropospheric levels (Holton et al., 2003). Energy and momentum is transferred by propagating waves and therefore it can be distributed from their source regions across the atmosphere. On the other hand transported momentum can also interact with the background mean flow when waves dissipate. While dissipation occurs, wave energy and momentum are transmitted to the atmospheric background field and thus considerably affect its structure and variability (Andrews et al., 1987; Holton and Hakim, 2013).

There are many ways to classify and distinguish atmospheric wave types. For example waves can be categorised according to their restoring mechanism (e.g. buoyancy or Coriolis force). A further category could arise from the fact that wave types are 'bounded' within certain regions, such as equatorial waves, which can propagate horizontally and vertically

but are evanescent with increasing latitude from the equator. The most relevant wave types for this work are briefly presented below.

## Planetary Waves

Planetary waves also known as Rossby waves are large scale atmospheric motions with wavelengths of several thousands kilometers and frequencies spanning from days to months (Holton and Hakim, 2013). The underlying basic physical mechanism is the conservation of absolute vorticity. The absolute vorticity is given in equation 1.1 with  $\eta$ ,  $\zeta$  denoting the relative vorticity and  $f$  the Coriolis parameter dependent upon the latitude. Considering an air package with  $\zeta = 0$  on a rotating sphere, which is displaced parallel to the rotational axes of the earth and therefore leading to changes of  $f$ . Consequently this alters  $\eta$  and cause a restoring force proportional to the displacement from the original latitude. This perturbation vorticity field leads to an meridional oscillation with westward phase velocity.

$$\eta = \zeta + f. \quad (1.1)$$

Excitations of planetary waves can occur by the overflow of large orographic obstacles such as the Himalaya or the Rocky mountain ranges. Also the large scale temperature differences of land-sea distributions and the corresponding heat uptake into the atmosphere are considered to trigger planetary waves. Relating to model simulations, excitation of planetary waves could be altered by horizontal resolution, due to the fact that orography is distinctly related to resolution (Roeckner et al., 2006), or alternatively a different representation of sea surface temperature and sea ice coverage (Garny, 2010; Cai et al., 2012), e.g. resulting from different prescribed data sets could also have implications on planetary waves.

In a first approximation propagation of planetary waves is steady and conservative until they break down at 'critical levels', when the values of zonal mean background wind  $\bar{u}$  and zonal phase speed  $c$  are close together (Charney and Drazin, 1961). This is due to the fact that the wave equation obtained from linear wave theory is proportional to  $(\bar{u} - c)^{-1}$  and thus  $\bar{u} = c$  leads to discontinuity. To solve this problem further physical processes are included, namely wave dissipation or non-linearities. As a consequence of these additional processes energy and momentum which were transported by the wave can now be transmitted to the mean background flow as a force and thus, for example can decelerate the zonal mean wind field (Holton and Hakim, 2013; Andrews et al., 1987).

Characteristics and properties of planetary waves can be obtained by Fourier decomposition of large scale perturbations of an atmospheric field. Fig. 1.1 illustrates a modelled winter situation of Northern hemispheric geopotential height at 500 hPa and its corresponding first three harmonics derived from the Fourier decomposition. These first three harmonics are often referred to as planetary waves (Holton and Hakim, 2013). In the literature the first harmonic is frequently named only wavenumber 1 and the second harmonic wavenumber 2 and so on. From Fig. 1.1 the features of the individual zonal wavenumbers are clearly visually perceived. For example in the planetary wavenumber 1 pattern, the

Northern hemisphere can be separated into two regions, one evincing positive values and the other one negative values, respectively.

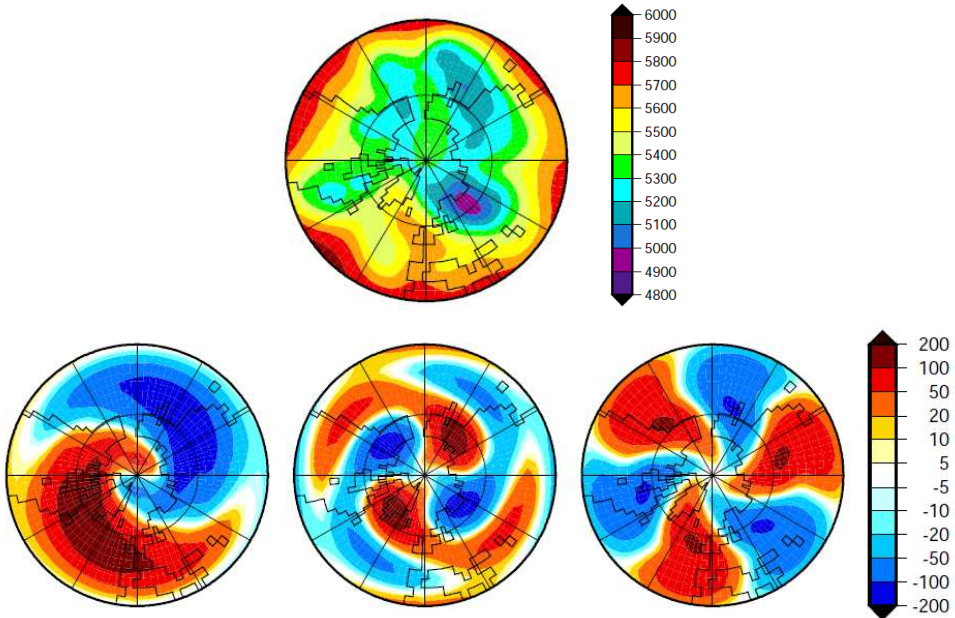


Abbildung 1.1: Upper panel shows the polar stereographic projection of Northern hemispheric geopotential height field at 500 hPa given in gpm. Lower panel gives the individual contributions of wavenumber 1,2,3. After Mager (2004).

## Gravity Waves

Buoyancy force is the restoring force for atmospheric gravity waves. Considering a simplified model where the Coriolis force is neglected and the Brunt-Väisälä frequency, a measure for atmospheric stratification and stability, is held constant, the amplitudes obtained from the wave equation are inversely proportional to the density of the atmosphere and therefore perturbations of the atmospheric fields are growing with altitude. Waves are favourably excited in the troposphere, however in the middle atmosphere non-linear effects increasingly gain importance, resulting in irreversible processes such as turbulence and small scale mixing and dissipation referring to gravity wave breaking. These non-linear effects are believed to have substantial implications on the structure of the middle atmosphere. For example, gravity waves are considered to provide the momentum, that keeps the extratropical mesosphere far from radiative equilibrium (Hitchman et al., 1989). It is also demonstrated that mesospheric gravity wave breaking during winter terms induces a dynamical downwelling in the polar region leading to a warming effect, which spreads down to stratospheric levels (Boville, 1984; Garcia and Boville, 1994). In the tropics gravity waves are also thought to play an important role determining atmospheric structure, which is reflected in the QBO or SAO (description see sections below).

Regarding global models the influence of gravity waves on the larger-scale circulation needs to be parameterised. The relevant waves for the atmospheric circulation have horizontal wavelengths spanning from approximately tens to thousands of kilometers (Fritts and Alexander, 2003). The largest of these waves can be resolved by some global models, however, for an important fraction of these wave types, the required resolution would be too fine in order to be coped by the current global model systems. Furthermore for the tropical region it is known that the vertical model resolution should be at least 1 km in order to resolve the effects of gravity waves (Giorgetta et al., 2002). Additionally, gravity waves can also interact with planetary waves, e.g. Cohen et al. (2013) demonstrated that mean meridional circulation, which is driven by resolved and unresolved waves remains unchanged when altering the planetary wave driving. This is due to the fact that the net effect of changed planetary waves is balanced out through orographic gravity wave driving.

However, observational constraints on the input and the tunable parameters of gravity wave parameterisation are still lacking of necessary detail (Fritts and Alexander, 2003). Among other things, it is discussed that gravity wave parameterisations potentially benefit more from refinement of the gravity waves spectra, especially at levels where the waves are initialised, than from the refinement of dissipation mechanisms itself (McLandress and Scinocca, 2005). So generally speaking there is no universal agreement to implement a dissipation mechanism and thus global atmosphere models have an undesired large degree of freedom in the representation of effects originating from gravity waves.

## Equatorial Waves

In order to understand tropical circulation and thus its variability, equatorial wave dynamics have to be considered. In the tropical region wave types occur, which are equatorially trapped, i.e. their amplitudes decay with increasing distance away from the equator and are evanescent in higher latitudes. The principles of equatorial wave theory such as described in Matsuno (1966) are briefly summarised here.

Formally, the theory bases on the linearised shallow water equations for perturbations of a resting atmospheric state on a so called  $\beta$ -plane. The  $\beta$ -plane assumption simplifies the equations, reducing the Coriolis parameter  $f \approx \beta y$ , where  $\beta$  is a constant and  $y$  is the distance from the equator. This linear relationship is only valid for the tropical region and therefore its solutions are 'trapped' to the equator (Matsuno, 1966; Andrews et al., 1987; Holton and Hakim, 2013). The equations for these equatorially trapped waves are determined by the meridional normal mode number, the frequency, zonal wavenumber and the 'equivalent depth' of the 'shallow' layer of the atmosphere. A further characteristic of its solution is that they can propagate zonally in westward and eastward directions and are either symmetric or antisymmetric about the equator, depending on the meridional normal mode number. Wave modes of odd numbers are antisymmetric whereas those for even numbers are symmetric (Matsuno, 1966). Important classes of these waves are Kelvin and Mixed-Rossby-Gravity waves.

Kelvin waves are symmetric around the equator and propagate eastward and thus can provide eastward momentum. Their dispersion relation is identical to that of the ordinary

gravity wave of shallow water equation given as:

$$v = \sqrt{gh}\lambda, \quad (1.2)$$

where  $v$  denotes the frequency,  $g$  the acceleration due to gravity,  $h$  the equivalent height and  $\lambda$  the zonal wavenumber. Thus frequency is linearly dependent on the zonal wavenumber. The perturbations of Mixed-Rossby-Gravity waves are ordered antisymmetric around the equator. In contrast to the afore mentioned Kelvin waves, they can propagate westward and eastward with a corresponding dispersion relation given as:

$$v = \lambda\sqrt{gh} \left[ \frac{1}{2} \pm \left( 1 + \frac{4\beta}{\lambda^2\sqrt{gh}} \right)^{\frac{1}{2}} \right]. \quad (1.3)$$

The positive square root is associated with an eastward propagating wave and a negative one to a westward propagating wave. Depending on the zonal scale these waves can resemble gravity waves or planetary Rossby waves. Due to this circumstance this wave mode is also named Mixed-Rossby-Gravity wave.

In addition to the equatorially trapped wave modes, extra-tropical waves can also contribute to the variability in the Tropics. Dickinson (1968) demonstrated that vertical propagating planetary waves, originating in the mid-latitudes can be refracted into tropical regions. Furthermore, Hendon et al. (2007) could verify the presence of Rossby Haurwitz waves in tropical lower stratospheric wind fields. Rossby Haurwitz waves are special analytic solutions of the wave equation on the sphere. Equatorial linear wave theory cannot account for spherical geometry and thus Rossby Haurwitz waves cannot be captured. However, Lindzen (1967) presented an approximation of this wave type valid for the equatorial  $\beta$ -plane and therefore equatorial trapped as well as extra-tropical waves can be described consistently by one theoretical approach.

For a more complete and comprehensive overview, as well as the detailed mathematical descriptions of atmospheric wave activity it is referred to textbooks, e.g. Holton and Hakim (2013) or Andrews et al. (1987).

### 1.1.2 Extra-Tropical Variability

The middle atmospheric dynamics of the mid-latitudes and the polar regions are determined by the so called polar vortex. In particular in the winter terms there are large-scale cyclonic circulation systems in the Arctic and Antarctic region – the polar vortices, ranging from mid- to high-latitudes, extending right above the tropopause to middle atmospheric altitudes with a maximum wind speed near the stratopause ( $\sim 50$  km) (Holton et al., 2003).

Their existence is owed to the relation of horizontal zonal wind and the meridional temperature gradient namely the thermal wind balance (Andrews et al., 1987). During the winter season after sun set, polar temperatures strongly decrease due to long wave outgoing infrared emissions to space. In this period the meridional temperature gradient is strongest and consequently westerlies in the polar regions reach their maximum wind

speed forming a polar vortex isolating polar air masses from the mid-latitude stratosphere. These are preferential atmospheric conditions for so called heterogeneous chemical reactions on polar stratospheric clouds, which alter the chemical composition in a way, when sun rises during spring term a severe ozone depletion over the polar region occurs (Dameris et al., 2007). Spring is also the season when the polar vortex breaks up, initiating the atmospheric summer conditions. Solar heating of the polar vortex enhances toward equinox and therefore attenuate the effect of the strong radiative cooling. Additionally the strong planetary wave activity in spring disrupts the vortex. As described above, vertical propagating planetary waves can deposit their momentum under certain circumstances to the mean flow, leading to a deceleration of the stratospheric westerlies. The radiative heating and the deceleration lead to the so called final warming which is marked by a definite stratospheric wind reversal turning westerlies into easterlies notifying summer conditions (Holton et al., 2003).

However, characteristic differences between Southern and Northern winter vortices have to be noted. Regarding the climatological mean, the Southern hemispheric winter polar vortex is stronger (meaning temperatures are lower and wind speeds are larger) and year-to-year variability is smaller compared to the Northern Boreal counterpart (Holton et al., 2003). The more stable Antarctic vortex is a consequence of smaller planetary wave activity during the winter season. Interhemispheric differences of planetary wave activity is partly due to the fact that unlike the Northern hemisphere large-scale orographic obstacles in the Southern hemisphere are only sparsely distributed; i.e. large-scale orography can account for the majority of the Northern hemispheric planetary wave activity (Andrews et al., 1987). Further the Antarctic polar vortex persists longer than the Arctic vortex. Several factors were determined which considerably affect the breakup date of polar vortices. Some studies explored the implications of ozone loss on the vortex dynamics. Ozone loss during equinox season leads to a cooling, which in turn results in a more persistent vortex. In particular, in the Southern hemisphere the breakup date shifts to later dates due to ozone depletion (Akiyoshi et al., 2009). A further stream of research has focused on the relationship of atmospheric waves and the breakup date. For example Hurwitz et al. (2010) demonstrated for their numerical model experiments that the timing of the maximum planetary wave activity is important for the transition of winter to spring conditions of the Antarctic polar vortex. But also interactions by gravity waves can decelerate the polar jets and thus contribute to the breakup of the polar vortices in spring (e.g., Limpasuvan et al., 2007).

### 1.1.3 Tropical Variability

The variability in the middle atmosphere in the tropics are dominated by the Quasi-Biennial Oscillation (QBO) and the Semi-Annual Oscillation (SAO). It has been recognised, that various types of atmospheric waves, particularly gravity waves are the key to force tropical middle atmospheric variability (Dunkerton, 1997, Ray et al., 1998). The principle concepts of the driving mechanisms shall be briefly summarised in the following.

## QBO

The tropical middle and lower stratospheric variability is dominated by the wave induced Quasi-Biennial Oscillation (QBO). The QBO is characterised by alternating westerly and easterly jets originating in the middle stratosphere and propagating downward into the upper troposphere, lower stratosphere (UTLS) region. This oscillation contains periods ranging from 22 to 34 months (Baldwin and Gray, 2005). One of the first theoretical considerations of the underlying processes of the QBO were presented by Lindzen and Holton (1968). Several studies (e.g. Dunkerton, 1997; Ern and Preusse, 2009; Kawatani et al., 2010a) adopted and refined their basic ideas and it is now established that equatorial, vertically propagating Kelvin and Mixed-Rossby-Gravity waves (MRG) provide the required zonal momentum source in order to drive the QBO. It is argued that these vertical propagating atmospheric waves deposit easterly and westerly momentum in the stratosphere, which is due to waves breaking in the vicinity of the 'critical levels', where the background wind speed and the phase speed of the wave are close together (Holton and Hakim, 2013). The Fig. 1.2 gives the schematic representation of the wave driving mechanism described in Plumb (1982). Eastward propagating Kelvin waves (indicated by wavy line with phase speed  $+c$  in Fig. 1.2a) tend to be damped preferentially in westerlies. They are considered to be responsible for the upward transport of eastward momentum associated with a westerly acceleration. Conversely MRG waves (indicated by wavy line with phase speed  $-c$  in Fig. 1.2a) accounting for the upward transport of westward momentum are mainly damped in easterlies, causing an easterly acceleration. The temporal evolution of an idealised flow interacting with equal amounts of easterly and westerly momentum transported by the waves can be seen in Fig. 1.2b. The initial weak westerly is modulated by the vertically propagating waves into a strengthened upper level easterly and lower level westerly flow accompanied by a shear zone descending with time. Eventually the shear zone reaches the 'bottom' which can be considered as the tropopause and the westerlies are damped out and easterlies remain in the stratosphere so that the eastward propagating waves can expand into higher levels initiating a new westerly phase. Following this principle the atmosphere is forced to oscillate between eastward and westward wind regimes.

Apart from this regular inter-annual variability, in the Equatorial lower stratosphere and, also in the extra-tropical and polar regions, a portion of variability appears to be correlated to the tropical QBO. Holton and Tan (1980) demonstrated that on average planetary wave activity in the Northern hemisphere in mid-latitudes and polar region is larger during a QBO easterly phase than during a westerly phase. This differences in planetary wave activity can have implications on the variability of polar regions (Dameris and Ebel, 1990).

## SAO

The Semi-Annual Oscillation (SAO) of the mean zonal wind and temperature in the tropical mesosphere / upper-stratosphere is certainly one of the most prominent features of the middle atmospheric dynamics. However, in contrast to the studies on the QBO in the

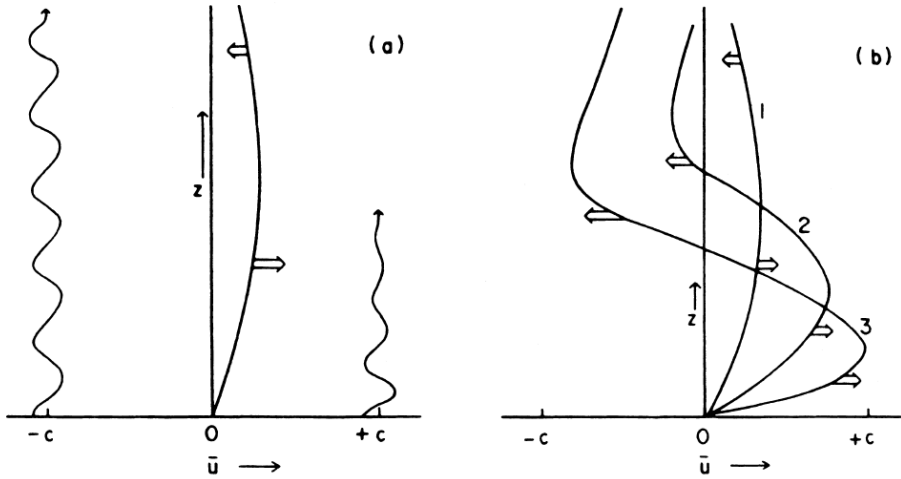


Abbildung 1.2: Sketch of the wave-driving mechanism of the QBO. Details see text. After Plumb (1982).

tropical lower stratosphere, a compelling theory for the detailed mechanism of the SAO is still missing or at least is widely discussed. Observational evidence of the SAO is given in numerous works (e.g. Reed, 1965; Garcia et al., 1997). The Fig. 1.3(b) gives rocket observations of the tropical zonal wind (at Ascension Island 8°S) in the vertical region between 28 and 52 km. The existence of a six-month cycle, which increasingly becomes dominant above 40 km can be detected. Below 40 km, this Semi-Annual Oscillation is masked by the QBO signal. The study of Hirota (1978) was one of the first to demonstrate, that the SAO can be distinguished between an upper stratospheric and mesospheric oscillation, i. e. the phases of the stratospheric and mesospheric SAO are approximately 3 to 4 months out of phase (see Fig. 1.3(a)). Hence, it is supposed, that their underlying driving mechanisms substantially differ. But generally it is an accepted fact, that the SAO is mainly forced by dynamical processes (e.g. Hirota, 1980; Holton and Wehrbein, 1980; Dunkerton, 1982). The stratospheric SAO is considered to be an interplay between vertically propagating Kelvin waves and the mean meridional circulation (Holton and Wehrbein, 1980; Garcia, 2000). The westerly phase is believed to be driven by the dissipation of Kelvin waves, analogue to the QBO. Holton (1975) suggested, that these Kelvin waves are of a shorter period, since long period Kelvin waves are 'filtered' by the QBO. The driving mechanism of the easterly phase of the SAO seems to be significantly different compared to the QBO. It is assumed that easterlies are caused by the mean meridional circulation during the solstice seasons, advecting easterly momentum from the winter to the summer hemisphere crossing the equator (Holton and Wehrbein, 1980). Figuratively speaking, the appearance of equatorial easterly winds in the lower mesosphere at the equator can be described as the penetration of the summer easterlies into the winter hemisphere. A possible interhemispheric coupling is suggested, also depicted by a stronger easterly phase during Northern summer compared to the easterly phase during the Southern summer (Hirota, 1980). But

as discussed in Andrews et al. (1987) advection alone cannot explain the whole easterly phase amplitude of the SAO. Dickinson (1968) demonstrated, that planetary Rossby wave breaking in the equatorial middle atmosphere can provide easterly momentum driving an easterly acceleration. Planetary waves originate from the troposphere in the mid-latitudes but then can be ducted into the tropical middle atmosphere. A further contribution for a easterly momentum source is constituted by inertio-gravity waves with small zonal wave-numbers and high frequencies. Thus, there are three possible mechanism to be assumed, in order to force the easterly phase of upper stratospheric / lower mesospheric SAO.

The driving mechanism of the middle and upper mesospheric SAO (altitudes larger than about 60 km) is less well understood due, among other factors, to a limited number of measurements. The mesospheric SAO is not the focus of this work, however some theoretical concepts and modelling efforts can be read in e.g. Dunkerton (1982); Richter and Garcia (2006); Giorgetta et al. (2006).

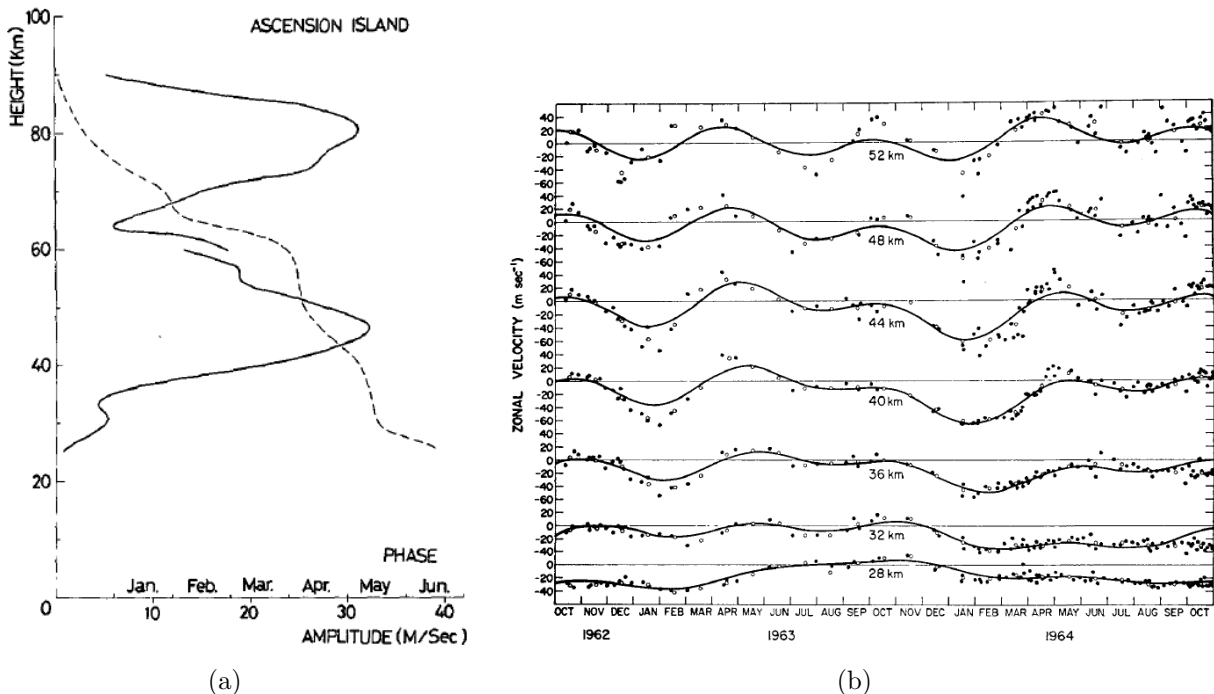


Abbildung 1.3: a) Vertical distribution of the SAO west component at Ascension Island ( $8^{\circ}$ S); amplitudes (solid line), phase (dashed line). From Hirota (1978). b) Zonal wind velocity at Ascension Island ( $8^{\circ}$ S). Solid circles denote individual observations and open circles monthly means. From Reed (1965).

Generally speaking tropical variability can be assigned to internal variability, when considering its driving mechanism. However, QBO and SAO themselves can also affect extra-tropical regions. For example Holton and Tan (1980) propose a mechanism how the QBO modulates the polar stratosphere. This means that the QBO itself can be considered as a forcing contributing to external / deterministic variability. This explicitly demonstrates

the strong relationship between internal and external variability.

## 1.2 Thesis Motivation and Objectives

Variability plays a major role in the determination, description and understanding of dynamical processes of the climate system. It affects distinctly atmospheric structures at the spatial scale from tropospheric to stratospheric and mesospheric levels, encompassing regional (e.g. the polar vortex or the QBO itself) to global extents (e.g. illustrated by the mean meridional circulation). Therefore numerical models need to incorporate relevant processes accounting for variability, however the representation of some aspects of variability remains very challenging. In particular, in global models unresolved waves, such as atmospheric small scale gravity waves have to be parameterised and consequently are subject to considerable uncertainties. Furthermore, these parameterisations are constrained by the relatively small number of observations, which in turn contributes to enlarge the uncertainties (Fritts and Alexander, 2003; Cohen et al., 2013). Nonetheless it is essential that the large variety of stratospheric processes are adequately well represented in numerical model.

The so called power spectra analysis (PSA) allows visualisations of the underlying wave spectrum of a certain atmospheric field and thus to characterise its variability. The methods applied in this work are based on theoretical considerations first presented by Hayashi (1971). Further reading and the mathematical formulations can be found in Hayashi (1979, 1982) or in the Appendix A. For example, in Hayashi (1979) the power spectra analysis can reveal the contributing waves of the Northern hemispheric extra-tropical lower stratospheric geopotential height during autumn season. Several following studies utilising power spectra analysis with emphasis set on the intra-seasonal time scales, in particular the Northern hemispheric extra-tropical latitudes were considered (e.g. Dell'Aquila et al., 2005; Fraedrich and Böttger, 1978). In the work of Wheeler and Kiladis (1999) Hayashi's method is also adapted to the tropical region. They identified characteristic intra-seasonal waves in the tropospheric equatorial temperature field, such as Kelvin and Mixed-Rossby-Gravity waves, which are known to force the QBO (see Sec. 1.1.3). Nevertheless to my knowledge applications of Hayashi's power spectral analysis to intra-decadal time scales have not been described in literature yet.

The purpose of this thesis is to contribute to a better understanding of variability in model systems. Therefore, investigations of atmospheric variability from intra-decadal to intra-seasonal time scales are carried out by means of numerical model simulations. The focus of these studies are on stratospheric levels. Model deficits are documented and possible drivers are identified.

The underlying scientific questions of this work are formulated as follows:

- How to describe atmospheric variability on intra-decadal time scales and what are the relevant processes?
- What are the challenges numerical models are faced with decadal variability and what

are the causes and drivers of model shortcomings reflecting intra-decadal variability?

Chapter 2 gives a brief overview of all utilised data sets of this work. The numerical model systems are introduced and the corresponding simulation setups are summarised. Further data sets used in this work are also described here.

Chapter 3 addresses questions of the intra-decadal variability. A method to analyse intra-decadal variability is introduced and the main characteristics are described and discussed by means of observational based data set. Moreover intra-decadal variability of different model configurations are examined and deviations to observational based data sets are described.

Chapter 4 analyses the detected model differences in more detail, with focus on the tropical and Southern hemispheric polar regions. The origins of possible drivers are considered on intra-seasonal time scales. In the tropics the leading variability patterns of the middle atmosphere, the QBO and the SAO and their driving mechanisms are investigated by means of power spectral analysis. Further attention is given to the difficulties of the representation of the Southern hemispheric polar vortex in numerical simulations and a systematic research into the underlying dynamical processes is carried out. A set of sensitivity simulations concerning the implications of sea surface temperatures, the effects of gravity wave parameterisation and the choice of model resolution on the representation of the Southern hemispheric polar vortex are analysed.

Chapter 5 summarises the results of this thesis and final conclusions are drawn and discussed. Ideas and thoughts for future research are made.



# Kapitel 2

## Model description and Data

### 2.1 MiKlip Decadal Prediction System

The MiKlip (Mittelfristige Klimaprognosen; engl. decadal climate predictions) project was launched by the german government (here: BMBF) in order to create a model system that can satisfy the requirements for a reliable decadal forecast of the climate. The underlying numerical model of the MiKlip decadal climate prediction system is the Max-Planck-Institute Earth-System-Model (MPI-ESM; which is described in Sec. 2.1.1).

A specific simulation procedure was carried out to meet the requirements of the statistical considerations necessary for decadal climate predictions (see Sec. 2.1.2). To date three development stages of MiKlip model system, namely the so called baseline 0, baseline 1 and prototype are completed. Apart from bug fixes the model development stages mainly differ in their applied initialisation method. In the following section a short description of MPI-ESM model is given and the simulation strategies are briefly explained.

#### 2.1.1 MPI-ESM

The Max-Planck-Institute Earth-System-Model (MPI-ESM) is a state-of-the-art atmosphere-land-ocean climate model. In principle three standalone models, representing atmosphere, land-surface processes and ocean are coupled via a special software (Valcke et al., 2003). Interactions between these models take place at the physical interfaces of these models. For example at the surface of the ocean, energy, momentum, water vapour, and traces gases can be exchanged between the atmosphere and the ocean model and thus atmospheric processes can influence oceanic processes and vice versa.

The atmospheric component of MPI-ESM is ECHAM6 (Stevens et al., 2013), the latest successor in the GCM family of ECHAM (European Centre Hamburg general circulation model). ECHAM is based on the weather prediction model of the European Centre for Medium Range Weather Forecast (ECMWF) considering comprehensive parameterisation developed at the Max-Planck-Institute for Meteorology in Hamburg in order to satisfy the requirements of (longterm) climate simulations. ECHAM is a spectral model formulating

the prognostic variables represented by series expansion of spherical harmonics. The horizontal resolution is determined by spectral truncation. For example T63 is the triangular truncation at 63 wavenumbers which correspond to a Gaussian grid of approximately  $1.8^\circ \times 1.8^\circ$  horizontal resolution.

The vertical structure is given in hybrid  $\sigma$ -p coordinates, which follow the terrain at levels near the ground and transition to pressure coordinates with increasing height. Depending on the research interest the uppermost model layer can be chosen variably. For the middle atmospheric version the model lid is usually set at 0.01 hPa ( $\sim 80$  km) or 0.1 hPa ( $\sim 60$  km).

The temporal discretisation is based on a semi-implicit leap frog scheme. To meet the requirements for stable numerical solutions the time-step has to be chosen dependent from the utilised horizontal resolution (e.g. for T63 a time step of 6 minutes is necessary).

The land-surface processes are represented by the JSBACH (Jena Scheme for Biosphere-Atmosphere Coupling in Hamburg) scheme. In the context of MPI-ESM this scheme can be considered as a lower boundary condition of the atmospheric model representing land surfaces. Biogeochemical and biogeophysical processes arising from vegetation (such as the soil hydrology; the soil heat transport or carbon uptake and release) can be provided to the atmosphere. Details of particular aspects of the model are described in Raddatz et al. (2007), Vamborg et al. (2011) and Reick et al. (2013).

The ocean and sea-ice component of the MPI-ESM is formed by the Max-Planck-Institute ocean model (MPIOM; Marsland et al., 2003; Jungclaus et al., 2013). MPIOM based on the primitive equations with hydrostatic and boussinesq assumptions. Processes implemented in this model represent the physical as well as the biochemical characteristics of a deep ocean system. Biochemical processes such as, e.g. the solubility of carbon dioxide, are captured by HAMOCC (Hamburg Ocean Carbon Cycle; Maier-Reimer et al., 2005) a sub-model of MPIOM.

### 2.1.2 MiKlip Simulation Setup

In MiKlip the MPI-ESM is used to conduct various sets of experimental designs following the recommendations of the CMIP5 (Coupled Model Intercomparison Project Phase 5) framework (Taylor et al., 2012). In this work only the so called decadal hindcast experiments of development stage baseline 1 are analysed. The aim is to produce a realistic representation of the climate state for the time period of one decade. Baseline 1 is selected due to the fact that this development stage enables the latest model version providing two model configurations with different vertical resolutions (in contrast prototype provides only one model configuration and baseline 0 suffered from some model errors which could be eliminated in baseline 1). A brief description of the baseline 1 model setups and the experimental design is given here.

The experiments are performed in a low-resolution (LR) and a medium-resolution (MR). ECHAM6 the atmospheric component is applied in T63 horizontal resolution including the middle atmosphere up to 0.1 hPa for both model configurations LR and MR. A substantial difference between the models is their vertical resolutions. For LR, 47 vertical levels were

used and for MR 95 levels, respectively. The ocean model is run in a horizontal resolution of about  $1.5^\circ$  for LR and  $0.4^\circ$  for MR both with 40 levels in the vertical direction.

The simulations consist of an ensemble size of at least five members initialised on the first day in every year from 1961 to 2012 and have the length of 10 years. Each ensemble member is realised with a lagged initialisation, by means of using consecutive days after January 1st with an assimilation experiment setting the initial conditions. Illustration of this concept is given in the Fig. 2.1. In the assimilation experiment, the atmospheric fields (i.e. temperature, vorticity and divergence) are truncated against ERA40 (Uppala et al., 2005) for the period 1960-1989 and ERA-Interim (Dee et al., 2011) for the period 1990-2012. For the ocean model, data is taken from the ORAS4 ocean reanalysis (Balmaseda et al., 2013). Technical details of the assimilation experiments can be read in Pohlmann et al. (2013).

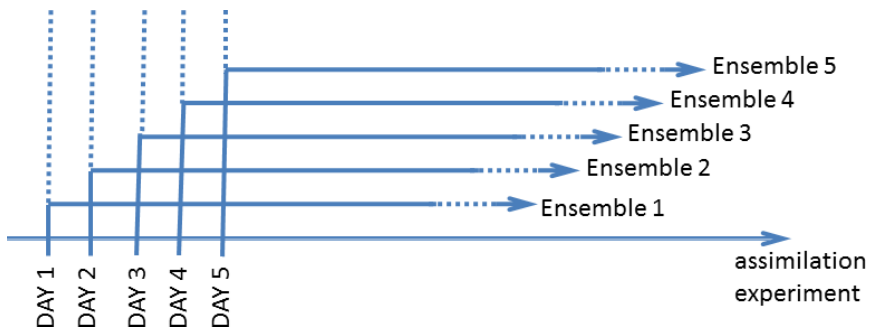


Abbildung 2.1: Sketch of ensemble initialisation in MiKlip. Each ensemble is initialised by assimilation experiment.

## 2.2 The EMAC Model System

In order to analyse relevant processes of decadal climate predictions, additional simulations were carried out with the more flexible model system ECHAM MESSy Atmospheric Chemistry (EMAC). The GCMs incorporated in MiKlip and EMAC originate from the same model family ECHAM. Therefore general findings gained within the EMAC simulations can contribute to a better understanding of relevant processes in the decadal prediction system MiKlip.

EMAC is a numerical Chemistry Climate Model (CCM) system describing physical and chemical processes from the troposphere to the middle atmosphere and their interaction with oceans, land and anthropogenic influence (Jöckel et al., 2010). The EMAC system is based on MESSy a sub-model coupling interface (described below in Sec. 2.2.2) which is connected to the general circulation model (GCM) ECHAM5 (see Sec. 2.2.1). The EMAC model has a flexible modular structure, which is also superbly suited for extension of miscellaneous processes, allowing studies of a wide range of physical, chemical and biological feedbacks and how their response impact the whole climate system. EMAC is emerging

as a comprehensive Earth System Model (ESM) including relevant domains such as the atmosphere, hydrosphere and parts of the biosphere and it is further developing.

### 2.2.1 ECHAM5

The dynamical core of EMAC is constituted by the fifth generation of ECHAM (ECHAM5) (Roeckner et al., 2003). Comparable to MiKlip, ECHAM5 is based on the weather prediction model of the ECMWF. Therefore the implemented processes of EMAC concerning the atmospheric dynamics are very similar to MiKlip. General differences between both model systems are discussed below in Sec. 2.2.4.

### 2.2.2 MESSy

The Modular Earth Sub-model System (MESSy) is considered as a bottom up approach towards Earth System modelling. MESSy comprises a generalised interface structure for the standardised control of sub-models and their interconnections. In this case a sub-model is seen as the implementation of a process according to a coding standard. In principle MESSy is organised in four different model layers:

- BML (Base-Model-Layer) hosts the dynamical core of the base-model. In case of EMAC this is ECHAM5. Other processes, especially parameterisation are separated from the base-model into sub-models. The goal of which is to maintain a BML consisting of time integration management and associated control processes only.
- BMIL (Base-Model-Interface-Layer) provides both the information and data exchange between the different sub-models as well as between the individual sub-models with the base-model.
- SMIL (Sub-Model-Interface-Layer) refers to the individual sub-models. Here relevant information is collected from the BMIL and are passed to the Sub-Model-Core-Layer (see next point) and the other way round data calculated in the sub-models are provided to transfer back into the BMIL.
- SMCL (Sub-model-Core-Layer) is the standalone core of the sub-model, which could operate independently from the base-model.

A schematic representation of MESSy is given in Fig. 2.2. All sub-models used in this work are listed in Table 2.1. An overview of the current status of MESSy version 2, which is the version used in this work, can be found in Jöckel et al. (2010).

### 2.2.3 Simulation Setups with EMAC

The modular property of EMAC is a big advantage when performing sensitivity studies. The modules representing certain atmospheric processes can be easily switched on or off

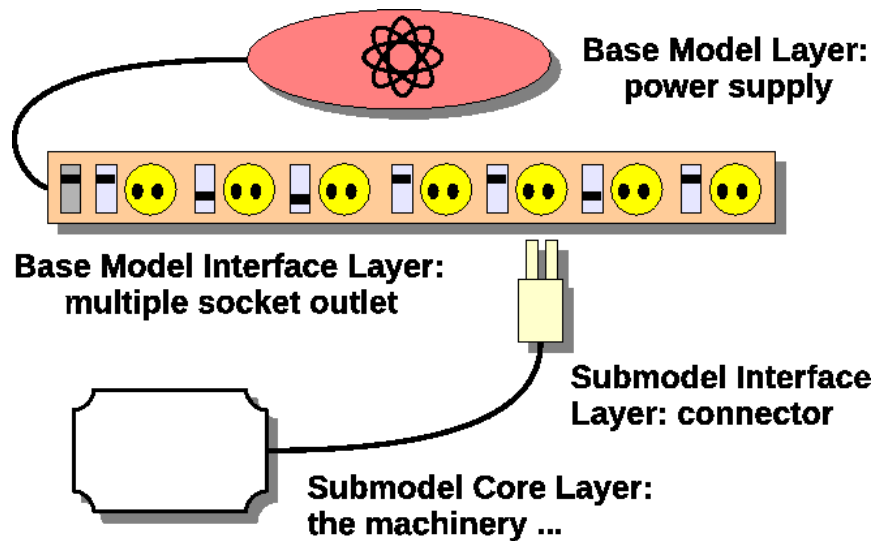


Abbildung 2.2: Sketch of MESSy interface structure from Kerkweg and Jöckel (2012).

Sub-model	Description	Reference
RAD	Revised radiation interface structure of original ECHAM5 code including new and extended features	Roeckner et al. (2003)
AERO_OPT, CLOUDOPT	Calculation of aerosol and cloud optical properties are separated from the original ECHAM5 scheme and transfer to these sub-models	Roeckner et al. (2003)
CONVECT	Tiedtke convection scheme	Tiedtke (1989)
CLOUD	Sundqvist cloud scheme	Sundqvist (1978); Sundqvist et al. (1989)
GWAVE	non-orographic gravity wave scheme	Hines (1997a)

Tabelle 2.1: List of all relevant sub-models used in this work.

or can alternatively be modified. In this work a set of so called time-slice simulations were conducted, to analyse the effects on the model dynamics concerning the chosen sea surface temperature data set, the horizontal and vertical resolution and different setting of the non-orographic gravity wave parameterisation.

Time-slice simulations describe a specific climate equilibrium state. Technically the boundary conditions are kept constant, only allowing a seasonal variability. The simulations performed here are all conducted with a prescribed annual cycle of the greenhouse gas concentrations (i.e.  $CO_2$ ) of the year 2000 derived from recommendations of the IPCC (2007) and a zonally symmetric ozone climatology based on the work of Paul et al. (1998). Likewise the model top at 80 km remains the same in each simulation and therefore the middle atmospheric dynamics are included. A description of the setups is outlined below.

### Reference Simulation

The reference simulation (REF) is the realisation of a 20 year time-slice experiment considered as the climate equilibrium state around the year 2000. The horizontal resolution is T42 corresponding to a approximately  $2.8^\circ \times 2.8^\circ$  Gaussian grid. The vertical extent from surface to the middle atmosphere with a upper model lid centred at 0.01 hPa is captured by 90 vertical levels. For the lower boundary conditions the annual cycle of the 10 year (from 1995 to 2004) climatological mean of the Atmospheric Model Intercomparison Project (AMIP) SSTs are prescribed (Hurrell et al., 2008). Sub-models used are AERO\_OPT, CLOUD, CLOUDOPT, CONVECT, RAD and GWAVE (see Table 2.1).

### Sea Surface Temperature (SST) Sensitivities

It is generally accepted that atmospheric waves play an important role for internal variability. SSTs and sea-ice conditions have significant implications on atmospheric wave activity and thus on model dynamics and variability too (see Andrews and McIntyre, 1976; Garny, 2010; Cai et al., 2012; Holton and Hakim, 2013). The SST experiments are carried out in order to get an estimate of the sensitivity of the model's behaviour relative to different SST data sets.

Technically the prescribed AMIP SSTs from REF were replaced by the climatology of a different SST product. AMIP is an observational based SST and sea-ice data set provided by the National Centre of Atmospheric Research (NCAR) following a specific process described by Hurrell et al. (2008). One sensitivity simulation named HAD is conducted with the seasonal cycle of HadISST (Hadley Centre Global Sea Ice and Sea Surface Temperature) averaged over the same period (from 1995 to 2004) as in REF. HadISST was developed by the Met Office Hadley Centre for Climate Prediction and Research. It is a global data set derived from observations. For technical details and further reading see Rayner et al. (2003). The last experiment in this series is named MPIOM, which is conducted with a SST climatology, that originates from a ten year climatological mean (from 1991 to 2000) derived from the MR model configuration of the MiKlip decadal prediction system. MiKlip is based on an interactive coupled atmosphere ocean general circulation model (details see

Sec. 2.1). Thus this set of sensitivity experiments represents two simulations driven by SSTs based on observations and one simulation operating with modelled SSTs.

### Gravity Wave Sensitivities

Gravity waves play a substantial role in the stratospheric dynamic, e.g. on the one hand in the tropics it is known that gravity waves provide the necessary momentum in order to drive the QBO (Dunkerton, 1997; Ern and Preusse, 2009) and on the other hand simulated upper stratospheric polar winter vortices are too cold without taking gravity wave interactions into account (Garcia and Boville, 1994). However spatial scales of gravity waves cannot be captured by the resolution of the majority of todays GCMs and thus have to be parameterised. These parameterisations are constrained by a lack of observations and therefore the models are challenged by an undesirably large degree of freedom (Fritts and Alexander, 2003).

In EMAC non-orographic gravity waves are represented by the sub-model GWAVE. The theoretical concepts of GWAVE are based on the ideas of Hines (1997a,b) and are briefly outlined here. The launch spectrum is assumed to be azimuthally isotropic in frequency. The launch spectra is the initial condition of the gravity wave field, providing waves which propagate vertically and make momentum available. Momentum flux density now can be employed to describe the development of the wave field with height, due to the fact that momentum flux density is conserved for steady propagation and thus only can be changed by dissipation. In the parameterisation of Hines (1997a,b) the so called vertical cut-off wavenumber  $m_j$  is considered as a threshold for the portion of the initially incident gravity wave flux that continues its upward progress and therefore  $m_j$  is the characteristic value that describes the dissipation of gravity waves in the model. The vertical cut-off wavenumber  $m_j$  for a given azimuth  $j$  and height is given as

$$m_j = N_i / (\phi_1 \sigma_j + \phi_2 \sigma + V_j - V_{ji}), \quad (2.1)$$

where  $N_i$  is the Brunt-Väisälä frequency at the initial height,  $\phi_1$  and  $\phi_2$  are constants,  $V_j$  is the background wind in the  $j$  azimuth direction, and  $V_{ji}$  is the background wind in the  $j$  azimuth direction at the initial height. The  $\sigma$  denotes the absolute root mean square horizontal wind speed induced by gravity waves and  $\sigma_j$  is the root mean square horizontal wind speed for the  $j$  azimuth. The values  $\sigma$  and  $\sigma_j$  are derived from the root mean square wind induced by gravity waves at the initial height given by the *rmscon* parameter. So dissipation is dependent on the source spectra, the background wind field and the choice of the *rmscon* parameter.

The launch spectra, or in general gravity wave parameterisation are constrained by a lack of observations (Fritts and Alexander, 2003). Therefore parameterisation parameters have to be tuned to preserve a meaningful climate state. In GWAVE the *rmscon* is such a tuning parameter, and can be used to control the vertically propagating gravity wave spectra as described above. Very simply speaking, increasing the *rmscon* parameter would lead to an enhanced dissipation of gravity waves and decreasing the *rmscon* parameter

---

Name	SST	Resolution	GWAVE	<i>rmscon</i>
REF	AMIP	T42L90	yes	0.96
HHR	AMIP	T63L90	yes	0.96
LVR	AMIP	T42L47	yes	0.96
HAD	HADISST	T42L90	yes	0.96
MPIOM	MPIOM	T42L90	yes	0.96
G1	AMIP	T42L90	yes	0.88
G2	AMIP	T42L90	yes	0.92
G3	AMIP	T42L90	yes	1.00
G4	AMIP	T42L90	yes	1.04
G5	AMIP	T42L90	no	-

*Tabelle 2.2: List of all simulations and corresponding resolutions and *rmscon* parameters.*

would result in a reduced gravity wave dissipation. Details can be found in the afore mentioned references and e.g. McFarlane and Manzini (1997).

In order to estimate the implications of non-orographic gravity waves on the model dynamics, five sensitivity simulations are carried out. The model setup used here is identical to REF, but for this set of sensitivities the available simulation time for the analysis is now six years, so as to maintain a feasible amount of data. Moreover, for each simulation the *rmscon* parameter is gradually changed and additionally for one sensitivity simulation the effects of non-orographic gravity waves are switched off (see Table 2.2).

## Resolution Sensitivities

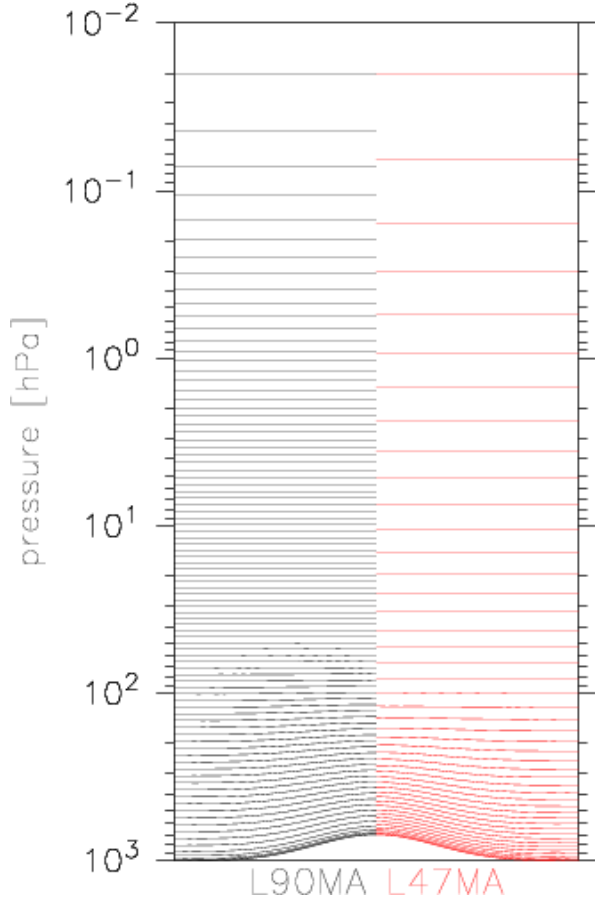


Abbildung 2.3: Distribution of vertical levels in L90 and L47 version.

much coarser (at  $\sim 2\text{-}3$  km) than in L90 ( $< 1$  km).

### 2.2.4 Differences between MPI-ESM and EMAC

One major difference between EMAC and MPI-ESM (the underlying numerical model of MiKlip) is the treatment of the ocean. MPI-ESM utilises an interactive deep layer ocean whereas in EMAC the SSTs are prescribed. Therefore variability arising from interactions between ocean and atmosphere, e.g. interactions with ENSO, are not represented adequately in EMAC. Furthermore the radiation schemes of both models differ, which could have implications on the model dynamics, too. However, the dynamical core of MPI-ESM and EMAC are based on the same model family, namely ECHAM5 is applied in EMAC and ECHAM6 in MPI-ESM respectively. The implementation of the fundamental dynamics

Horizontal and vertical resolutions have implications for the model dynamics. For example, it is demonstrated that higher horizontal resolution in ECHAM5 leads to a better compliance between model data and observational-based reanalysis data, in particular during Boreal winter (Roeckner et al., 2006).

In order to quantify the impact of spatial resolution on the model dynamics of EMAC, two different sensitivity studies were performed. Apart from resolution these experiments have the same experimental setup compared to REF. The model lid at 0.01 hPa is kept consistent as well as the other parameters used in the sub-models. The first sensitivity is realised with a **higher horizontal resolution (HHR)** using T63L90 (T63 corresponds to a gaussian grid of approximately  $1.8^\circ \times 1.8^\circ$ ) with a time step of 6 minutes instead of T42L90 and 12 minutes, respectively. A second sensitivity study with **lower vertical resolution (LVR)** with T42L47 is conducted, at vertical levels lower than in the REF simulation. The distribution of the different levels in the vertical is displayed in Fig. 2.3. Qualitatively the tropospheric resolution of L90 and L47 are identical but for middle atmospheric levels the vertical resolution in L47 is

remain the same. The treatment of the primitive equations as well as important parameterisations, such as non-orographic gravity wave parameterisation and convection are identical. Minor changes between ECHAM5 and ECHAM6 were carried out for example in the 'tuning' of these parameterisations (details see Mauritsen et al., 2012) or treatment of gravity waves in the tropics are altered (Stevens et al., 2013). However, from a qualitative perspective the dynamics in both model systems remain similar. This is also demonstrated by the study of Deckert (2012), who showed that Southern winter hemisphere in EMAC as well as in ECHAM6 suffer from a too weak polar vortex. Therefore findings obtained within the EMAC simulations can qualitatively contribute to a better understanding of the dynamics in the MiKlip system.

## 2.3 Reanalysis ERA-Interim

Reanalysis data sets are usually derived from weather forecast models paired with an assimilation system integrating a large number of achieved observations, for example from satellites. The key strengths are for example, the supply of one physically and dynamically consistent data set and the combination of comprehensive observations and models that provide a good estimate for the description of the historic climate system, on a global scale.

ERA-Interim is the third generation reanalysis product of the European Centre for Medium-Range Weather Forecast (ECMWF). The underlying model system utilised for the production of ERA-Interim is based on the so-called Integrated Forecast System (IFS) developed by the ECMWF. This IFS version applied a 12 hourly analysis window and a spatial horizontal resolution of T255 (roughly 80 km) and 60 vertical levels from ground to model lid at 0.1 hPa, which corresponds roughly to 60 km height. Temporal coverage is from 1. January 1979 to today. See Dee et al. (2011) for a comprehensive overview of the ERA-Interim system.

When using ERA-Interim, general uncertainties of the data set have to be kept in mind, e.g. temporal inconsistencies can arise due to switching or mixing of observational platforms. In upper stratospheric level the major source of discrepancy arises when observations from new satellite instruments are introduced (Rienecker et al., 2011). This can lead to spurious long-term trends and variability of the reanalysis output (Dee et al., 2011; Rienecker et al., 2011).

Furthermore, the quality of ERA-Interim increases with the number of available observations. For the middle atmosphere, in particular from upper stratospheric to lower mesospheric levels in-situ observations are increasingly sparse and thus major uncertainties in this altitudes remain (Mitchell et al., 2014). Moreover, the underlying numerical model of ERA-Interim has a model lid at 0.1 hPa and gravity waves are damped in the uppermost level in order to maintain momentum conservation (Orr et al., 2010). This damping is necessary to avoid spurious sensitivities and feedback mechanisms in lower altitudes as described in e.g. Shaw and Shepherd (2007), but the effects of this damping are an artificial non-physical response in the upper most model layers of the reanalysis data set.

In this work ERA-Interim is considered as a reference data-set, which is used to compare and evaluate model results. The occurring caveat of long-term trends mentioned above plays only a minor role in the analysis here, since the focal points are on the mean climatological state (as described in Sec. 2.2.3) or on intra-decadal processes and therefore the issue of long-term trends are only of partial concern. Regarding the artificial wave damping at the uppermost level of ERA-Interim (Orr et al., 2010) comparisons to model simulations in levels near the model top, approximately above 0.5 hPa, should not be taken into consideration.

The choice of ERA-Interim is based on following considerations. First ERA-Interim provides data including upper stratospheric and lower mesospheric altitudes, which is not necessarily standard for all reanalysis. Moreover, ERA-Interim belongs to the so called 3rd generation reanalysis, which applies more sophisticated data assimilation approaches that enhance analysis accuracy (Courtier et al., 1994). Further significant improvements are offered, when ERA-Interim is compared to the forerunner models, such as ERA40 (Uppala et al., 2005). For example the quality of stratospheric circulation in ERA-Interim is enhanced compared to older reanalysis generations (Dee et al., 2011). Moreover, ERA-Interim is well established and comprehensive experiences and known problems are widely documented (e.g. Dee et al., 2011; Dee and Uppala, 2008). Apart from ERA-Interim other data sets considering middle atmospheric level and additionally being associated with 3rd generation reanalysis are JRA-55 (Japanese 55 years Reanalysis; Kobayashi et al., 2015) and MERRA (Modern Era Retrospective-Analysis for Research and Applications; Rienecker et al., 2011). For JRA-55 it was only very recently that the first documentation has been published (Kobayashi et al., 2015), so the long term experiences such as in ERA-Interim are missing. Regarding MERRA the characteristic signals of 'deterministic' variability (such as solar, QBO, ENSO, and volcanoes) are remarkably consistent compared to ERA-Interim (Mitchell et al., 2014). Moreover, on inter-annual and seasonal time scales the global mean atmospheric fields (e.g. temperature and zonal wind) of MERRA and ERA-Interim are in a good agreement (Rienecker et al., 2011). However differences in the representation of the climate signal can be relatively large depending on both the variable itself and the region of interest. For example the correlation of tropical tropospheric winds is comparatively low between MERRA and ERA-Interim (Rienecker et al., 2011). But still uncertainties and their causes in particularly the middle atmospheric region of reanalysis data sets are issues of current research. Intercomparison projects dedicated to these questions have been started relatively recently (Fujiwara and Jackson, 2013).

So to date ERA-Interim represents a good estimate for the recent climate state and therefore can be used with appropriate care in order to evaluate simulation results.



# Kapitel 3

## Intra-Decadal Variability

In the context of intra-decadal predictions, information of variability across various time scales, spanning from days to decades, are essential to conduct reliable simulations. The drivers and their spatial and temporal contribution have to be characterised. For example external / deterministic variability such as QBO (Quasi Biennial Oscillation) or ENSO (El Nino – Southern Oscillation ), but also internal variability are important and models have to consider the underlying processes in order to give a reasonable representation of the climate state on time scales of a decade.

### Power Spectral Analysis

Power spectral analysis (PSA) enables one to draw a detailed picture of the relationship between spatial and temporal scales. Periodic processes in terms of waves can be described dependent of their wavelengths and frequencies. In this work the PSA is calculated after the method described in Hayashi (1979) and Hayashi (1982). Details of this concept can be found in the Appendix A.

In this section the total variance (often also named power) of monthly averaged zonal wind field is presented as the sum over all wavelengths, this the information of the derived power spectra is only dependent upon frequency. For the representation of tropospheric altitudes the 850 hPa pressure level was chosen and for the stratosphere the 30 hPa pressure level was selected, respectively. The covered time period for all analysed simulations is 10 years. In the case of the transient MiKlip experiments the timespan is derived from 1991 to 2000 and alternatively for the EMAC, time-slice simulations from a ten year time series are taken from a climate mean state representing the climate conditions around the year 2000. To preserve comparability all data sets are regridded to the lowest resolution T42 before the PSA is performed. The unit for intra-decadal power of zonal wind is given in  $(m/s)^2$ . But for illustration purposes the natural logarithm of the power is applied and additionally the power is scaled by the frequency, so the displayed power has a unit given in  $lg(m/s)^2 * cpm$  ( $cpm$ ; cycle per months). Following Zangvil (1977) this procedure is required to preserve area fidelity, which in turn is necessary in order to illustrate the power distribution correctly.

### 3.1 PSA of ERA-Interim

The PSA of ERA-Interim is used as a reference from which to compare model results. Figure 3.1(a) gives the distribution of power dependent on the period for each latitude at 850 hPa representing a tropospheric level. The pattern is characterised by the annual cycle and semi-annual cycle which is reflected by the prominent features at 12 and 6 month, respectively. Most of the power can be found in the mid-latitudes and periods up to one year, which is reasonable since extra-tropical tropospheric westerlies are known to transport large-scale weather patterns contributing substantially to variability. With increasing periods the power decreases.

However, observing the tropical region from  $15^{\circ}\text{N}$  to  $15^{\circ}\text{S}$  relatively high power can be detected for periods larger than 12 months. This equatorial variability pattern could arise from effects provided by the ENSO. The periods of ENSO phases cover a broad spectrum predominantly between 1-10 years (Rayner et al., 2003) and therefore their contribution to variability is mainly on time scales longer than 12 months.

Similar to the troposphere, the annual and semi-annual cycle clearly arises from the PSA in the stratosphere at 30 hPa (Fig. 3.1(b)). But as mentioned in the introduction the inter-annual and intra-seasonal variability of the stratosphere is much larger than in the troposphere. This is also reflected in the larger amplitudes of intra-decadal PSA at the stratospheric level. A large part of the stratospheric power is distributed in the extratropical and polar region with periods up to one year. This illustrates the major role of polar vortices and their interactions with extra-tropical areas that contribute to high variability in the stratosphere. In general, comparing both hemispheres in the regions  $60^{\circ}$  North / South towards the poles, the Northern hemispheric stratosphere bears larger areas of maximum variability.

This is reasonable since it is known that the Northern polar vortex is more variable when compared to its Southern hemispheric counterpart (Holton et al., 2003).

Apart from at higher latitudes, the tropical region also shows a striking variability pattern around the period of 24 months. Here variability can reach values of a comparable magnitude to the extra-tropical regions on periods shorter than a year. It is tempting to think this stratospheric feature could be associated with the QBO which is characterised by an alternating eastward and westward wind regime every 2 years. But to prove this hypothesis further research and analysis is necessary to draw a conclusion.

#### PSA Features via Regression Analysis

In order to give more evidence to the power spectra found in the tropical region a multi-linear-regression (MLR) model is used to calculate the influence of QBO and ENSO on the PSA. In a first step the raw zonal wind field is expressed by its base functions, which represent relevant processes, i.e. the annual cycle, the linear trend, QBO, ENSO and the 11 year solar cycle (more details and theoretical background of the concept of the MLR can be read upon the Appendix B). To derive a wind field without the effects of one these processes, the regression coefficients accounting for this effect are set to zero. The remaining

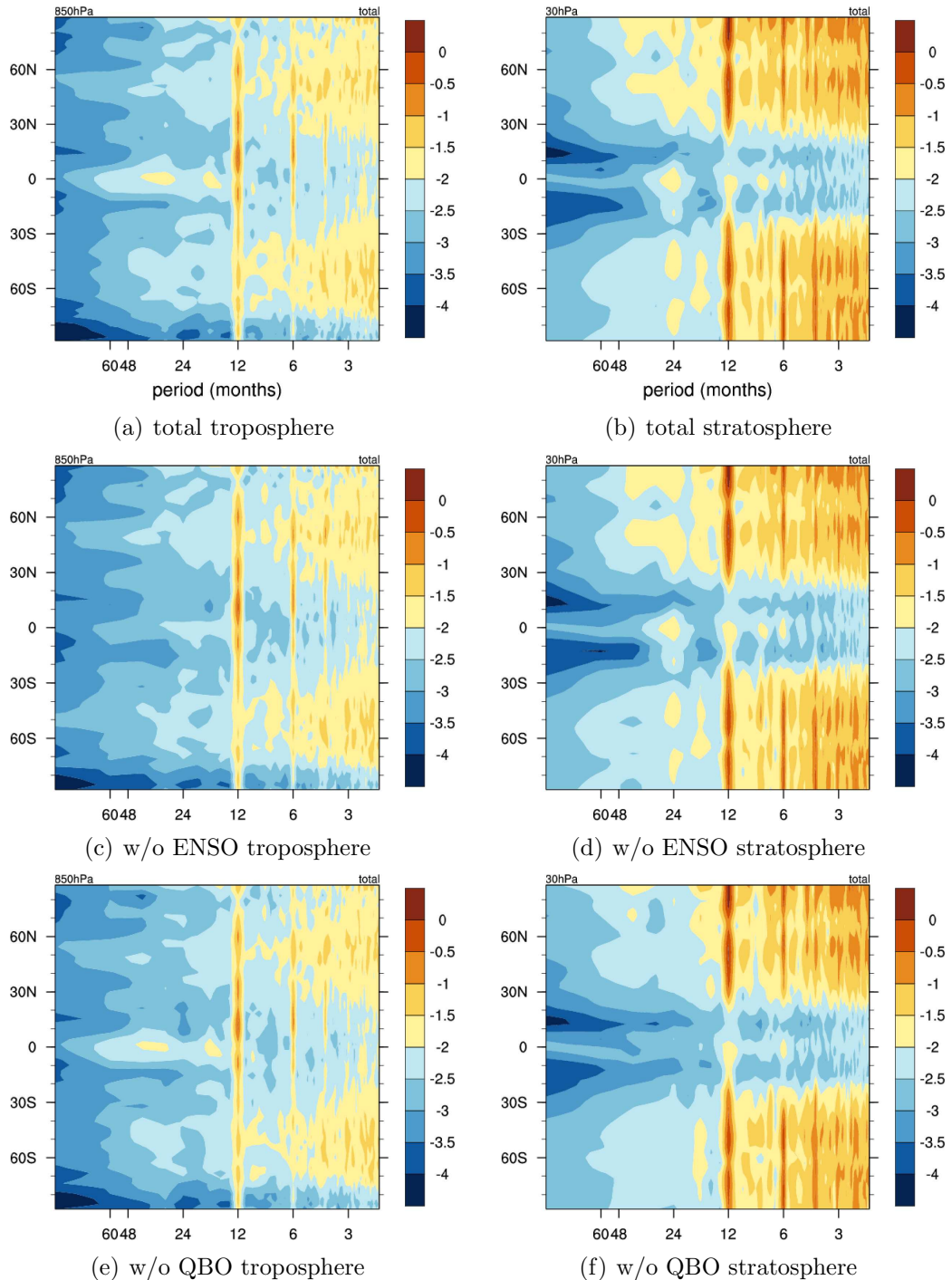


Abbildung 3.1: ERA-Interim power spectra of zonal wind summed over all wavelengths. The left column represents the tropospheric level at 850 hPa and the right column refers to stratospheric level at 30 hPa. a), b) give the PSA of the original field; c), d) without ENSO signal and e), f) without QBO signature, respectively. Units are  $lg(m/s)^2 * cpm$ . See text for details.

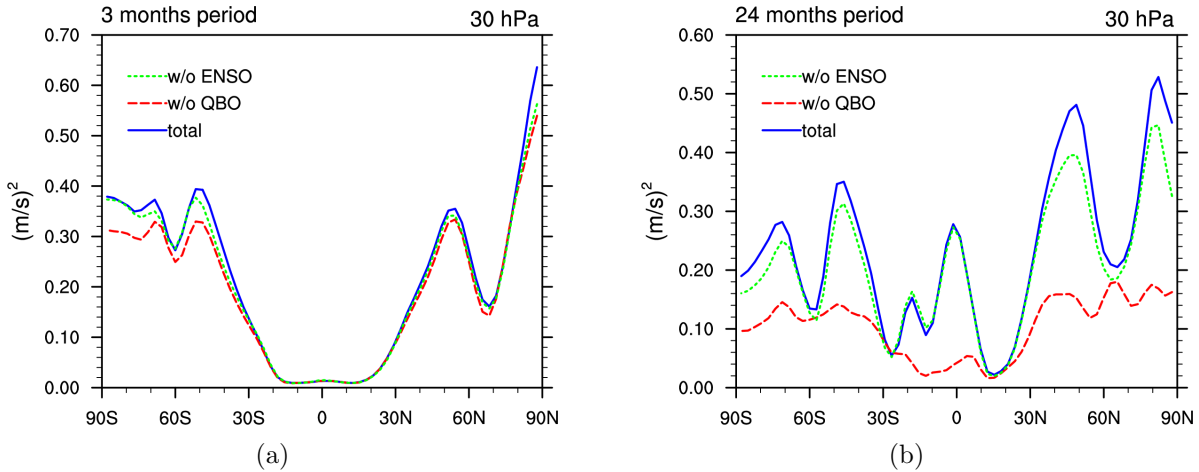


Abbildung 3.2: ERA-Interim power spectra summed over all wavelengths for stratospheric level at 30 hPa for zonal wind field, wind field without ENSO or QBO effect, respectively. a) The 3 months period, b) the 24 month period.

coefficients then leave a wind field independent from this process. Afterwards the PSA for this 'regressed' wind field is calculated. In Figure 3.1 the PSA for wind fields without QBO (Fig. 3.1(e),(f)) or ENSO (Fig. 3.1(c),(d)) are presented. The effects of the solar cycle are not considered here, since the regarded time series accounting for the PSA is 120 months and therefore the time series is too short relevant to a period of the solar cycle.

Figures 3.1a) to f) show the PSA calculated for the original zonal wind field, and corresponding wind fields without QBO or ENSO effects respectively. With regard to intra-annual time scales, meaning periods up to 12 months the variability pattern seems to be independent from the applied MLR analysis. At the tropospheric as well as at the stratospheric level the power distribution within the intra-annual periods of the original and 'regressed' wind fields are very similar to each other. This becomes more clear in Figure 3.2(a), which illustrates the power of the zonal wind at 30 hPa for the 3 month period. The latitudinal distributions of seasonal variability have a similar shape for all three analysed wind fields, reflecting the comparable power distribution of the individual wind fields on intra-annual time scales.

Looking at periods larger than 12 months, distinct differences between the PSA patterns derived from the 'regressed' wind fields and the 'raw' wind field can appear, i.e. in tropospheric level, variability of the wind field without ENSO (see Fig. 3.1(c)) is considerably lower (partly by one order of magnitude) in tropical region for periods larger than 12 months compared to the other analysed wind fields. The 'raw' wind field (Fig. 3.1(a)) and the wind field without QBO (Fig. 3.1(e)) evince a similar pattern and therefore the QBO tends not to have any effects on the variability pattern here. In conclusion the tropical tropospheric power spectrum detected for periods larger than 12 months can be attributed to the effects of ENSO.

Regarding the stratosphere a prevailing fraction of variability is contributed by the

QBO. This in particular, can be seen when comparing the PSA pattern of the wind field without QBO (Fig. 3.1(f)) to the pattern of the 'raw' wind field (Fig. 3.1(b)). The pattern of the power distribution in the vicinity of the 24 months period, which correspond to periods of the QBO, almost vanishes in the tropics and also in higher latitudes as well. Figure 3.2(b) illustrates the latitudinal distribution of stratospheric power for the 24 month period. As expected the effects of the QBO have a large influence on the total variability of the 2 year period. In the tropics the QBO contributes to 80% of total power, whereas in higher latitudes the relative differences are about 70%. The fact that the QBO variability pattern is not only constrained by the tropics but also affects the extra-tropics can be explained by Holton and Tan (1980), who found an interaction of the QBO and the extra-tropical stratospheric circulation.

The features in the tropical variability pattern which were assumed to be triggered by external / deterministic variability such as ENSO or QBO, can now be confirmed by the means of the MLR analysis. In order to get an impression of the contributions of 'internal' variability, power spectra of the residual compound of the MLR analysis is calculated (Fig. 3.3). The resulting power spectra thus illustrates the intra-decadal variability without the effects of the processes represented by the base functions of the MLR (i.e. the annual cycle, the linear trend, QBO, ENSO and the eleven year solar cycle). A striking difference compared to the raw power spectrum is the absence of large variability values at periods of 12 and 6 months. In general the values of the power spectrum, derived by the residual compound are smaller compared to the unregressed power spectrum, however the main characteristics of the intra-decadal variability pattern are qualitatively preserved. In particular, intra-annual variability (with periods shorter than 12 months) at mid-latitudes at tropospheric levels and in the polar regions at stratospheric levels respectively, remain virtually unaltered if the 'residual' (Fig. 3.3) and 'raw' power spectra (Fig. 3.1(a),(b)) are compared. Therefore internal variability is dominating the power spectra within periods of intra-annual time scales. This finding is quite reasonable, since the internal variability can be characterised by the interaction between atmospheric waves and the background mean flow. Geographical locations determined for internal variability are prominent for large-scale atmospheric phenomena such as the subtropical jets or the polar vortices which are in turn known to be sensitive to these interactions (Andrews et al., 1987; Holton et al., 2003).

## 3.2 Power of MiKlip Simulations

The power spectra presented here are derived from the MiKlip baseline 1 data set. The MiKlip MR with 90 vertical levels as well as the LR configuration with 47 vertical levels are analysed. The time period covers the years from 1991 to 2000. The PSA is performed with a preceded regridding to T42 and the removal of the linear trend. For illustration purposes the power distribution is analogously scaled as for the reanalysis data.

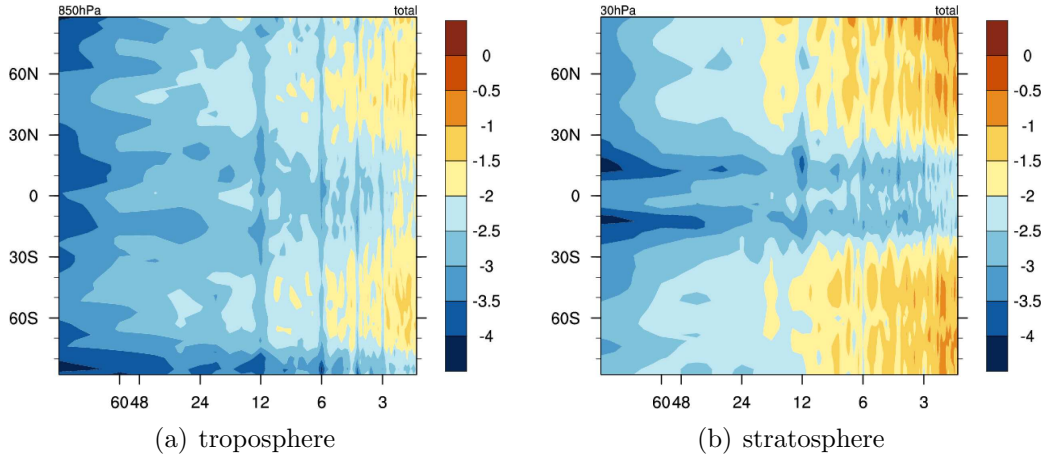


Abbildung 3.3: As Fig. 3.1 but for the residual compound of the MLR analysis. a) The tropospheric level and b) the stratospheric level.

### MiKlip Tropospheric PSA

The magnitude as well as the latitudinal distribution and in general the pattern of the variability are qualitatively in line compared to reanalysis data. The main characteristics of the tropospheric variability pattern are fairly well reproduced in the MiKlip MR and LR configuration (see Figures 3.4(a),(b)). The annual and semi-annual cycle with maximum power of  $0.5 \text{ lg}(m/s)^2 * \text{cpm}$  derived from both model configurations are similar to ERA-Interim. Furthermore qualitatively accordance to reanalysis data can be found in the extra-tropical region where the majority of intra-annual variability is located. Values here derived for the power are approximately  $-1 \text{ lg}(m/s)^2 * \text{cpm}$ . However, differences to the ERA-Interim are seen in the tropical regions. On the one hand differences arise at intra-seasonal time scales, namely for periods of around 3 months, where the simulated power tends to be overestimated compared to the reanalysis (the deviations of tropical variability on intra-seasonal time scales are discussed later in Sec. 4.1). On the other hand the power spectrum pattern deviates at long periods larger than 12 months where the ENSO signal in reanalysis data occurs. Generally variability here also tends to be underestimated compared to reanalysis data. The lower simulated power corresponding to ENSO, could be a consequence from weaknesses in the ocean model incorporated in the MiKlip system e.g. it was shown by Jungclaus et al. (2013) that the MPI-ESM, which is the underlying model of the MiKlip system, underestimates the variance spectra of ENSO for intra-decadal time scales (their Fig. 10). Variations occurring in the individual ENSO patterns of MR and LR could result from a different representation of the respective SST variability, which arises due to the different ocean model resolution of each simulation configuration in MiKlip.

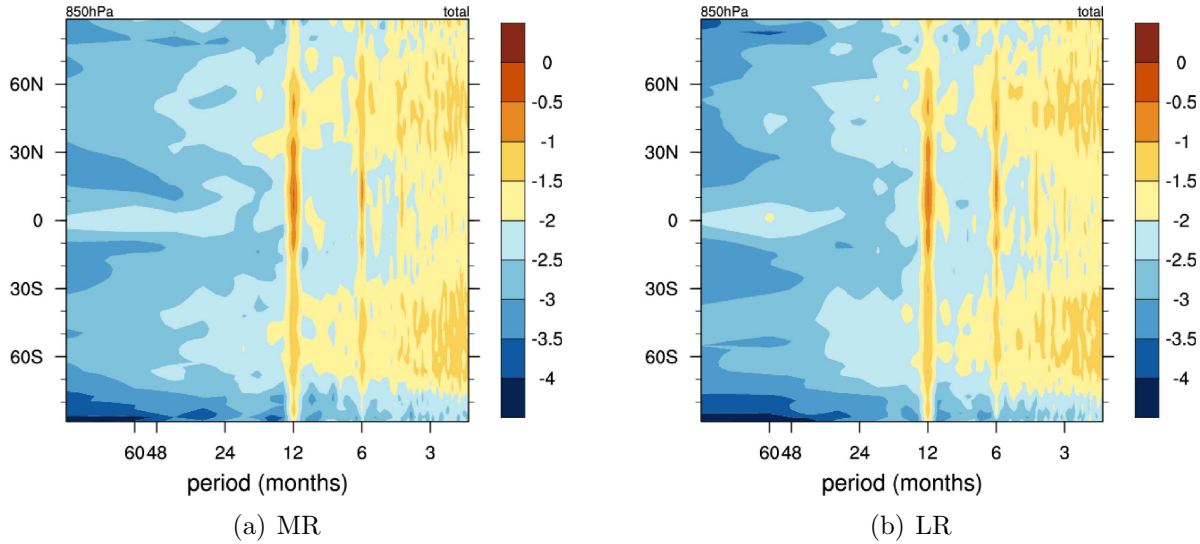


Abbildung 3.4: Power spectra of zonal wind summed over all wavelenghts for 850 hPa. a) refers to MR and b) to LR, respectively. Units are  $lg(m/s)^2 * cpm$ .

### MiKlip Stratospheric PSA

At the stratospheric level the power spectra derived from the MiKlip models (see Figures 3.5(a),(b)) give reasonable results. Most of the power is concentrated in the extra-tropical as well as in the polar region and the corresponding magnitudes are similar to those detected in ERA-Interim. However, relative large values (about  $-1 lg(m/s)^2 * cpm$ ) tend to occur more frequently than in the reanalysis data.

The power pattern in the tropics around the 24 month period, corresponding with the tropical variability of the QBO, cannot be clearly represented by both model configurations. In the low resolution model LR, the QBO pattern is not captured and the power is considerably underestimated by  $1 lg(m/s)^2 * cpm$  compared to ERA-Interim. For MR, the tropical variability of the QBO periods is larger than in LR, but values are still below those from reanalysis data. Furthermore the variablity pattern relevant for the tropical QBO region is characterised by 2 local relative maxima, which are located in the vicinity of the 24 month periods in the tropics. Qualitatively the LR version is not able to represent the pattern and amplitude of QBO variability, whereas in MR the amplitudes are closer to reanalysis, but the pattern deviates. The relatively high values of total variance here are not centred around the 24 month period like in the reanalysis data, but have two features which describe local maxima distributed around the 24 month period. A more detailed discussion of the QBO is presented later in Sec. 4.1.1.

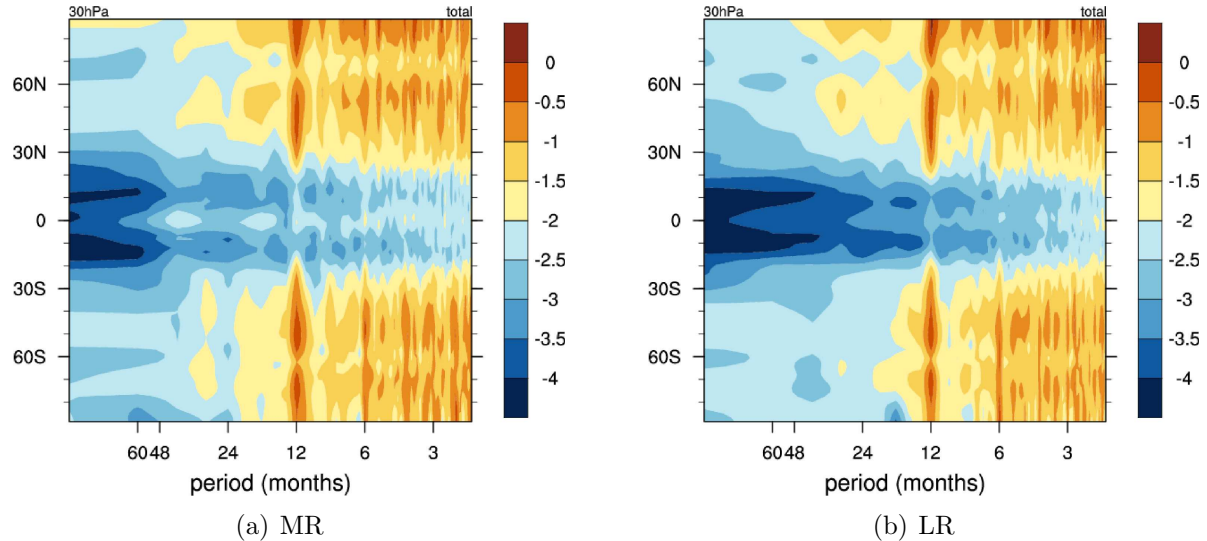


Abbildung 3.5: Power spectra of zonal wind summed over all wavelenghts for 30 hPa. a)MR and b)LR. Units are  $\text{lg}(\text{m/s})^2 * \text{cpm}$ .

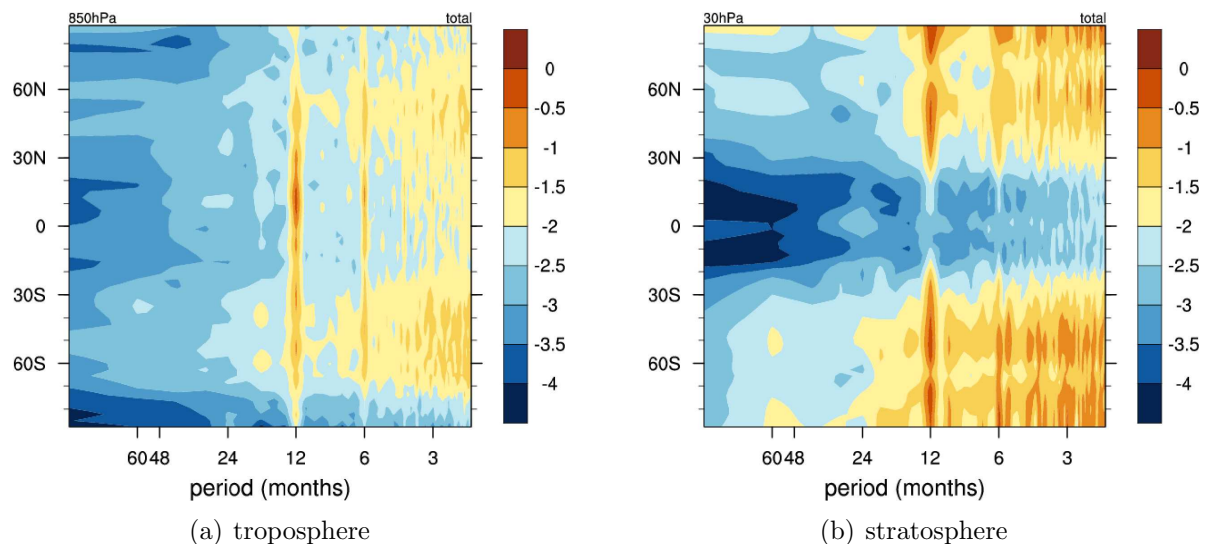


Abbildung 3.6: Power spectra of zonal wind summed over all wavelenghts for EMAC. a) 850 hPa pressure level and b) 30 hPa pressure level, respectively. Units are  $\text{lg}(\text{m/s})^2 * \text{cpm}$ .

### 3.3 Power of EMAC Simulations

The model systems EMAC and MiKlip have a related dynamical core (see Chap. 2), thus conclusions drawn with EMAC can be qualitatively compared to MiKlip. The intra-decadal PSA of EMAC is given in Fig. 3.6. Model setup here is equal to the configuration of the REF simulation described in Sec. 2.2.3 and the variability pattern is fairly well accommodated by the model in general. The characteristic features like the annual and semi-annual cycle or the relatively high intra-annual variability clustered at the mid-latitudes are captured by the model, which is in accordance with the reanalysis data. However, as with the MiKlip system, weaknesses in the representation of tropical power can be detected.

For example at the tropospheric level (see Fig. 3.6(a)) the variability pattern corresponding to the ENSO effect does not arise in the EMAC simulation. This is due to the experimental setup, i.e. in this simulation the SSTs are prescribed; application of the annual cycle derived from a 20 year average distinctly attenuates the ENSO variability, resulting in a weak corresponding power.

For the 30 hPa stratospheric level (Fig. 3.6(b)) the pattern accounting for the QBO in the tropical region at the 24 month periods can be clearly detected. However, its amplitude is considerably weaker by approximately  $0.5 \lg(m/s)^2 * cpm$  compared to the reanalysis data set. These findings could be explained by model conditions describing a combination of a well represented QBO phase but too weak QBO amplitudes. A more detailed discussion of the QBO and its driving mechanism is given in Chapter 4.

### 3.4 Summary and Discussion of Decadal PSA

A new method of illustrating intra-decadal variability by means of applying power spectral analysis was introduced in the previous sections. To my knowledge this application of Hayashi's PSA on a decadal time scale has not been described in literature yet. It is demonstrated that this approach of utilising the PSA for decadal time scales gives reasonable results. The variability patterns are characterised by 2 prominent peaks at 12 and 6 months representing the annual and semi-annual cycle. Furthermore, most of the power can be found at periods shorter than one year and at geographical locations around the mid-latitudes reflecting the activity of storm tracks in the troposphere or the polar vortex at the stratospheric level, respectively.

Furthermore, external / deterministic variability such as ENSO or QBO can be captured, which is verified by MLR analysis. For example, the variability pattern detected in the tropical tropospheric region at periods larger than 12 months can be attributed to the effects of ENSO. Furthermore, the MLR analysis reveals that variability in particular of the 24 months period is distinctly influenced by the QBO. For the tropics the effects of the QBO contributes up to 80% to total variability, but also in the high-latitudes up to 70% of total variability is determined by the QBO. Implications of the QBO on higher latitudes is also commonly known as the 'Holton and Tan effect' (Holton and Tan, 1980).

On the other hand, the power of shorter intra-annual time scales (periods shorter than

12 months) show a dominant contribution of internal variability. Internal variability was determined by the residuum of MLR analysis. So generally it can be stated that for intra-decadal time scales, deterministic variability tends to be more relevant for periods larger than 12 months, whereas internal variability is the more important factor for time scales shorter than 12 months.

With this new approach the decadal variability of numerical models can be analysed. Applying decadal PSA to model simulations gives a qualitatively good representation of the variability pattern compared with the ERA-Interim reanalysis data set. However, in all regarded model systems difficulties occur. For example, concerning the power spectra distribution of tropical external / deterministic variability shortcomings in the numerical simulations are identified. By means of MLR analysis these model deficits are attributable to the effects of ENSO. For EMAC this is explained by the experimental setup, which utilise a SST climatology and thus the ENSO signal is considerably attenuated and do not arise in the power pattern. In contrast in the numerical model configurations of MiKlip weaknesses of simulating variability of ENSO as it is incorporated within the ocean model (Jungclaus et al., 2013) results in detected difference of the decadal PSA.

At the stratospheric level, 'external variability' of decadal PSA is marked by the QBO. Its variability pattern can only be qualitatively captured by the models with high vertical resolution (i.e MR and EMAC), whereas in the low resolution model this QBO signature is missing. The experimental studies of Giorgetta et al. (2006) inferred that this is due to the fact that high vertical resolution (approximately less than 1 km) is necessary to simulate a QBO-like oscillation comparable to observation. It is discussed that a coarser resolution with less levels in the vertical could lead to 'numerical induced diffusion', resulting in a wave momentum into the stratosphere, that is not sufficient to generate internally a QBO (Bunzel, 2013). Further discussion on the representation of the QBO and its driving mechanism can be found in Chapter 4.

A quantitative discussion of simulated decadal PSA is given below. The data in Fig. 3.7 provides the relative differences of the decadal PSA between the corresponding simulations and ERA-Interim. Negative values refer to an overestimation of variability by the models compared to reanalysis data and positive anomalies to an underestimation.

At the tropospheric level, the anomaly patterns derived from the model simulations evince a great similarity between each other (see Fig. 3.7a,c,e). Their largest deviations to ERA-Interim are predominantly situated in periods shorter than 6 months. But also a characteristic feature with relatively strong anomalies at the 12 months periods arises. Differences here can locally exceed 20%. In general anomalies within the 6 months period are dominated by negative values up to 10% relative difference. However, in the polar regions positive anomalies can also occur, in particular the Arctic region is characterised by positive relative differences.

For the tropical ENSO variability pattern, at periods larger than 12 months positive deviations of up to 10% can be detected locally. This under representation of ENSO variability can be most clearly seen in the EMAC simulation. As stated above this is due to its experimental design.

In the stratosphere the main differences in the PSA pattern emerge in the extra-tropical

regions, at periods shorter than 12 months (see Fig. 3.7b,d,f). Compared to the relative differences detected in the troposphere anomalies here are larger with values around 30%. Moreover, there is no clear predominance of negative or positive values. Sparse local anomaly peaks, exceeding more than 100% also could be a consequence of uncertainties in the spectral regridding preprocesses and therefore can be neglected. Regridding is necessary since reanalysis data and models have different horizontal resolutions.

Looking at the equatorial region, all models underestimate variability larger than 6 months. In particular at the QBO period of around 24 months, positive anomalies can be detected. Since the driving mechanisms of the QBO are acting on time scales significantly shorter than 2 years, anomalies arising at periods less than 24 months could be affected by problems with these driving mechanisms. In accordance with the above discussed findings, the largest deviations between reanalysis and models occur for LR which underestimates the tropical QBO variability of ERA-Interim by 15%, but also the Holton and Tan effect can be demonstrated in the anomaly pattern, where an underestimated tropical QBO also affects higher latitudes at the same period, e.g. relatively strong deviations of around 20% can be found in the Arctic region of the Northern hemisphere.

Staying in the Northern hemispheric mid- to high-latitudes the intra-annual variability in EMAC is mainly underestimated compared to ERA-Interim, which is reflected by positive anomalies of up to approximately 30%. Bearing in mind that wave mean flow interaction contributes considerably to atmospheric variability, underestimated vertical propagating waves from the troposphere would consequently lead to lower stratospheric variability. Therefore regarding the corresponding anomaly pattern at tropospheric levels, likewise in accordance to the stratosphere, predominantly negative differences are obtained.

In the Southern hemisphere the anomaly pattern tends to be dominated by negative values around 20%. However positive anomalies can be found, in particular at 60°S. The vicinity of the 60°S is also known to be a hot spot for orographic gravity waves, induced by the overflow of the Southern Andes and therefore deviations arising here could be related to possible problems with the representation of small scale orographic gravity waves.

Considering the MiKlip system both models qualitatively reflect a similar positive anomaly (Fig. 3.7d,f). The amplitudes of the anomaly pattern are comparable to EMAC, however, for the Northern hemisphere the anomalies are stronger and whereas in the Southern hemisphere positive anomalies are more pronounced compared to EMAC.

In general these relatively large deviations in the polar regions derived by the PSA give a strong indication that model dynamics, which plays a major role in representing variability, are challenged by some problems. For example, it is demonstrated that EMAC suffers from a Southern hemispheric polar vortex that is too 'weak'. This is reflected in zonal wind speeds that are too low during winter and spring, which leads to a warm bias accompanied by less ozone depletion (see Deckert, 2012; Khosrawi et al., 2009). Further studies are needed to explain the possible causes and their underlying processes as they related to the anomaly patterns of intra-decadal variability. Analyses are therefore carried out in more detail in Chapter 4, with a focus on the tropical as well as on the Southern hemispheric polar region.

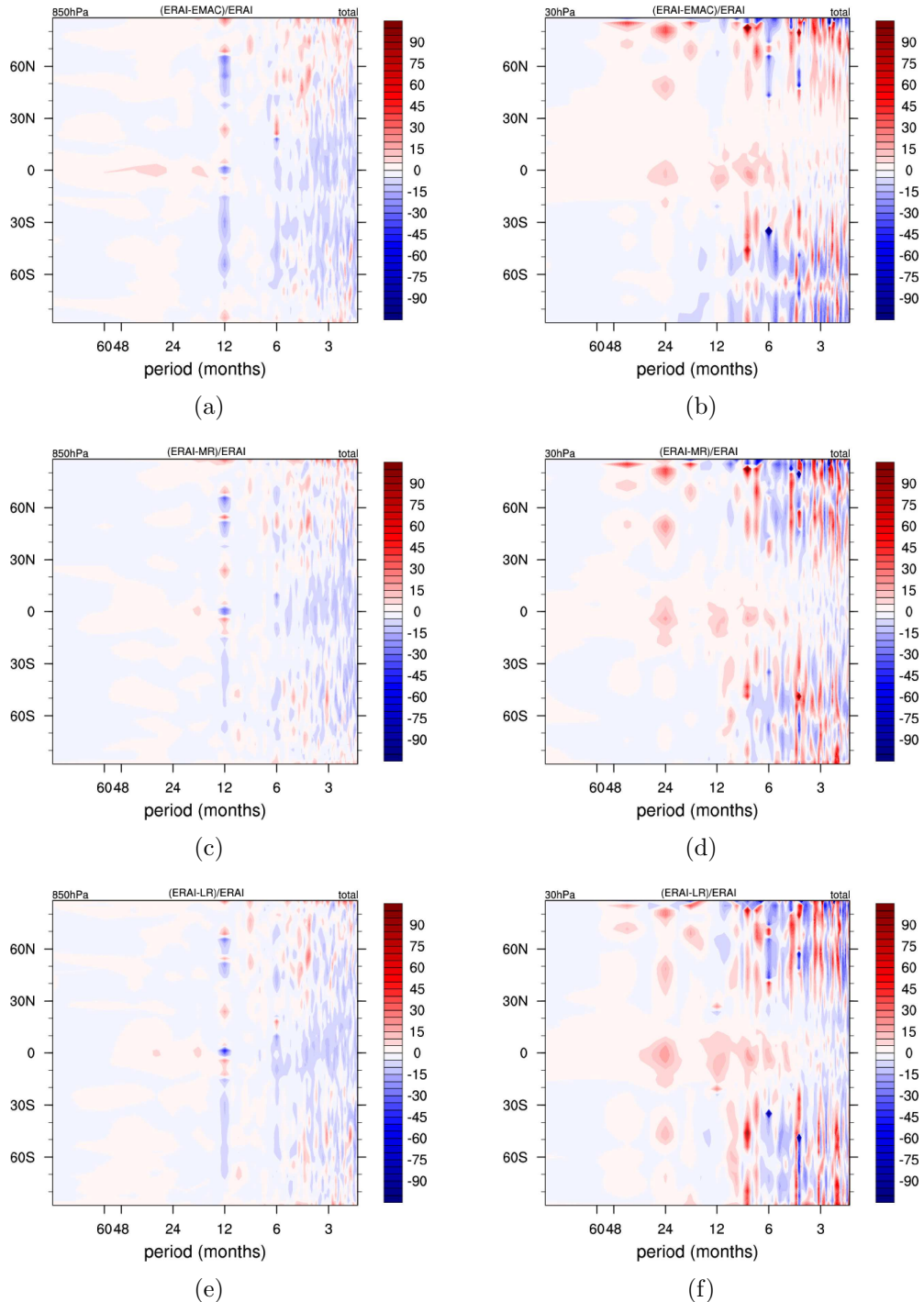


Abbildung 3.7: Relative differences of decadal power distributions between ERA-Interim and models given in %. Top row EMAC, middle MR and bottom LR. Left column 850 hPa and right 30 hPa.

# Kapitel 4

## Intra-Seasonal Variability

The previous Chapter identified that simulated stratospheric variability is particularly challenged on the one hand in the tropics by the representation of the QBO and on the other hand in the region of the polar vortices. In particular, in the Southern hemispheric polar vortex region in EMAC the variability is considerably overestimated. Both atmospheric features, QBO and polar vortices are characterised by atmospheric waves, whose temporal scales typically coincide with seasonal time horizons. Therefore the focal point of this chapter is on the diagnostics of intra seasonal variability and their underlying processes. The regions of interest are the tropics and the Southern hemispheric polar region, respectively.

### 4.1 Tropical Variability

#### 4.1.1 The QBO

In this section the QBO and its drivers are analysed. The Figures 4.1(a) to 4.1(d) give an altitude-time cross section of tropical zonal mean zonal wind covering the vertical domain from the mid stratosphere to the UTLS region (roughly from 100 hPa to 10 hPa). This illustration method typically represent the characteristics of the QBO. In the low vertical resolution model LR no oscillation can be detected and the wind field is dominated by weak easterlies (see Fig. 4.1(d)). Only the model configurations with high vertical resolution such as REF and MR (see Fig. 4.1(b) and 4.1(c)) are capable of reproducing a QBO or at least a QBO-like pattern comparable to the reanalysis data illustrated in Fig. 4.1(a). In the REF simulation the QBO pattern is qualitatively well represented but the wind amplitudes below the 30 hPa level tend to be underestimated. Deviations in the easterlies as well as in the westerlies can reach up to  $4 \text{ ms}^{-1}$ . In the MR model differences, especially in the representation of the QBO pattern are even more clearer, in particular the downward propagation and the oscillation period compared to ERA-Interim is not well captured, e.g. the duration of the easterly phase at 20 hPa can last from 2 to 4 years, or at 50 hPa prevailing westerlies are interrupted by short, half a year lasting, easterly episodes.

After Giorgetta et al. (2002) it is inferred that a broad spectrum of atmospheric waves

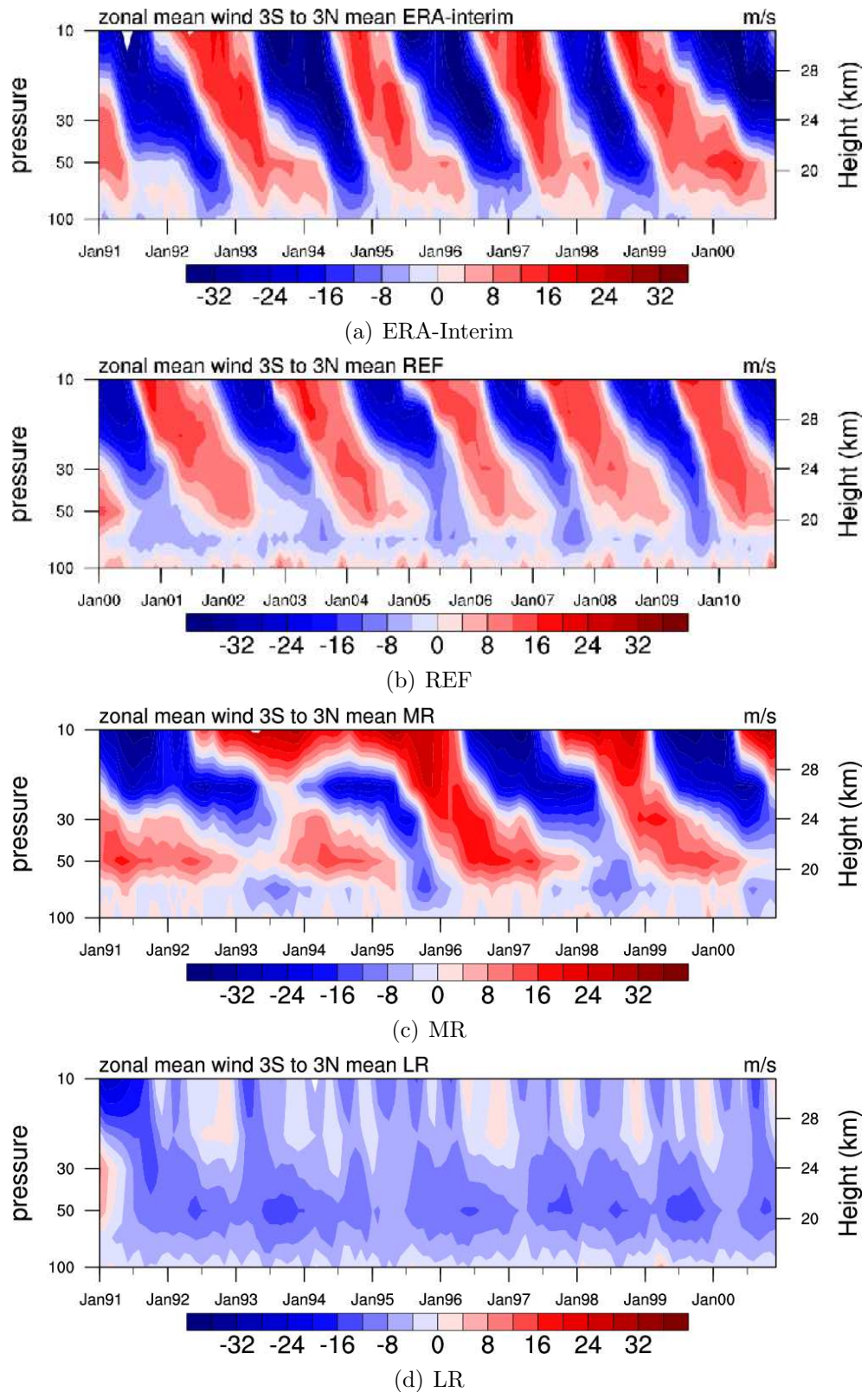


Abbildung 4.1: Altitude-time cross section of monthly mean, zonal mean, zonal wind for tropical latitudes ( $3^{\circ}$  N to  $3^{\circ}$  S) and 100 hPa to 10 hPa level given in m/s, representing the QBO signal.

are required in order to internally generate a QBO in the models. As discussed in Sec. 1.1.3 vertical propagating Kelvin and MRG waves significantly contribute to the necessary momentum for the driving mechanism of the QBO. Significant contributions of these types of waves are largely not resolved by the models and need to be parameterised (Giorgetta et al., 2002, 2006). Therefore, the simulation of the QBO is strongly dependent of an adequate implementation of these atmospheric waves and deficits in the models pointed out above are very likely due to insufficient representation of these waves.

Analysis and discussion of the representation of MRG and Kelvin waves by the different numerical models are carried out in the subsequent sections.

### 4.1.2 PSA following Wheeler et al.

To analyse equatorial waves, the PSA following the procedure described in Wheeler and Kiladis (1999) is applied. This method decomposes the atmospheric field into a symmetric and an antisymmetric portion in order to capture the characteristics of MRG and Kelvin waves. The terms symmetric and antisymmetric are referenced spatially to the equator, since geometrical properties of e.g. tropical MRG waves are arranged antisymmetrically to the equator, whereas Kelvin waves have a symmetric appearance. The theoretical background of this method can be found in the Appendix A.

Similar to the decadal PSA and to preserve comparability all input fields were regredded to the lowest available vertical resolution of T42. The applied input time step for the PSA is 6 hours meaning the shortest resolvable period is 12 hours. For each simulation a ten year temperature data set at 30 hPa is partitioned into consecutive 96-day segments. Each of these segments are first detrended and then the PSA is applied for the equatorial symmetric and antisymmetric fractions. Eventually the power is averaged over all symmetric as well as antisymmetric segments for the tropical latitudes from 15°N to 15°S. Details on the decomposition and the PSA method can be read in the Appendix A.

The resulting raw power spectra and the corresponding background power are given in Fig. 4.2. The background is calculated by the sum of antisymmetric and symmetric power by smoothing frequency and wavenumber with a 1-2-1 filter (details described in Wheeler and Kiladis, 1999). This smoothing is an attempt to eliminate any periodic signatures in the power pattern, which ideally gives a remaining power spectrum consisting of only random and non-periodic processes and hence representing background noise. For interpretational purposes the dispersion curves are overlayed resulting from the equatorially trapped wave solutions approximated by the linear shallow water equations on an equatorial  $\beta$  plane, which were described in Matsuno (1966). Each wave type (i.e. equatorial Rossby wave with  $n = 1$  for the symmetric and  $n = 2$  for the antisymmetric component, Kelvin wave with  $n = 1$  and MRG wave with  $n = 0$ ) is represented by three different equivalent depths  $h_e$  of 10 m, 50 m and 250 m. The  $n$  is the equatorial meridional mode number introduced by Matsuno (1966), which sets a specific solution of the corresponding dispersion relations of the equatorial wave types.

Both raw power spectra differ fundamentally in their pattern. In the symmetric component (see Fig. 4.2(b)) most of the power is situated at small wavenumbers ( $< 5$ ) and high

periods (6 to 30 days), which are characteristic scales for planetary and synoptic waves. A clear domination of eastward propagating waves can be seen. Their power is accumulated between the dispersion curves of Kelvin waves with equivalent heights of 50 m to 250 m and the amplitudes are decreasing with increasing wavenumbers and frequencies, respectively. But also westward travelling waves can be detected, which are mainly located along the dispersion curves of equatorial Rossby (ER) waves with small wavenumbers (-5 to -1).

The antisymmetric fraction is given in Fig. 4.2(a). In contrast to the symmetric component the majority of the power is accumulated within the westward propagating waves and their distribution can be well captured by the dispersion curves of MRG and ER waves. One maximum is located at planetary scale ER waves with periods of approximately one month (corresponding to frequencies of about 0.1 cpd; cycle per days) and small wavenumbers (wavenumbers 1-3). But most of the variability can predominately be found within the dispersion curves of MRG waves with equivalent depths of 250 m to 50 m and periods between 3 and 6 days (corresponding to 0.2-0.4 cpd).

The pattern of the background power (Fig. 4.2(c)) qualitatively shows the characteristics of red noise, which means that power decreases with increasing wavenumber and frequency. A red background spectrum seems to be very reasonable. For example, Holton (1973) determined a red background for the tropical lower stratosphere arising from the observations of Kelvin waves. Furthermore theoretical studies in the work of Von Storch and Zwiers (2001) could confirm red noise characteristics of the background conditions of stratospheric processes.

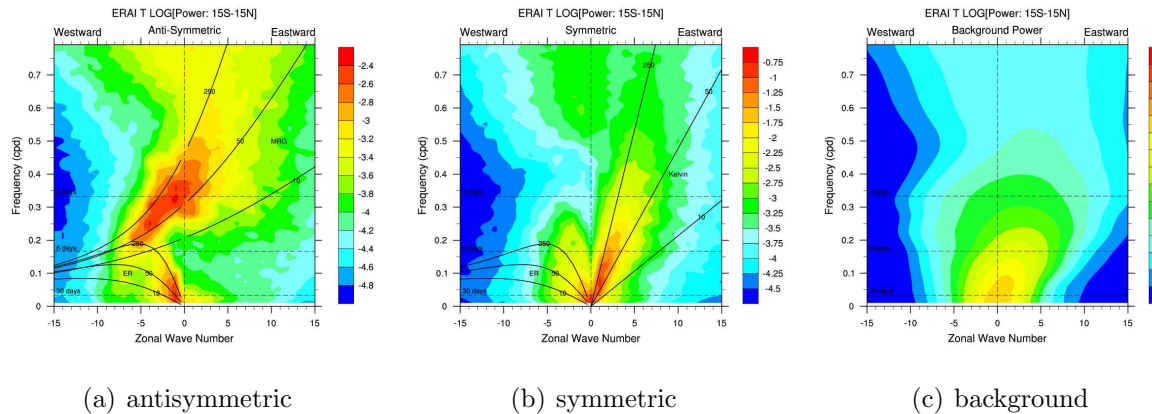


Abbildung 4.2: Raw and background power of tropical ( $15^{\circ}\text{N}$  to  $15^{\circ}\text{S}$ ) temperature at 30 hPa given in  $\lg K^2$ . Overlayed are constant periods of 3, 6 and 30 days (horizontal dashed lines) and dispersion curves for MRG waves with  $n = 0$  and Kelvin waves with  $n = 1$ . ER waves with  $n = 1$  for the antisymmetric and  $n = 2$  symmetric component, respectively. The applied equivalent depths are 10 m, 50 m and 250 m (solid lines).

For statistical considerations and for a clearer representation of MRG and Kelvin waves only the relative power is displayed in the following. Relative power is derived from the raw power spectrum which is normalised at each wavenumber and frequency by the cor-

responding background power. In this work the theoretical absolute number of degrees of freedom (*dof*) is 2 (space and time)  $\times$  10 (latitudes)  $\times$  10 (years)  $\times$  365/96 (time segments length)  $\approx$  760. Regarding the corresponding symmetric and antisymmetric spectra and considering that the latitudes are not independent from each other, a very conservative estimate for the respective *dof* would be 76 (2 (space and time)  $\times$  1 (latitude)  $\times$  10 (years)  $\times$  365/96 (time segments length)). After Warner (1998) a relative power of approximately 1.2 (and under the assumption of 76 *dof*) can be assessed to a 90% significance level. This implies that signatures arising in the ratio of raw power to background power exceeding values larger than 1.2 are statistically distinguishable from the background.

The antisymmetric fraction of relative power for stratospheric temperature at 30 hPa derived for ERA-Interim and the individual numerical models is given in Figures 4.3(a) to 4.3(d). Superimposed are the dispersion curves for MRG waves with equivalent depths of 250 m, 50 m and 10 m. It can be seen in the reanalysis data (Fig. 4.3(a)) that significant variability is clearly organised within the dispersion curves of MRG waves with equivalent depths of 250 m to 50 m. The corresponding relative power in the REF simulation compares fairly well to ERA-Interim (see Fig. 4.3(b)). Similar to the reanalysis power distribution, most of the significant signals can be found by the dispersion curves of MRG with 250 m and 50 m. But the modeled power is more 'compact' meaning the frequency bandwidth covered by significant patterns, is smaller compared to ERA-Interim.

In the MiKlip models MR and LR this 'compact' characteristic is even more pronounced (see Fig. 4.3(c) and Fig. 4.3(d)). The significant relative power is predominately situated within the dispersion curves of MRG waves with equivalent depths of 250 m to 10 m, periods between 6 and 30 days and wavenumbers from approximately -1 to -5, which is distinctly different to ERA-Interim. Furthermore, the relative power in LR is relatively weak, the maxima are almost only half of the values derived from the reanalysis data.

In Figures 4.4(a) to 4.4(d) the relative power of the symmetric component is presented. The dispersion curves of Kelvin waves with equivalent depths of 250 m, 50 m and 10 m are overlayed. As seen in ERA-Interim the majority of the significant fraction of symmetric power can be attributed to Kelvin waves with equivalent depths of 250 m to 50 m. All models, from a qualitative perspective, can identify this characteristic well. A good comparison of relative symmetric power is given in the REF simulation. However, the power of Kelvin waves with frequencies larger than 0.2 cpd tends to be underestimated. In the MR and the LR models attenuation of variability of the Kelvin waves is even more pronounced. Especially in the LR simulation maximum, where relative power can predominantly be found at periods longer than 6 days, whereas in ERA-Interim these values also expand to shorter periods of 3 days.

It appears to be that all analysed models can capture the variability of Kelvin waves qualitatively well. However, for the representation of MRG waves, models with a higher vertical resolution have an advantage over lower vertical resolution models.

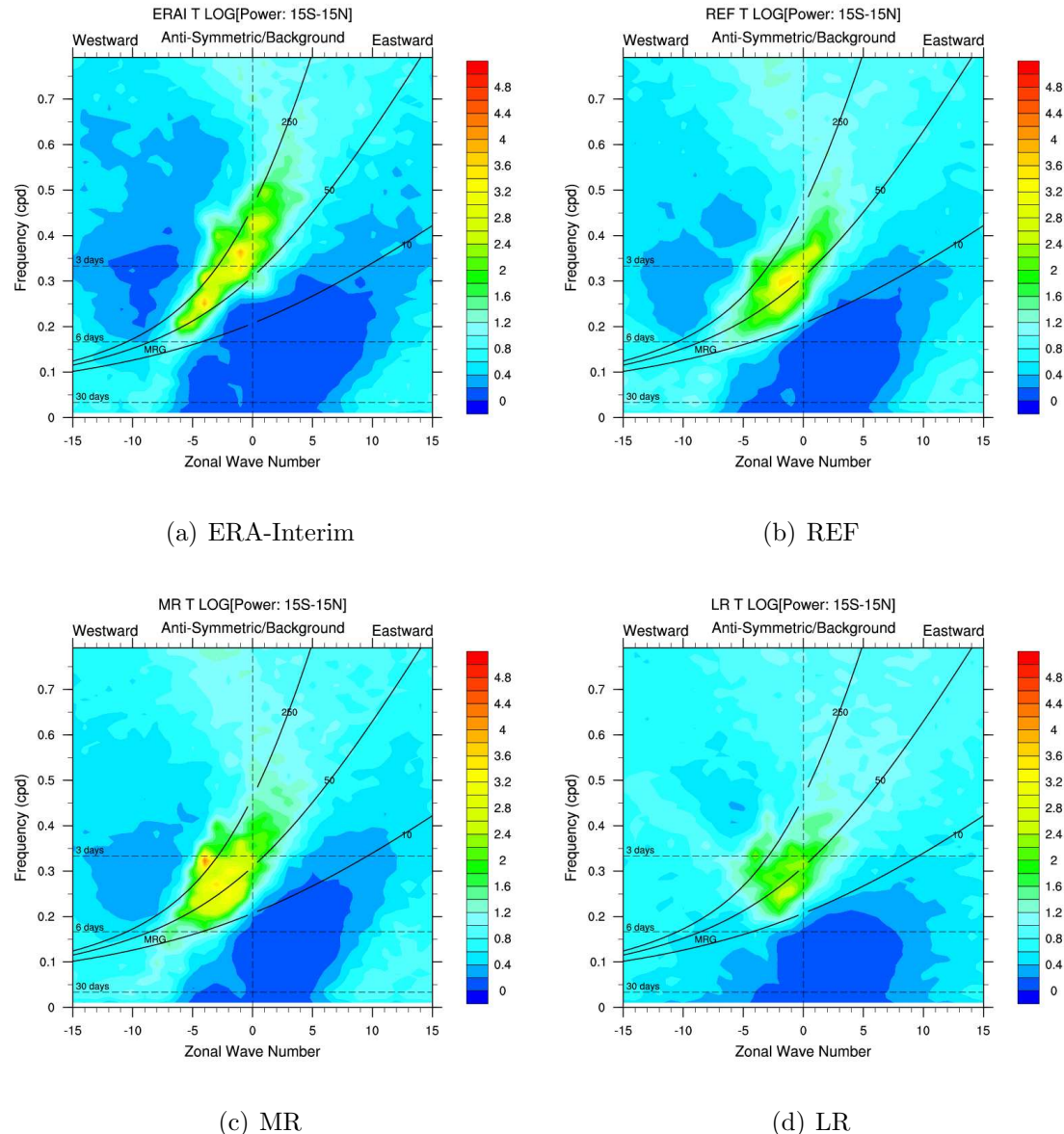


Abbildung 4.3: Antisymmetric component of relative power spectra of tropical ( $15^{\circ}N$  to  $15^{\circ}S$ ) temperature at 30 hPa. Overlayed are constant periods of 3, 6 and 30 days (horizontal dashed lines) and dispersion curves for MRG waves with  $n = 0$  calculated for the equivalent depths of 10 m, 50 m and 250 m (solid lines). Colours give the dimensionless value of the ratio between raw and background spectrum. See text for details.

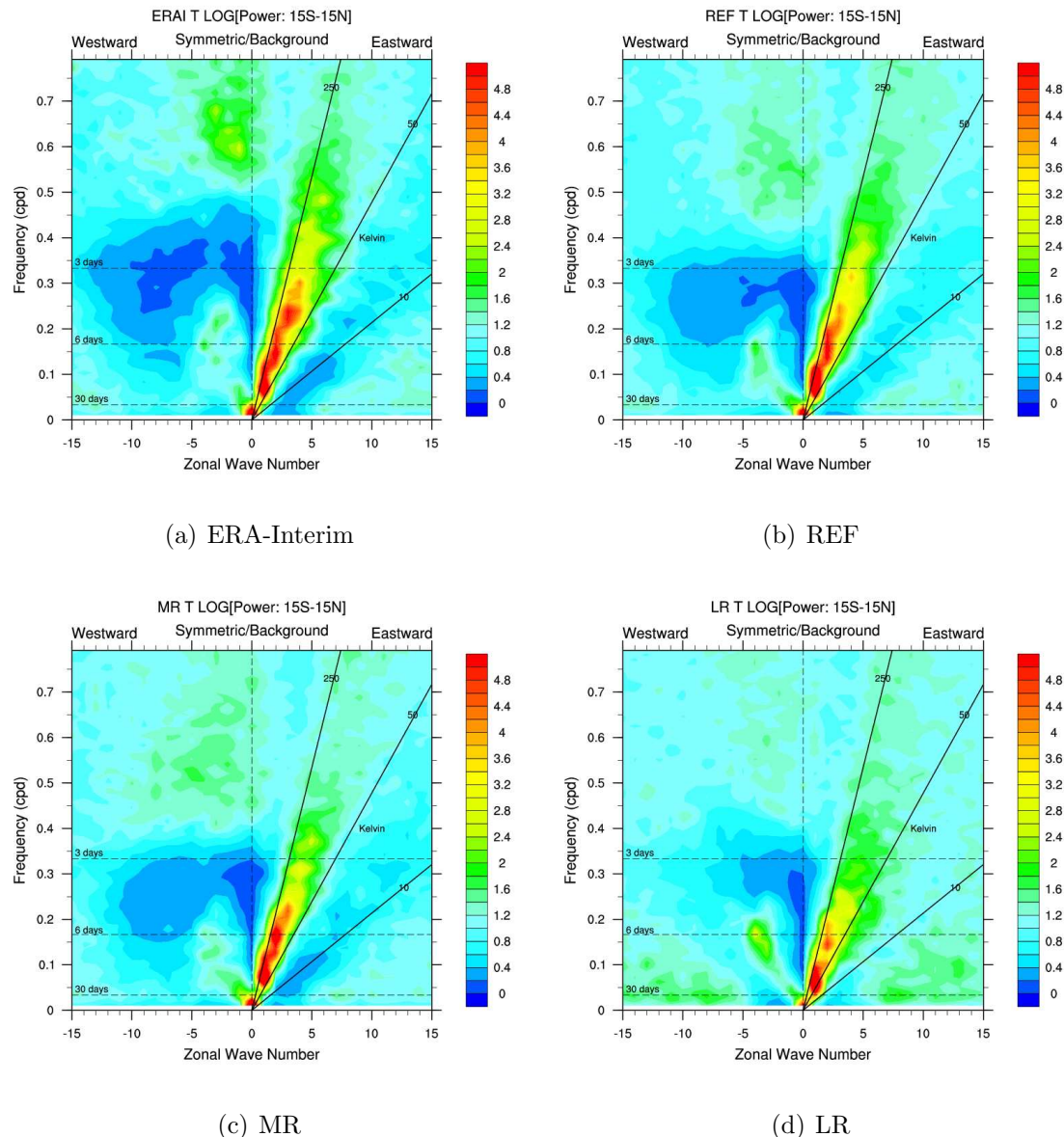


Abbildung 4.4: Symmetric component of relative power spectra of tropical ( $15^{\circ}\text{N}$  to  $15^{\circ}\text{S}$ ) temperature at 30 hPa. Overlayed are constant periods of 3, 6 and 30 days (horizontal dashed lines) and dispersion curves for Kelvin waves with  $n = 1$  calculated for the equivalent depths of 10m, 50m and 250m (solid lines). Colours give the dimensionless value of the ratio between raw and background spectrum. See text for details.

### 4.1.3 Discussion of the QBO

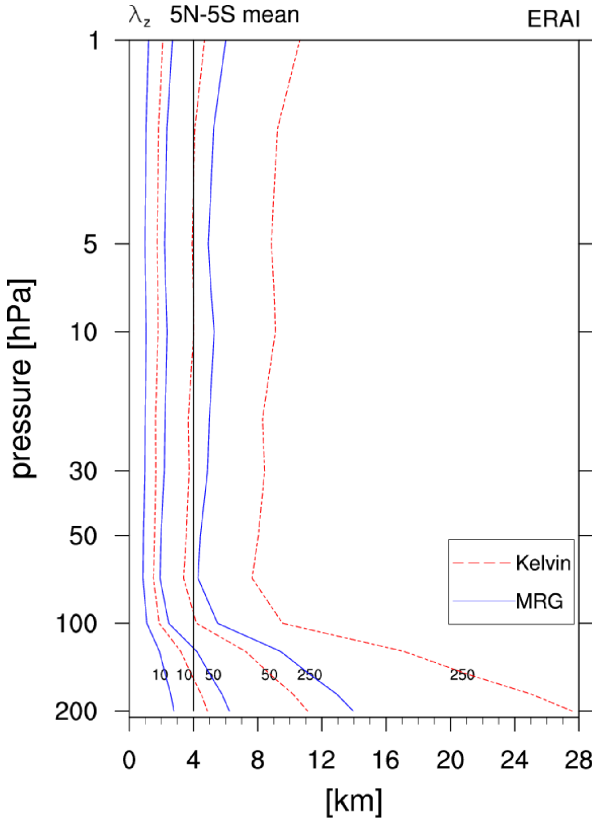


Abbildung 4.5: Vertical distribution of vertical wavelengths  $\lambda_z$  of Kelvin and MRG calculated from ERA-Interim following linear wave theory after Andrews et al. (1987). See text for details.

corresponding wavenumbers cover a smaller range, predominately to be found at low values (-1 to -5). In the MR model this characteristically altered power spectrum of MRG waves contributes to a distorted QBO signal, particularly reflected in an irregular QBO period (see Fig. 4.1(c)). In the case of the LR simulation not only the distribution of relative power of MRG waves are considerably different to ERA-Interim, but also the significant absolute values are comparatively small and tend to be only half as large as in the reanalysis data. This under representation of MRG waves in the LR model is thus very likely to be the reason, why no alternation of easterly and westerly regimes in the tropical lower stratosphere can be generated.

In addition, Giorgetta et al. (2006) pointed out by numerical experiments, that a vertical resolution of at least 1 km is necessary for in order to simulate a QBO signal in a GCM, but specific explanations or reasons for this fact remain unclear. Recalling the vertically resolution of LR, which is on average approximately 2 km, the inability of the LR model

As demonstrated above, solely the models with high vertical resolution such as REF and MR are capable of reproducing tropical variability comparable with the QBO signal seen in the ERA-Interim data, but in the lower vertical resolution model only weak easterlies can be detected. To determine possible causes, Kelvin and MRG waves, the main drivers of the QBO are analysed by means of the PSA adapted to the method of Wheeler and Kiladis (1999). The variability of the QBO is quite well depicted in the REF simulation, which is not only reflected in the zonal mean zonal wind cross sections, but which also can be seen in the distribution of relative power derived by the PSA. Especially the pattern of Kelvin and MRG waves derived from the power spectra in the REF simulation which are in a qualitatively good agreement to reanalysis data.

Regarding the MiKlip simulations MR and LR, both models can give a qualitatively good representation of Kelvin waves but shortcomings particularly in the variability pattern of MRG waves are identified. The distribution of the relative power for MRG waves differs considerably from ERA-Interim.

The frequency bandwidth is narrower and the

wavenumbers cover a smaller range, predominately to be found at low values (-1 to -5). In the MR model this characteristically altered power spectrum of MRG waves contributes to a distorted QBO signal, particularly reflected in an irregular QBO period (see Fig. 4.1(c)). In the case of the LR simulation not only the distribution of relative power of MRG waves are considerably different to ERA-Interim, but also the significant absolute values are comparatively small and tend to be only half as large as in the reanalysis data. This under representation of MRG waves in the LR model is thus very likely to be the reason, why no alternation of easterly and westerly regimes in the tropical lower stratosphere can be generated.

In addition, Giorgetta et al. (2006) pointed out by numerical experiments, that a vertical resolution of at least 1 km is necessary for in order to simulate a QBO signal in a GCM, but specific explanations or reasons for this fact remain unclear. Recalling the vertically resolution of LR, which is on average approximately 2 km, the inability of the LR model

to generate a QBO confirms their findings.

Following linear wave theory (e.g. Andrews et al., 1987; Matsuno, 1966; Lindzen, 1967; Lindzen and Matsuno, 1968) the vertical wavenumber  $m$  for zonally and vertically propagating equatorial waves are given as

$$m = \frac{2\pi}{\lambda_z} = \left( \frac{N^2}{gh} - \frac{1}{4H_s^2} \right)^{1/2}, \quad (4.1)$$

where  $\lambda_z$  is the vertical wavelength,  $N^2 = -p/H_s \theta * \partial\theta/\partial p$  is the buoyancy frequency squared,  $g$  is the acceleration of gravity,  $h$  the equivalent depth,  $H_s$  is the scale height and  $\theta$  is potential temperature.

Bearing in mind Kelvin waves accounting for the eastward acceleration, predominantly occur in westerlies regimes whereas corresponding westward MRG waves responsible for westward momentum can mainly be found in easterlies. The calculation of vertical wavelengths following Eq. 4.1 distinguishes between eastward and westward wind regimes. Calculated wavelengths considering solely values during phases of westerlies are assigned to Kelvin waves and analogous wavelengths derived during the phases of easterlies are assigned to MRG waves. Following this concept Fig. 4.5 gives the vertical distribution of  $\lambda_z$  of Kelvin and MRG waves calculated for 10 m, 50 m and 250 m equivalent depth for ERA-Interim. With growing equivalent depths, the vertical wavenumbers increase. The  $\lambda_z$  of Kelvin waves are larger than the  $\lambda_z$  of MRG waves, which corresponds to the findings of Boville and Randel (1992). Regarding stratospheric levels relevant for the QBO,  $\lambda_z$  for MRG waves with  $h = 250$  m are about 4 km and MRG waves with  $h = 50$  m are about 2 km, respectively. Between these equivalent heights from 250 m to 50 m the majority of significant power of Kelvin and as well as MRG waves are located, which is shown above in corresponding PSA. Therefore, a vertical model resolution of at least 1 km is necessary to resolve the major part of stratospheric equatorial variability forced by Kelvin and MRG waves. Furthermore, by means of linear wave theory the empirical findings of Giorgetta et al. (2006) can be confirmed, where they determined the minimum required vertical resolution for an internally driven QBO with numerical experiments.

In the context of the decadal forecasts system, it is demonstrated that the QBO contributes considerably to intra-decadal variability. Therefore, a good representation of the QBO and its underlying processes are absolutely required. This implies that high vertical resolution is mandatory for decadal climate prediction systems.

#### 4.1.4 The SAO

Extending the previous analysis of the QBO vertically up to 0.1 hPa, which is the upper model lid of MiKlip simulations and ERA-Interim, a further atmospheric feature namely the SAO can be detected. Its dynamical forcings have similar aspects compared to the mechanism described for the QBO. But in contrast to the QBO where Kelvin and MRG waves contribute the momentum, the SAO can be additionally forced by inertio-gravity waves and also in particular by planetary scale waves, which are resolved by the models.

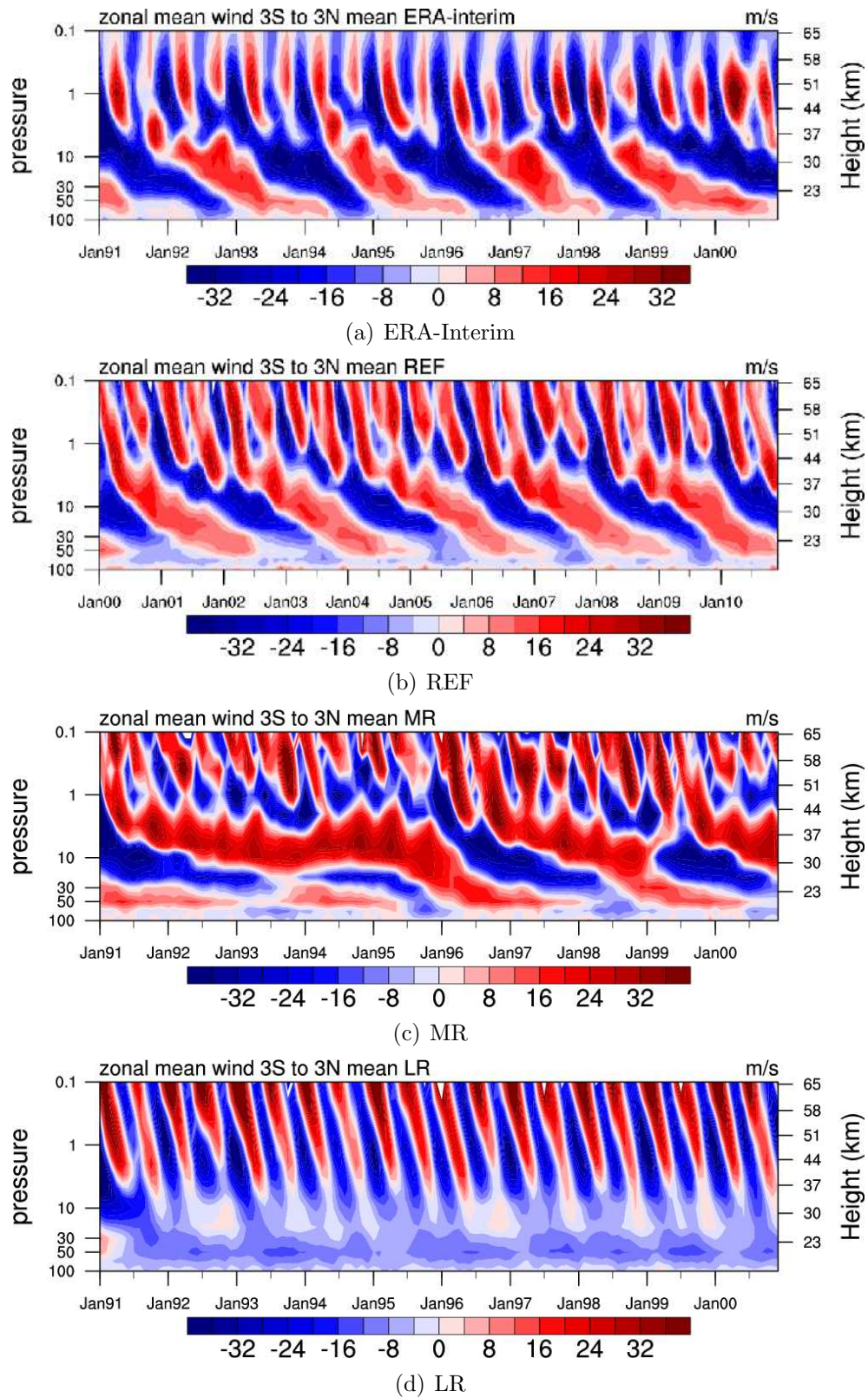


Abbildung 4.6: Same as Fig. 4.1 but for vertical levels from 100 hPa to 0.1 hPa given in m/s, representing the QBO and SAO signal.

The westerly phase is considered to be driven by large-scale Kelvin waves whereas the easterlies are driven on the one hand by planetary waves advected during solstice seasons (Hirota, 1980) and on the other hand also small-scale inertio-gravity waves contribute considerably to an acceleration of easterlies (Sassi and Garcia, 1997; Garcia, 2000).

In principle all analysed models are capable of reproducing some kind of a SAO-like pattern (see Fig. 4.6). But compared to ERA-Interim substantial deviations in the modelled Semi-Annual Oscillation arise. The REF simulation, which also could fairly well represent the QBO, is able to generate a qualitatively good representation of the SAO variability. Alternating westward and eastward zonal mean wind expanding from the mesosphere to the upper stratosphere with  $\sim 6$  months period can be seen. But the easterlies are underestimated and hence the westerly phase is dominating the SAO pattern (see Fig. 4.6(b)).

In the MR model the SAO signature is much more distorted, e.g. this is reflected by the individual phases of the SAO. They seem not be able to span the vertical extent of the mesosphere and upper stratosphere. The easterlies are mainly concentrated at around 1 hPa forming a 'horizontal band' (see Fig. 4.6(c)).

Regarding the low resolution simulation, which could not reproduce the QBO, a very regular SAO signature arises. The maximum easterlies tend to occur at lower altitudes around 5 hPa whereas the relatively strong westerlies are located at higher levels at 0.1 hPa. In contrast to the reanalysis data both wind regimes here have a relative clear tilt which corresponds with a downward propagation of the respective wind regime with time. In ERA-Interim changes of the wind field can appear abruptly which can be seen by an instantaneous switch of wind direction throughout the whole vertical extent of upper stratosphere and lower mesosphere.

#### 4.1.5 Discussion of the SAO

An interaction of SAO and QBO is demonstrated by several studies. Depending on the QBO phase, only certain wave spectra can pass the lower stratosphere. The remaining momentum is then available to drive the SAO (e.g. Mayr et al., 2010). Thus, it is not surprising that the REF simulation, with a qualitatively well representation of the QBO, is also able to reproduce a SAO signal comparable to ERA-Interim and respectively the MR with a distorted QBO reflects a SAO pattern with stronger deviations to reanalysis data.

Nevertheless, drawbacks in the representation of the easterlies in the REF simulation, especially during Northern summer months June-July-August (JJA), can be detected. This could be related to the issue the models suffer from capturing the variability of the polar vortex (see Sec. 3.4), since the properties of the polar vortex are strongly influenced by extra-tropical wave forcing, which also partly accounts for driving the mean meridional circulation. The mean meridional circulation is considered to provide easterly momentum contributing to the easterly phase of the SAO. The tropical mean meridional wind at stratopause level can be regarded as a proxy for the strength of the cross equatorial easterly momentum advection as described in Holton and Wehrbein (1980). In all models the mean

annual cycle of meridional wind are very similar (see Fig. 4.7). Especially during JJA the models clearly overestimate the wind speed by 0.5 m/s compared to ERA-Interim, meaning the modelled advection of easterly momentum is enhanced. Thus this effect cannot explain the underestimation of the easterly SAO phase in the REF simulation.

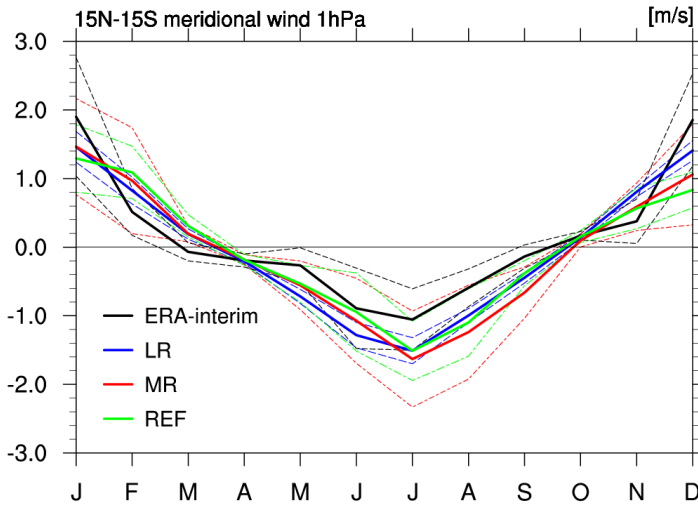


Abbildung 4.7: Tropical ( $15^{\circ}N$  to  $15^{\circ}S$ ) mean of meridional wind component at 1 hPa given as m/s. Positive values indicating northward and negative values indicate southward direction, respectively. Dashed lines denote the corresponding  $1\sigma$  standard deviation.

But regarding the one  $\sigma$  standard deviation of the meridional wind, substantial differences between the models arises. The smallest  $\sigma$  is presented by the LR model ( $\approx 0.2\text{m/s}$ ) and largest in MR ( $\approx 0.8\text{m/s}$ ). The different standard deviations also can depict the different variability with corresponding varying wave forcing. Wave types assumed to be responsible for driving the easterly phase of the SAO are planetary Rossby waves and westward propagating inertio-gravity waves (IG). The westward IG waves in particular, are not explicitly discussed in the previous QBO section (see Sec. 4.1.3), because their contribution to the driving mechanism of the QBO is negligible (Kawatani et al., 2010b). However concerning the SAO the IG waves play a substantial role in providing the necessary momentum, especially IG waves of approximately a diurnal period contribute most of the forcing for the easterly phase of the SAO (Sassi and Garcia, 1997; Garcia, 2000). The relative power of ERA-Interim given at 30 hPa (Fig. 4.4(a)) offers a very distinct signal in the power spectra appearing at small westward wavenumbers with periods of approximately a day (larger 0.6 cpd). Analogous to the work of Wheeler and Kiladis (1999) this distribution of power can be attributed to the variability of IG waves. Examination the corresponding PSA pattern of the models, it is apparent that they all together considerably under estimate the IG waves. This implies that in the models a substantial fraction of momentum accounting for the westward acceleration is missing, which in turn would be

relevant to force the easterly phase of the SAO. Relating to the REF and MR simulation this dynamical drawback is a strong indication why westward propagating winds in the SAO are underrepresented.

Not only IG waves provide momentum for the generation of equatorial easterlies, extra-tropical planetary waves can also directly contribute to the easterly phase of the SAO (Garcia, 2000; Holton and Wehrbein, 1980; Dickinson, 1968). Hendon et al. (2007) also verify that extra-tropical planetary waves emerge in the symmetric component of equatorial PSA. They were able to attribute the power of these planetary waves to the Rossby-Haurwitz (RH) waves.

Fig. 4.8 shows the relative power distribution of the symmetric component identical to Fig. 4.4 presented before in Sec. 4.1.2, but now the dispersion curves of RH waves with  $n = 1$  and  $n = 3$  are included. The dispersion curves were calculated following the discussion in Hendon et al. (2007). Although the RH waves are external non-equatorial trapped waves, they can be approximated by ER waves with an equivalent depth of 10 km and assuming a constant westerly advecting velocity of 15 m/s, which depicts a mid-latitude equivalent barotropic level (Hendon et al., 2007; Kasahara, 1980).

By means of these additional dispersion curves, it is clearly evident that the model with higher vertical resolution can reproduce quite well the power of planetary RH waves but the LR model substantially overestimates their contribution. Considering the log scale in the representation of relative power, the signature of the RH waves derived from the LR model is approximately one order of magnitude larger compared with the reanalysis.

So the strongly even and regular oscillation pattern of the SAO in the LR configuration could result from a combination of enhanced planetary RH waves and overestimated meridional wind at the equator. Especially it is discussed that a strong meridional wind in the middle atmosphere could intensify the advection of easterly momentum provided by planetary waves (Andrews et al., 1987; Holton and Wehrbein, 1980), which could explain the strong easterly phase of the SAO in the LR model.

#### 4.1.6 Summary and Discussion of Tropical Variability

Deviations from the reanalysis data referring to the QBO signal of intra-decadal power spectra derived from model simulations give rise to a more detailed inspection of the tropical variability. The leading variability patterns of tropical middle atmosphere are the QBO and the SAO. In particular their underlying dynamical drivers are analysed in order to gain some explanations for the different behaviours detected in the numerical simulations.

At first it is demonstrated that only models with a higher vertical resolution (REF and MR) are capable to produce an alternating easterly and westerly wind regime in the tropical stratosphere, which is a characteristic feature of the QBO. In the simulation with lower vertical resolution (LR), the wind regime is dominated by weak easterlies. However, also weaknesses in REF and MR arise in the representation of the QBO compared to ERA-Interim, in particular in MR the wind amplitudes are overestimated and the duration and downward propagation of the individual QBO phases are more irregular compared to reanalysis data.

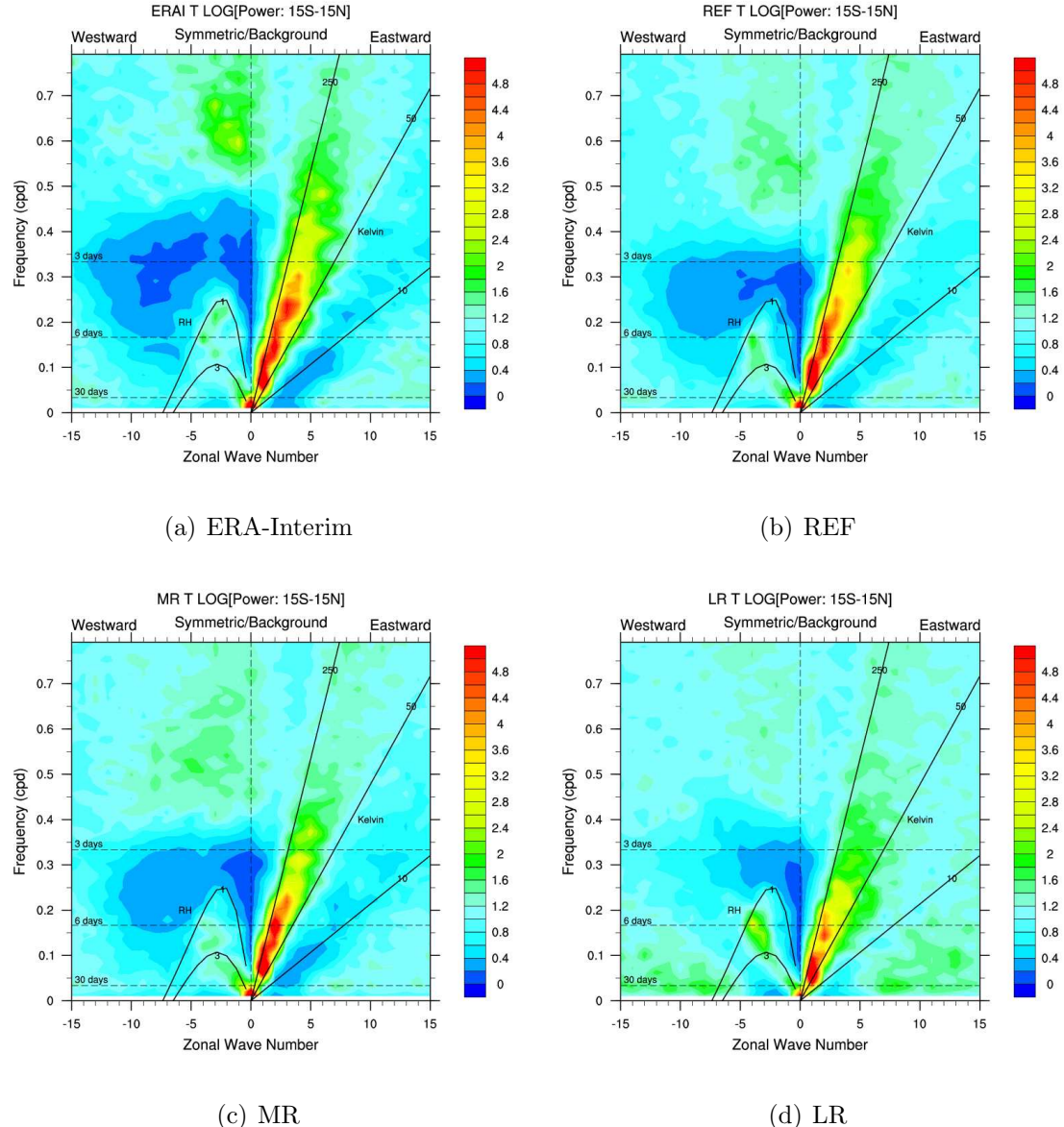


Abbildung 4.8: Same as Fig. 4.4, but additionally dispersions curves of Rossby-Haurwitz waves with  $n = 1$  and  $n = 3$  included. See text for more details.

To analyse the underlying processes, intra-seasonal PSA following the work of Wheeler and Kiladis (1999) is enabled, which gives a very detailed picture of the contribution of the different wave types. It is generally accepted that Kelvin and MRG waves provide the necessary momentum to force the QBO (e.g. Dunkerton, 1997; Ern and Preusse, 2009; Kawatani et al., 2010a). Both wave types clearly arise in the power spectra derived from the model simulations. However, differences towards ERA-Interim can be detected in the distributions and amplitudes of the individual variability patterns, e.g. variability in the MR simulation derived for MRG waves is considerably overestimated (within periods between roughly 3 and 6 days) compared to the reanalysis data. Thus these deviations can lead to a different wave forcing which in turn could contribute to the detected, irregular QBO periods.

In the LR model, variability of Kelvin and MRG waves are smaller than in ERA-Interim, in particular the contributions of the relevant power of MRG waves are widely half as large as in the reanalysis data. This underestimation of power is very likely the reason that there is no alteration of westerlies and easterlies in the QBO region of the LR model. By a combination of linear wave theory and the PSA following Wheeler and Kiladis (1999) derived from ERA-Interim, it was demonstrated that it is mandatory to resolve MRG waves with vertical wavelenghts of 2 km in order to capture the momentum which is required to force the QBO. Therefore, numerical models need to have a vertical resolution of at least 1 km in order to resolve these waves. This is in accordance to the study of Giorgetta et al. (2006), who determined with an experimental approach that for the generation of the QBO a minimum vertical resolution of approximately 1 km is necessary. However, the vertical resolution of LR model setup is on average 2 km and thus a considerable fraction of the wave spectra cannot be captured which lead to the detected underestimation of variability in the PSA of MRG waves. Apart from the QBO, the SAO is a further leading variability pattern of tropical middle atmosphere. The SAO forms from mesospheric to upper stratospheric levels. A distinct interaction between the QBO and the above located SAO is widely discussed in several studies (e.g. Dunkerton and Delisi, 1997; Mayr et al., 2010; Garcia et al., 1997; Sassi and Garcia, 1997). Since the here regarded numerical models have vertical extents covering lower mesospheric altitudes the SAO analysis were also taken into consideration.

Generally speaking all models are capable of producing a SAO like oscillation. Comparing the models with higher vertical resolution (REF and MR), the deviation of the SAO pattern compared to reanalysis data are larger in the MR model. The MR is also the model system which shows larger differences in the QBO pattern. Bearing in mind the strong relationship between QBO and SAO this finding is quite reasonable.

In the LR model no QBO signal could be detected, but in the upper stratospheric lower mesospheric levels a comparatively strong SAO pattern arises. This could be explained by the fact that driving mechanism of the QBO and SAO differs from each other. Especially the momentum for westward acceleration of the SAO is believed to be provided by planetary waves. Analysis of PSA in the LR model show that these waves are particularly overestimated.

Overall numerical model simulations have to consider an adequate high vertical reso-

lution in order to give a reasonable representation of the leading variability pattern of tropical middle atmosphere.

## 4.2 Antarctic Polar Vortex Variability

Large differences of decadal variability between models and reanalysis data arise in the polar stratospheric regions. But in EMAC deviations are most evident in the Southern hemisphere as shown in Chapter 3. The main contributions to this over represented variability are very likely caused by a too weak Southern hemispheric polar night jet, which in turn is related to overestimated wave activity (Deckert, 2012). Further model deficits of the Southern hemispheric polar vortex in EMAC are described in several publications (e.g. Khosrawi et al., 2009; CCMVal, 2010; Righi et al., 2014), however, the underlying processes are very little investigated and remain unclear. The model deviations in the Arctic region of EMAC are predominantly not statistically significant (e.g. Righi et al., 2014). Therefore, the focal points of this section are on the Southern hemisphere, presenting a systematic research into the causes and the potential drivers of the shortcomings of the representation of the Austral polar vortex in the EMAC model system.

### 4.2.1 REF Climatologies

The Fig. 4.9 shows the latitude-height cross sections of the 10 year climatological mean of the seasonal mean anomalies of zonal mean temperature and zonal mean wind field respectively. Anomalies in this case refer to differences of the REF simulation to ERA-Interim.

Regardless of the season a cold bias can be detected in all latitudes around the tropopause level at roughly 100 hPa. In the polar region in particular during Boreal summer season (JJA) this bias is comparatively strong and can exceed values of -10 K. However, it should be noted that this characteristic model bias is a common feature of CCMs (IPCC, 2007; CCMVal, 2010). The underlying processes leading to this cold bias are still yet not completely understood and possibly can differ among different models (e.g., Pawson et al., 2000). For instance, Stenke et al. (2008) showed that the polar cold bias in ECHAM4 is partly attributed to a considerably overestimated water vapour concentration in the extratropical lower and middle stratosphere. Furthermore Righi et al. (2014) demonstrate that in EMAC globally the temperature cold bias at tropopause and lower stratospheric levels are owed to an overestimated water vapour concentration. Water vapour is a radiatively active trace gas. The long wave outgoing radiation by water vapour at stratospheric levels is larger than the absorptions of upwelling infrared radiation from the troposphere. Therefore water vapour here leads to a net cooling effect.

Apart from this cold bias and comparing all seasons, the Southern hemispheric polar jet shows striking differences. Considerably in Austral winter (JJA) and spring (SON) stratospheric winds around 60°S in the REF simulation can be more than 20 m/s weaker than in the reanalysis data, which corresponds very roughly to a 20-30 % wind bias. The dipole

anomaly pattern in JJA, meaning strong negative wind biases at latitudes equatorward of 60°S and strong positive wind bias at latitudes higher than 60°S, indicates that the core of the simulated polar night jet is shifted poleward compared to the reanalysis data, which could be driven by spurious atmospheric wave activity in the numerical simulations. In SON the modelled Southern hemispheric vortex is overall weaker. Due to the strong correlation of wind and temperature (e.g. via the thermal wind relationship), these deviations of the zonal wind are also reflected in the temperature fields. Thus, in JJA a remarkable warm bias up to 8 K can be detected along the core of the polar night jet. During Austral spring (SON) the warm bias focuses at high-latitudes in the lower stratosphere and upper troposphere with maximum values of approximately 10 K.

At higher altitudes in the stratopause level at roughly 1 hPa, anomalies can reach values up to 12 K in the corresponding autumn and winter hemisphere. Anomalies above 0.5 hPa are not taken into consideration, since the underlying numerical model of ERA-Interim has a model lid at 0.1 hPa and values derived in the vicinity of the model top are highly influenced by the upper boundary conditions and often have no physical base.

In the Northern hemisphere the stratospheric model biases are smaller compared to the Southern hemisphere ones, in particular when Boreal seasons are compared with Austral seasons. The differently large inter-hemispheric model biases could be owed to the fact that inter-annual variability of the Northern hemisphere is significantly larger then in the Southern hemisphere (Holton et al., 2003) and thus model weaknesses of the Northern hemisphere are masked.

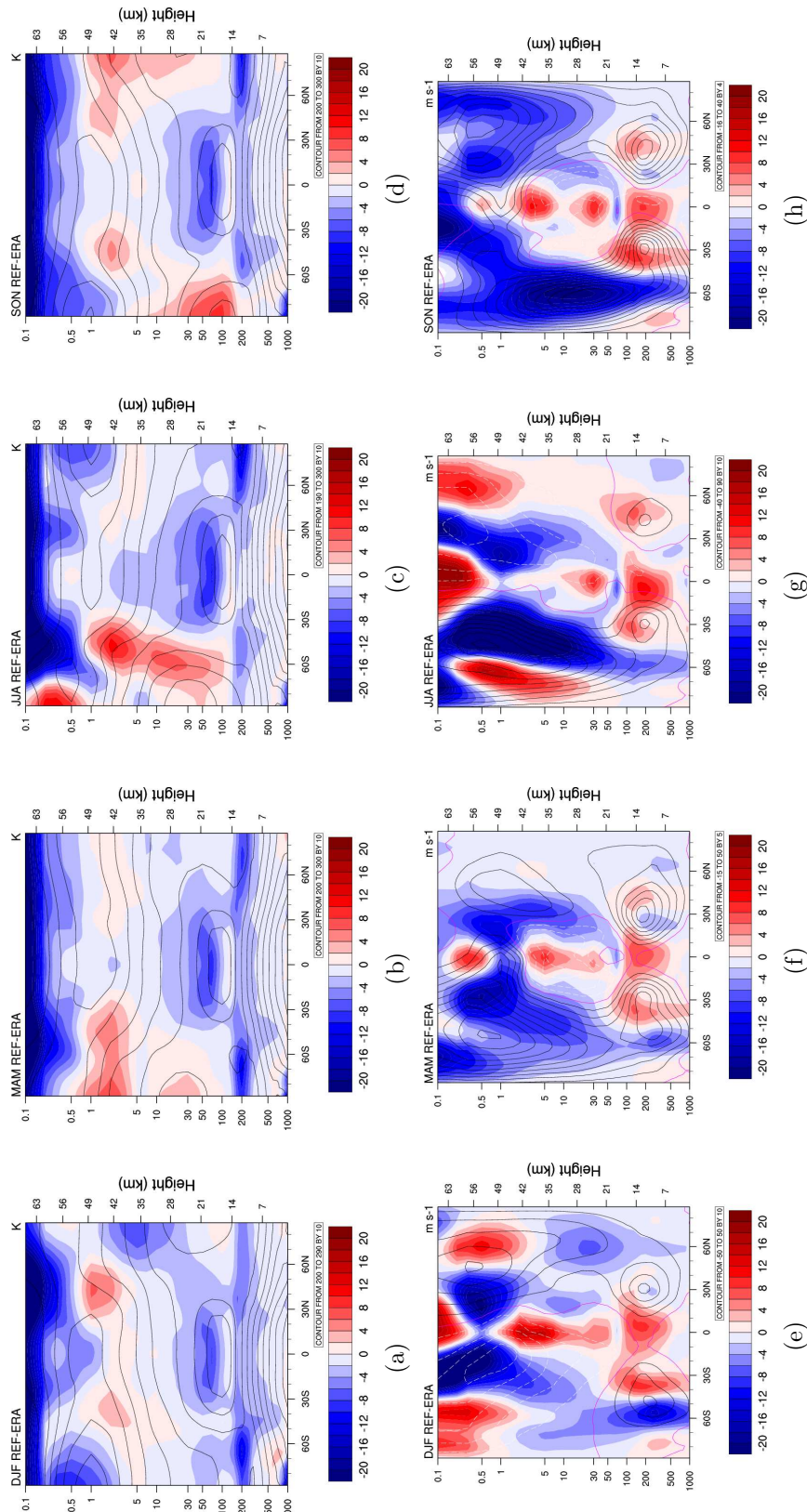


Abbildung 4.9: Latitude-height cross section of seasonal mean anomaly of REF minus ERA-Interim for a)-d) zonal mean temperature given in K and e)-h) zonal mean wind given in m/s. Black contour lines refer to ERA-Interim absolute values.

### 4.2.2 Sea Surface Temperature (SST) Sensitivities

Deckert (2012) presumed that planetary waves play a decisive role in the problem of representing the polar vortex. He demonstrated that enhanced planetary wave activity in EMAC during the Austral winter season, leading to enhanced wave dissipation in the lower stratosphere and eventually resulting into a weaker polar vortex.

Sea surface temperatures (SSTs) are known to influence planetary wave activity (e.g. Andrews and McIntyre, 1976; Holton and Hakim, 2013; Garny, 2010; Cai et al., 2012). In order to investigate the underlying mechanisms of Deckert (2012) hypotheses more closely, two sensitivity studies HAD and MPIOM, with different prescribed SSTs are carried out. The REF and HAD simulations utilise respectively their own SST data sets but both SST data sets are based on observations whereas in the MPIOM sensitivity study the SSTs are derived from a numerical model simulation. For technical details and simulation setups see Sec. 2.2.3.

#### SSTs

A first impression of the differences between the individual SST data sets is given in Fig. 4.10. In Fig. 4.10(a) the climatological annual mean SST for AMIP is presented. The AMIP data set is used to prescribe the SSTs and sea-ice cover in the reference time-slice simulation REF. Deviations between the observational based SSTs namely AMIP and HadISST are in general small (see Fig. 4.10(b)), but comparatively large differences up to 1.8 K can be found in the Southern mid-latitudes in the vicinity of 60°S. During SON these differences even exceed 2.4 K (not shown). Due to sparse observational data in the polar regions, especially in the Southern Ocean the data sets are challenged by relatively large uncertainties. For example, in the HadISST a specific interpolation procedure is applied in order to fill the 'gaps' in the data (Rayner et al., 2003). Therefore, it is not surprising that the major differences between AMIP and HadISST occur in the Southern Ocean.

When comparing the SSTs derived by model simulation based on MPIOM with AMIP observations (see Fig. 4.10(c)), a model cold bias of less than 5 K primarily arises along the continental east coasts. Warm biases can be found in the tropical region and particularly in the North-Atlantic ocean with values exceeding 7 K which corresponds to a relative difference of  $\sim 6\%$ . In the Southern hemisphere the anomaly pattern resembles a wavenumber 1 pattern with amplitudes of approximately 2-3 K (see Fig. 4.10(d)). But in general, model deviations can be four times larger compared to the deviations between the observational data sets. Further details and evaluations of the simulations of the underlying ocean model can be found in Kern (2013) and Jungclaus et al. (2013).

Nonetheless the differences identified here between the individual SST data sets, especially in the middle latitudes of the Southern hemisphere have a great potential to affect activity of planetary waves, i.e. the latitudinal region of 60°S are also expected to accommodate the majority of Southern hemispheric wave activity (Holton and Hakim, 2013; Newman et al., 2001). Furthermore, due to interactions of planetary waves with the background mean flow, deviations in the planetary wave activity could considerably contribute

to the properties, such as strength and variability of the simulated polar vortex.

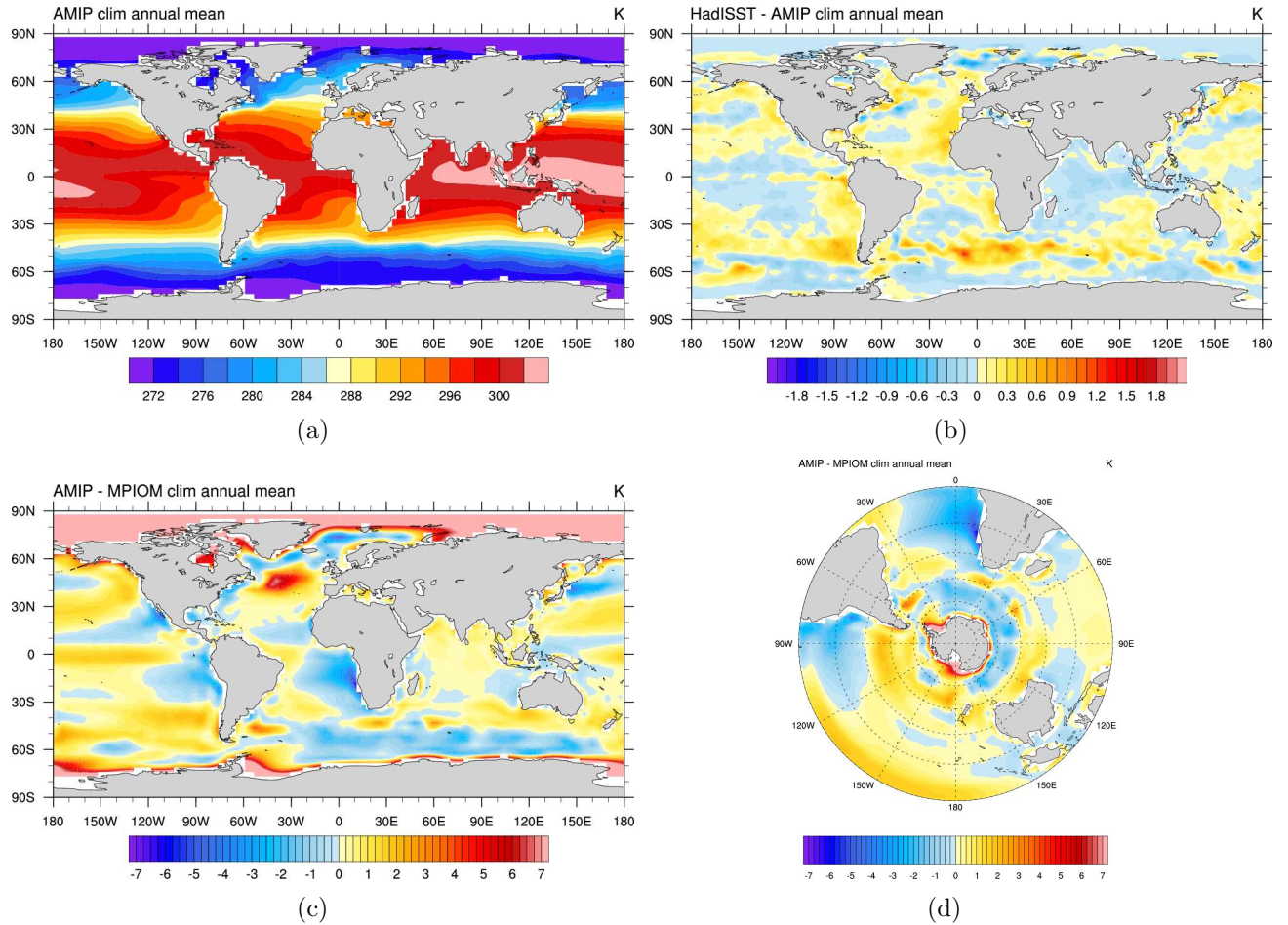


Abbildung 4.10: Climatological annual mean SSTs given in K. a) AMIP, b) differences of HadISST and AMIP and c) differences of AMIP and MPIOM. d) Southern hemispheric polar stereographic projection of c) – note b) and c) have different colour tables.

### Annual Cycle of Polar Temperature

The mean temperature of the stratospheric polar cap ( $90^{\circ}\text{S}$  -  $60^{\circ}\text{S}$ ) can be considered as a proxy for the strength of the Southern hemispheric polar vortex. The climatological mean annual cycle of the height cross section of polar cap temperature of ERA-Interim is given in Fig. 4.11(a). The temporal evolution of the polar vortex can now be easily captured. With sunset and the onset of winter polar temperature decreases rapidly and the polar vortex strengthens. The most stable conditions for the polar vortex is accompanied by the lowest temperature of approximately 180-190 K, which can be found at stratospheric and upper tropospheric levels (10 hPa-100 hPa) from June to September. The relatively warm

stratopause is situated aloft at around 1 hPa. During winter terms the stratopause altitude is higher than in summer.

All simulations show a comparable deviation pattern from ERA-Interim in the seasonal cycle of polar cap temperature (see Figures 4.11(b)-(d)). A characteristic warm bias in the stratopause altitude at about 1 hPa, which evolves during the Austral autumn season (MAM) and lasts until spring season (SON). But also in the entire vertical extent of the stratosphere a warm bias in all model configurations can be seen. It begins with March and intensifies within the transition from winter to spring season, reaching maximum values from 6-8 K. During spring (SON) the modelled temperature bias seem to propagate from upper stratospheric level down to lower stratospheric levels.

The sensitivity simulation with prescribed modelled SSTs (Fig. 4.11(d)) presents the smallest warm bias. The stratospheric temperature difference here never exceeded 6 K and also the vertical extent of the warm bias during winter to spring transition is the smallest compared to the REF (Fig. 4.11(b)) and HAD (Fig. 4.11(c)) simulations. Both models configurations enable observational based SSTs.

Deviations from modelled to observational based Antarctic temperature fields could originate from planetary wave activity. This is the case in particular, if account is taken of the facts that firstly, the stratospheric warm bias preferably appears from late autumn to early spring term during the westerly phase, when atmospheric conditions are conducive for vertical propagating planetary waves and secondly, the individual SST data sets differ in the region of the Southern hemispheric mid-latitudes where planetary wave activity is expected to be large. So analyses of planetary waves are needed in order to consider the problem of the too warm and therefore too weak polar vortex.

### Meridional Eddy Heat Flux

In the following, planetary wave activity is analysed by means of the meridional eddy heat flux ( $\overline{v'T'}$ ). The mid-latitudinal zonal mean of meridional eddy heat flux at 100 hPa was used in Austin et al. (2003) as a diagnostic tool for planetary waves entering the lower stratosphere originating from the troposphere. This diagnostics based on the study of Newman et al. (2001), who demonstrated that the mid-latitudinal, upper tropospheric  $\overline{v'T'}$  (at 100 hPa height level) and the polar temperatures of the lower stratosphere (at 50 hPa height level) are linearly correlated suggesting an underlying mechanism driven by planetary wave activity.

The Figures 4.12(a) to (c) show the seasonal development of  $\overline{v'T'}$  at 100 hPa averaged over a broad latitudinal band from 40°S - 80°S, which is analogous to the analysis described in Newman et al. (2001). However, additionally the relative contribution of the first three harmonics (wavenumber 1 – 3) are presented. This is achieved by an a priori Fourier decomposition of the input fields temperature and meridional wind speed, before the heat flux is calculated. In this work  $\overline{v'T'}$  for the Southern hemisphere is defined as negative, thus small numerical values represent large fluxes and large numerical values represents small fluxes respectively. The meridional eddy heat flux given here are monthly means derived from daily values. The analysis and definition of planetary waves are not strictly

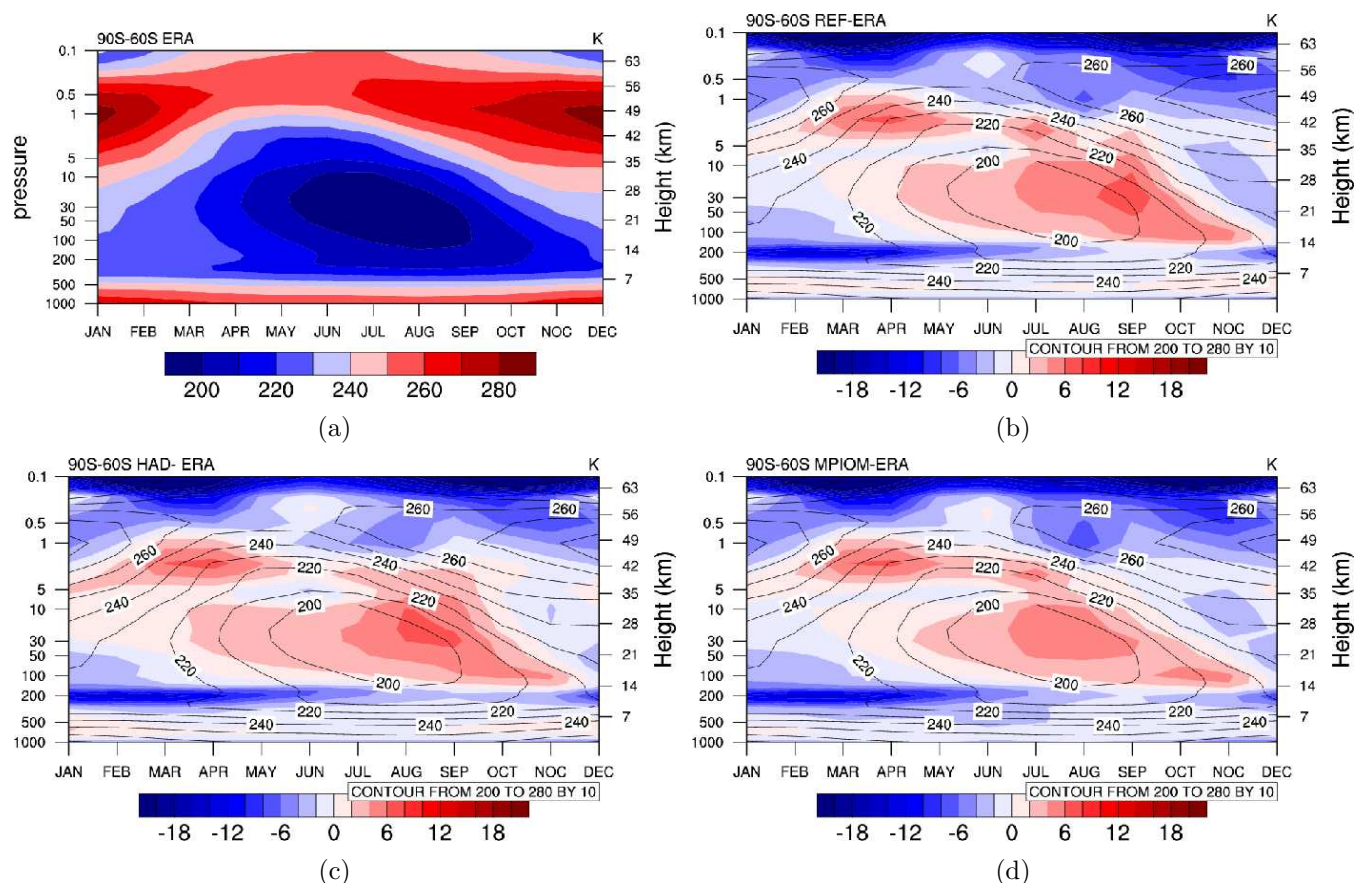


Abbildung 4.11: Annual cycle climatology of 90° S - 60° S mean temperature given in K of a)ERA-Interim and corresponding temperature anomaly for b)REF, c)HAD and d)MPIOM. Solid contour lines refer to the values of ERA-Interim.

determined in literature, e.g. Newman et al. (2001) considered  $\overline{v'T'}$  derived from daily full field atmosphere as planetary waves, whereas Holton and Hakim (2013) regarded the first 3 harmonics of the atmospheric field as planetary waves. Thus, the analysis in this work is a hybrid of both approaches.

An advantage of this analysis is for example, that now on the basis of the Fourier decomposition it is clearly apparent that planetary wavenumber 1 is the dominating compound of  $\overline{v'T'}$ . For ERA-Interim the annual cycle of the wavenumber 1 heat flux is characterised by low values in the Austral summer and autumn and high values during winter and spring (see Fig. 4.12(a)). From December to March low meridional heat fluxes of  $-1$  to  $-2 \text{ Kms}^{-1}$  can be found. Beginning with July a strong increase of  $\overline{v'T'}$  can be seen. This rise of planetary wave activity peaks in October with heat fluxes of approximately  $-8 \text{ Kms}^{-1}$ . After October in the course of November heat fluxes strongly decrease and eventually reach low December levels.

Regarding the corresponding annual cycle of  $\overline{v'T'}$  derived from the individual model simulations, considerable deviations from ERA-Interim can be noted. For example, in the REF simulation the shape of the annual course of the eddy heat flux is flatter and shifted by one month ahead, meaning the maximum is situated in September with values of approximately  $-6 \text{ Kms}^{-1}$ . The winter months show an overestimation of  $\overline{v'T'}$  whereas the heat fluxes are underestimated during spring terms compared to the reanalysis data. In the HAD simulation the annual cycle is qualitatively well represented during DJF and MAM, but during winter and the transition from winter to spring, in particular in August and September the values of  $\overline{v'T'}$  derived by the model exceed reanalysis data by roughly  $3 \text{ Kms}^{-1}$ , which corresponds to a 60-80% deviation relative to the reanalysis data. Regarding the MPIOM sensitivity simulation the annual evolution of the eddy heat flux is reflected quite well, apart from JJA season. Especially during July the  $\overline{v'T'}$  is  $-5 \text{ Kms}^{-1}$ , which is more than twice as high as in ERA-Interim.

Morphologically all models overestimate the eddy heat flux during late autumn to winter, but during spring from September to November is not as clear. For example in the REF simulation the heat fluxes during spring are distinctly underestimated, whereas in the HAD and MPIOM configurations during October and November  $\overline{v'T'}$  is qualitatively good captured. Furthermore, differences arises in September, when in particular the HAD simulation shows a strong over representation of the heat flux compared to ERA-Interim by roughly  $3.5 \text{ Kms}^{-1}$ .

### 4.2.3 Discussion of SST Sensitivities

The SST sensitivity studies are carried out in order to investigate the implications of different SST data sets on the model dynamics. The main focus is the Southern hemispheric polar region, since intra-decadal power spectra are determined by overestimated variability in particularly the Antarctic stratospheric region and moreover previous studies have demonstrated model deficits of ECHAM5 in the representation of the Southern hemispheric polar vortex (Deckert, 2012; Khosrawi et al., 2009). The utilised SST data sets originate from observations (AMIP and HadISST) and a numerical simulation based on

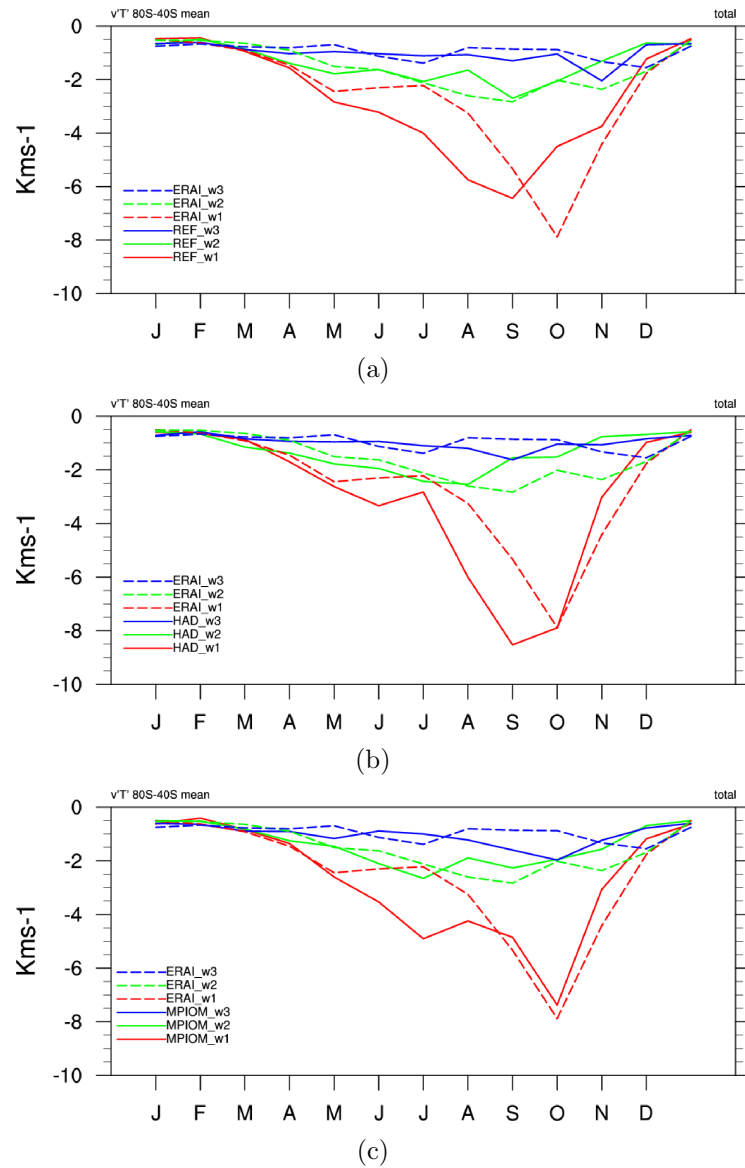


Abbildung 4.12: Annual cycle climatology of  $40^{\circ}\text{S} - 80^{\circ}\text{S}$   $\bar{v}'T'$  at 100 hPa given in  $\text{Kms}^{-1}$  for a)REF, b)HAD and c)MPIOM. Solid lines refer to the corresponding simulation and the dashed line to ERA-Interim, respectively.

an atmosphere-ocean model. The deviations between observational SSTs are on average generally small (less than 1%) and are four times lower compared to differences between observational and modelled SSTs. However, in the Southern ocean larger differences in the observational SSTs can be found. Concerning planetary wave activity, the deviations detected in the Southern ocean, may probably have implications on the generation of planetary waves and thus, planetary wave activity, e.g. Cai et al. (2012) showed that SST anomalies in the Arctic Ocean have significant effects on the planetary waves during late Boreal autumn.

The analysis of the seasonal evolution of Southern hemispheric polar cap temperature ( $90^{\circ}\text{S}$  -  $60^{\circ}\text{S}$ ) shows for all three simulations a comparable anomaly pattern with regard to ERA-Interim. From late Austral spring to autumn a stratospheric warm bias occurs with maximum 8 K difference during late winter early spring. However MPIOM, the simulation with prescribed modelled SSTs, presents the smallest bias. Bearing in mind that westerly conditions are conducive for planetary waves (e.g. Holton and Hakim, 2013), this simulated stratospheric warm bias could result from enhanced activity of planetary waves. Enhanced planetary wave activity can provide momentum, which in turn could decelerate the background mean flow leading to a warmer polar vortex (Andrews and McIntyre, 1976).

To answer the question whether planetary waves play a role for this warm bias, the meridional eddy heat flux ( $\overline{v'T'}$ ) of Southern hemispheric middle latitudes at 100 hPa is investigated. The eddy heat flux is a measure for tropospheric planetary waves entering the lower stratosphere (Austin et al., 2003). By means of a Fourier decomposition it is demonstrated that planetary wavenumber 1 is the largest contributor. The seasonal distribution of  $\overline{v'T'}$  derived from the individual model setups evince qualitative and quantitative differences. However, all simulations have in common that the eddy heat flux is overestimated compared to ERA-Interim during Austral autumn and winter months. Considering the findings of Newman et al. (2001) an enhanced  $\overline{v'T'}$  would lead to an increased lower stratospheric polar temperature with a time lag of about one month. So the Antarctic model warm bias during winter can probably partly be attributed to the detected stronger planetary wave activity, in particular by the contribution of wavenumber 1, but the model temperature deviations from ERA-Interim in the course of the spring term seem no longer to be explained by the Newman-correlation, i.e. all simulations show consistently a warm bias during SON, but the corresponding heat fluxes of the preceding months derived by individual simulations cannot provide such a clear behaviour. Therefore, in the spring months SON, planetary waves (in particular the contribution of wavenumber 1) very likely play a minor part contributing to the polar vortex properties of the model.

Furthermore, the work of Austin et al. (2003) demonstrated that the relation of temperature and heat flux during Austral winter and spring is quite differently represented by different climate models (see Fig. 4.13). They did not provide a clear explanation for the underlying processes. However, in the presentation of Shepherd (2006) referring to the findings in Austin et al. (2003), it was suggested that the various treatment of the gravity waves among the models could lead to the deviation in their corresponding correlation of temperature and eddy heat flux. According to Shepherd's line of arguments  $\overline{v'T'}$  at 100

hPa is considered as the amount of planetary wave activity, which is resolved by the models entering the stratosphere. The polar temperature occurring at 50 hPa is a result of the interaction of the background mean flow with the total wave activity. In this case total wave activity denotes the combination of resolved planetary wave activity and parameterised gravity wave activity. Thus, Shepherd (2006) concluded that differences in the correlation of  $\overline{v'T'}$  and temperature derived by the individual models, are associated with different approaches of handling gravity waves.

Analogous analyses to Austin et al. (2003) are carried out with the REF simulation and ERA-Interim and the results for the Southern hemispheric winter to spring season is discussed in the following (see Fig. 4.13). Firstly, it has to be noted that  $\overline{v'T'}$  in Austin et al. (2003) is defined in an opposite direction to this work, therefore only the absolute values of the eddy heat flux are regarded. A comparison is undertaken of the reanalysis data sets ERA-Interim and NCEP/NCAR. Differences occur in the slope of the regression lines. In NCEP/NCAR the slope is about 0.89 whereas in ERA-Interim the calculated slope is 0.73. This deviation is relatively small towards the range from 0.45 to 1.14, which arises from analysis of the presented models in Austin et al. (2003). The slope derived by the correlation line in REF is 1.04, which is steeper than in both here regarded reanalysis data sets. The corresponding value for HAD is 2.20 and for MPIOM is 1.86, respectively. Thus, all models show a stronger stratospheric temperature response to resolved planetary wave activity with regard to ERA-Interim. Following Shepherd (2006) this additional temperature response could be forced by parameterised, unresolved gravity waves. Yet it has to be called to attention that the correlation lines derived from the model are based only on 10 years, and for statistical significance more years have to be taken into account. But still these preliminary results give rise to indications that parameterised gravity waves could add a considerable amount to the detected warm bias.

#### 4.2.4 Gravity Wave Sensitivity

It is well established that gravity waves play an important role in determining the structure and variability of middle atmosphere (Fritts and Alexander, 2003). As demonstrated in previous Chapter gravity waves provide the required momentum to force the QBO and SAO, which are the characteristic features in the tropical middle atmosphere. For the extra-tropical region, in particular the wintertime Southern hemispheric stratospheric polar vortex, models which do not consider the representation of gravity waves suffer from the so-called cold pole bias, a substantial negative temperature bias in the Antarctic stratospheric region (Garcia and Boville, 1994). However, in EMAC the analyses of Southern hemispheric stratospheric polar temperature shows a severe warm bias. Determined from Newman-correlations in the previously presented SST sensitivity simulations (see Sec. 4.2.2), an enhanced gravity wave activity may explain this bias. Therefore, gravity wave sensitivity simulations are carried out, with gradually changed  $rmscon$  value which is a tuning parameter of the non-orographic gravity wave scheme in the submodel GWAVE (description see Sec. 2.2.3). The  $rmscon$  parameter is set in the individual simulations as follows, in G1  $rmscon = 0.88$ , in G2  $rmscon = 0.94$ , in G3  $rmscon = 1.00$  and in G4

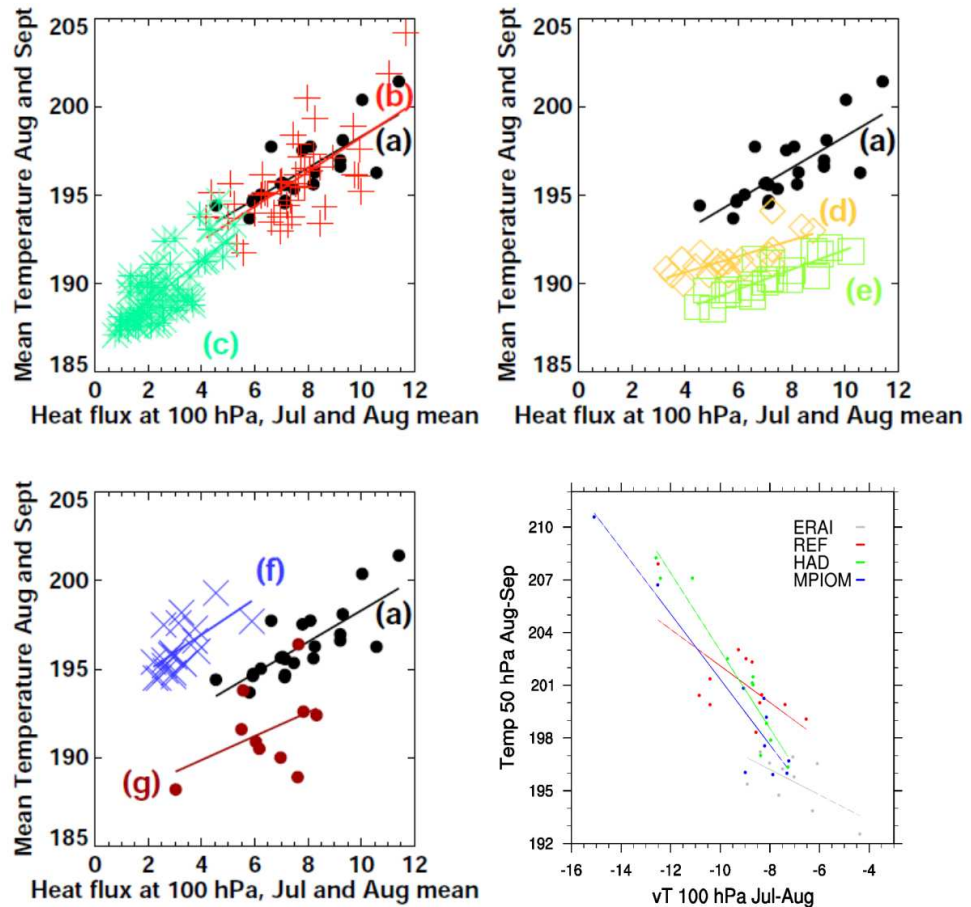


Abbildung 4.13: Correlation of  $\overline{v'T'}$  at 100 hPa given in  $\text{Kms}^{-1}$  averaged over  $80^\circ\text{S} - 40^\circ\text{S}$  and July to August, and polar temperature given as  $K$  for the  $90^\circ\text{S} - 60^\circ\text{S}$  mean at 50 hPa for August to September. Upper and lower-left plots are from Austin et al. (2003). a) NCEP/NCAR reanalysis, b)- g) different CCMs, details see in reference. Lower-right plot corresponding correlation for ERA-Interim, REF, HAD , MPIOM – note  $\overline{v'T'}$  here is defined as negative in opposite to a)-g).

$rmscon = 1.04$ . In the G5 simulation the gravity wave parameterisation of non-orographic gravity waves is disabled. For the REF simulation  $rmscon = 0.96$  is applied. More details of the respective simulation setup can be read in Sec. 2.2.3.

### Annual Mean Gravity Wave Flux and Wave Drag

Implications of the choice of different  $rmscon$  parameter on the gravity wave flux and the corresponding wave drag at stratospheric level are illustrated in Fig. 4.14. The 10 hPa level is selected in order to represent a typical middle stratospheric level. The findings presented in the following are insensitive to the selected 10 hPa level and are qualitatively applicable to a wide vertical range of the stratosphere.

The latitudinal distribution evince a clear preference for the high-latitudes for the absolute values of annual mean gravity wave flux as well as for the wave drag. The gravity waves fluxes are characterised by a maximum peak centred roughly around the  $60^\circ$  latitude, whereas the wave drag shows a broader distribution with several local maxima. The maximum Southern hemispheric quantities compared to the Northern hemispheric ones can be more than twice as large.

Differences also arise among the individual simulations. Maximum annual mean gravity wave flux in the Southern hemisphere for G4 is approximately  $14 \text{ mPa}$  and for G1 it is  $0.9 \text{ mPa}$  and respectively for the wave drag G4 has  $16 \times 10^{-4} \text{ mms}^{-2}$  and in G1 the wave drag is  $7 \times 10^{-4} \text{ mms}^{-2}$ . In principle, with an increasing  $rmscon$  parameter both the gravity waves flux and wave drag at 10 hPa intensify. The  $rmscon$  parameter in REF is set between the values of G2 and G3 simulations. Accordingly, the gravity wave flux and wave drag is located between the quantities of G2 and G3. In principle, the here described differences of gravity wave activity presumably have a different effect on the extra-tropical dynamics and hence implication on the Southern hemispheric polar vortex.

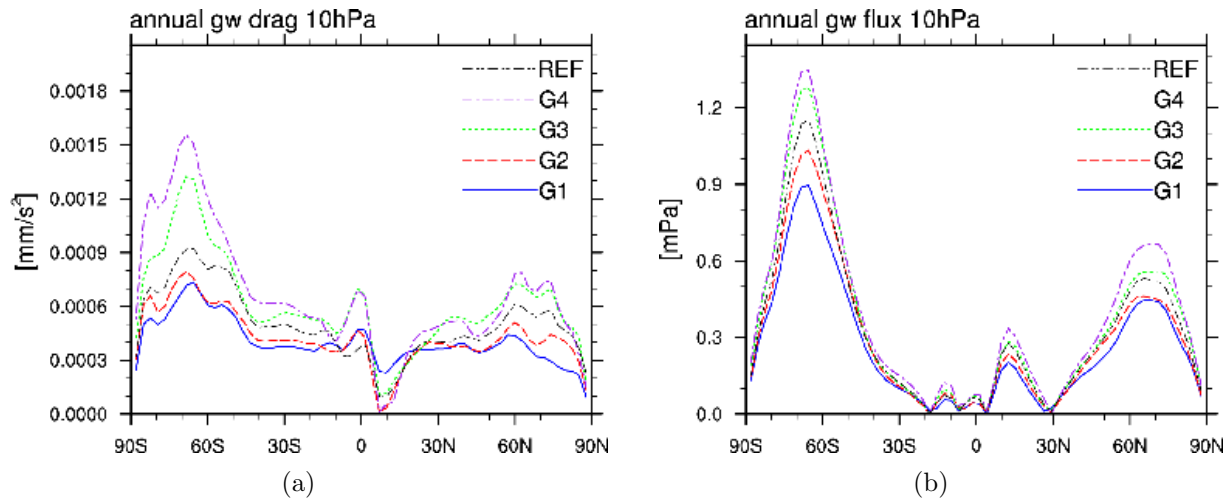


Abbildung 4.14: Absolute values of annual mean of a) gravity wave drag given in  $\text{mms}^{-2}$  and b) gravity wave flux given in  $\text{mPa}$ , respectively at 10 hPa.

### Annual Cycle of Polar Temperature

To analyse the temporal evolution of the Southern hemispheric polar vortex, the annual cycle of mean Antarctic polar cap temperature anomalies of the individual simulations are presented in Fig. 4.15. Anomalies refer to model deviation from ERA-Interim.

In contrast to the previously shown SST sensitivities, the anomaly patterns of the gravity wave sensitivity simulations differ distinctly from each other. In the simulations with a smaller  $rmscon$  parameter, namely G1 (Fig. 4.15(b)) and G2 (Fig. 4.15(c)) the stratospheric warm bias during Austral winter and spring season is less pronounced compared to the REF (Fig. 4.11(b)) simulation. Deviations from ERA-Interim are smaller than 4 K and never exceed 8 K. The warm bias in G1 tends to be bounded to the lower stratospheric levels around 50 hPa to 30 hPa. However, in the case of G2 positive anomalies can reach stratopause levels in late winter to early spring term. For the stratopause level the simulated warm biases of G1 and G2 are less than in REF or even negative anomalies can arises (e.g. in June at 5 hPa in Fig. 4.15(b), 4.15(c)). With a larger  $rmscon$  parameter, in particular in the sensitivity run G3 (Fig. 4.15(e)) and G4 (Fig. 4.15(f)) the model warm bias is increased towards the REF simulation. For both of these sensitivity simulations the stratospheric warm bias amplifies in the course of the winter months reaching a relative maximum in the transition from winter to spring with values of about 10 K. In the spring terms anomalies propagate from upper stratospheric levels at 1 hPa to tropopause level at 100 hPa. The overall absolute maximum positive anomaly in both sensitivity simulations can reach 12 K. Analogous to the REF simulation a continuous stratopause warm bias can be found roughly from March to September.

With regard to G5 (Fig. 4.15(a)), the simulation without non-orographic gravity wave parametrisation, a so called cold-pole bias can be observed. Negative anomalies, which can drop below -18 K, occur during March to September and vertically extend through the whole middle atmosphere.

Broadly speaking simulations taking the effects of non-orographic gravity waves into account, suffer all together from a stratospheric warm bias in the Austral winter and spring season. Furthermore, it should be noted that with an increased  $rmscon$  parameter this model warm bias intensifies. As shown earlier, raising the  $rmscon$  parameter enhances at the same time the gravity wave dissipation, reflected in the gravity wave drag in Fig. 4.14(a) at stratospheric levels.

### Meridional Eddy Heat Flux

On the basis of reduced wavenumber model experiments previous studies (Holton, 1984; McLandress and McFarlane, 1993) suggested a potential significant interaction between unresolved parameterised wave drag and the resolved wave driving in the middle atmosphere. This relationship possibly could contribute to a better understanding of the model temperature bias derived by the gravity wave sensitivity simulation set. Therefore, resolved planetary wave activity is analysed by means of  $\overline{v'T'}$  for the gravity wave simulations. In Fig. 4.16 the annual cycle of Southern hemispheric eddy heat flux at 100 hPa resolved by

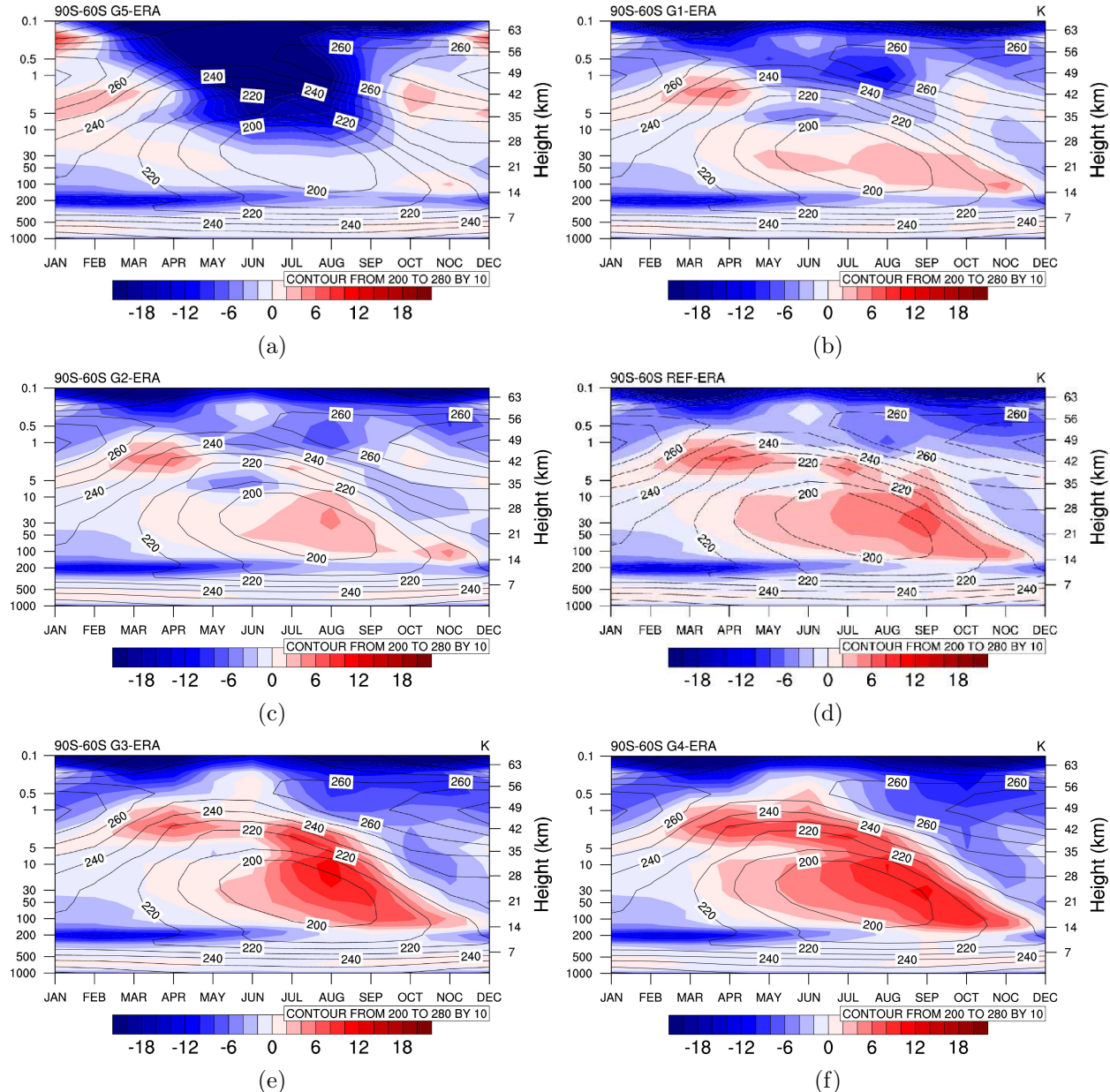


Abbildung 4.15: Annual cycle climatology of  $90^{\circ}\text{S}$  -  $60^{\circ}\text{S}$  mean temperature anomaly to ERA-Interim given in K for a)G5, b)G1, c)G2, d)REF, e)G3 and f)G4 simulations. Solid contour lines refer to the absolute values of ERA-Interim.

the wavenumber 1 to wavenumber 3 is presented. The calculation procedure is identical to the analysis described in the SST sensitivity experiments (see Sec. 4.2.2). Analogous to the results shown before, the largest portion of eddy heat flux is attributable to wavenumber 1, hence in the following the description of heat flux only refers to the contribution of wavenumber 1.

Beginning with G5 (Fig. 4.16(a)), the sensitivity run without parameterised non-orographic gravity waves, the seasonal evolution of  $\overline{v'T'}$  is fairly well reproduced compared to ERA-Interim. The annual peak in October with approximately  $-8 \text{ Kms}^{-1}$  is well captured by the G5 simulation. The largest deviations to the reanalysis data occur in the period from June to September, with a maximum difference of  $-1.5 \text{ Kms}^{-1}$  in September. For August and September these deviations are comparatively small, particularly if the standard deviation of ERA-Interim is considered, which are  $1.4 \text{ Kms}^{-1}$  in August and  $3.4 \text{ Kms}^{-1}$  in September, respectively (standard deviation is not explicitly shown).

Regarding the simulations including non-orographic gravity wave parameterisation, the annual cycle of planetary wave activity derived from the individual realisations is clearly distinguishable from each other. Initially, simulations with a smaller *rmscon* parameter and thus smaller stratospheric gravity wave drag compared to REF are described. In G1 (Fig. 4.16(b)) the strongest heat flux within the year during October is well represented, but early winter  $\overline{v'T'}$  especially June planetary wave activity is overestimated by  $1.3 \text{ Kms}^{-1}$ , which is the same order of magnitude obtained by the G5 simulation in July, but in late spring and early summer heat flux is underestimated by  $1.7 \text{ Kms}^{-1}$ . The G2 (Fig. 4.16(c)) simulation can be qualitatively characterised by an overestimated  $\overline{v'T'}$  during winter season followed by underestimated heat fluxes in the spring months. Overrated heat fluxes, with differences of  $1.7 \text{ Kms}^{-1}$  in July tend to be larger than in G1. However, the September heat flux is approximately  $-5 \text{ Kms}^{-1}$ , which is almost  $3 \text{ Kms}^{-1}$  below the corresponding heat flux in ERA-Interim.

The sensitivity simulations with larger gravity wave dissipation at stratospheric levels than in REF, namely G3 (Fig. 4.16(e)) and G4 (Fig. 4.16(f)), show a shifted annual cycle of  $\overline{v'T'}$  in regard with reanalysis data. The strongest heat fluxes of the year do not occur in October any more, but now the peak rises one month earlier in September. Furthermore, in the winter months JJA  $\overline{v'T'}$  are considerably overestimated, whereas in spring terms the fluxes are underestimated. In G3 during the winter season the heat flux is on average  $2 \text{ Kms}^{-1}$  larger than in ERA-Interim, whereas the deviations in G4 are even larger, e.g. in August values in G4 exceed the reanalysis data by roughly  $4 \text{ Kms}^{-1}$ . In late spring terms from October to November the heat flux of both sensitivity runs clearly show smaller values compared to ERA-Interim.

The meridional eddy heat fluxes calculated from the gravity waves sensitivity simulations are based on a 6 year time-slice experiments. Therefore, longer time series have to be taken into account in order to obtain statistical evidence. However, this set of simulations presents a quite robust systematic change in the annual cycle of  $\overline{v'T'}$  if the *rmscon* parameter is enlarged. With an increasing *rmscon* parameter, it becomes more and more apparent that the seasonal cycle of eddy heat flux is shifted by one month ahead. Furthermore, considering the Newman-correlation, which describes the interrelation of planetary

wave activity with stratospheric temperature, the changes in  $\bar{v'T'}$  introduced in this section are consistent with the detected Antarctic temperature anomalies shown above (see Fig. 4.15). Thus, this systematic change of  $\bar{v'T'}$  seems to be a reliable result. Independent from the chosen gravity wave parameter  $rmscon$  the model tends to overestimate planetary wave activity in early winter.

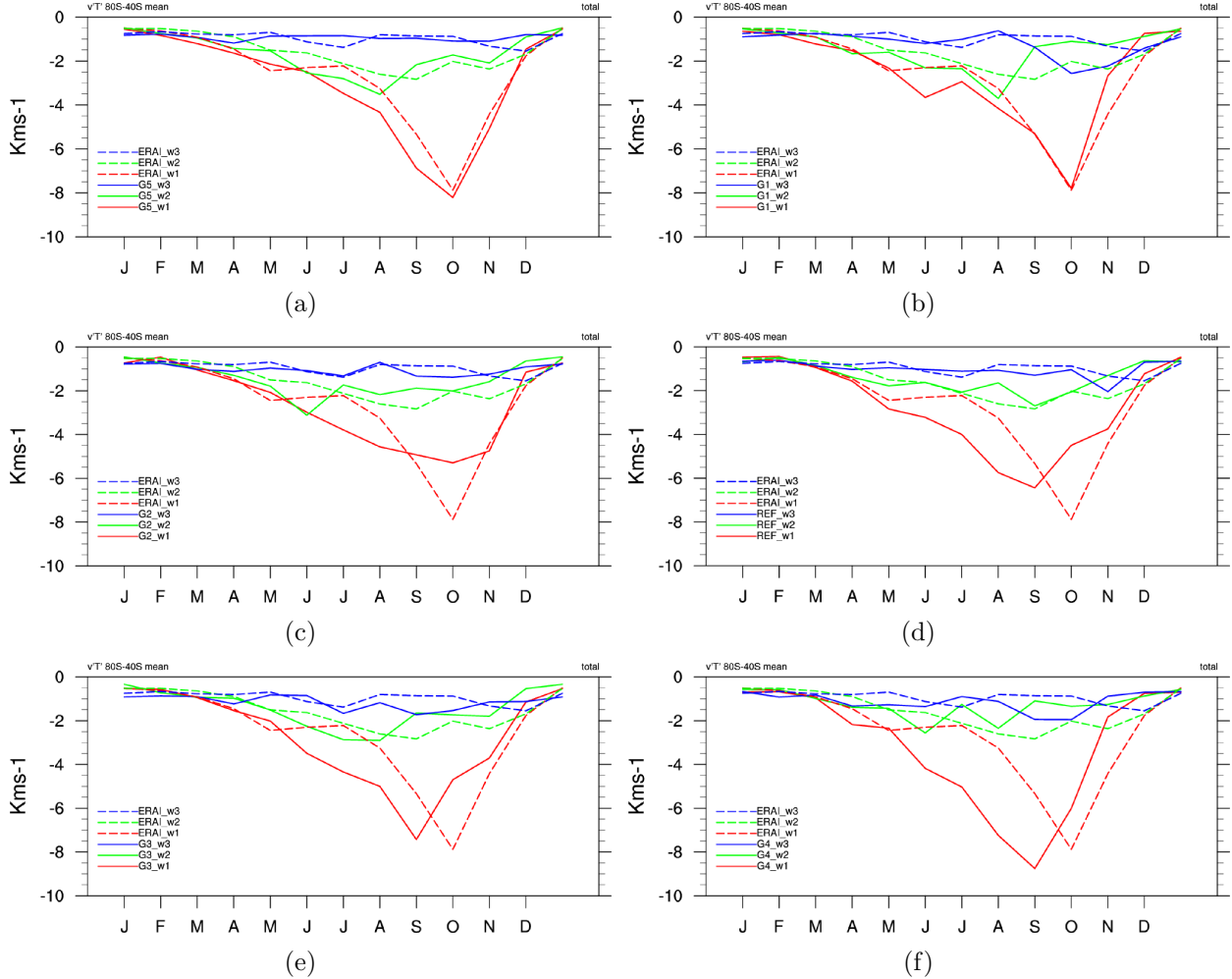


Abbildung 4.16: Annual cycle climatology of  $40^{\circ}\text{S} - 80^{\circ}\text{S}$   $\bar{v'T'}$  at 100 hPa given in  $\text{Kms}^{-1}$  for a)  $G5$ , b)  $G1$ , c)  $G2$ , d)  $REF$ , e)  $G3$  and f)  $G4$ . Solid lines refer to the corresponding simulation and the dashed line to ERA-Interim, respectively.

### Latitude-Height Cross Section of Temperature

In order to better meet the requirements of the three dimensional structure of the polar vortex, latitudinal height cross section are also analysed. The focus is on the Austral winter (JJA) and spring season (SON) when the stratospheric temperature bias of the Southern hemispheric polar cap is greatest.

In Fig. 4.17(a)-(f) the latitude height cross section of JJA mean temperature anomalies to ERA-Interim are shown. For all gravity waves sensitivity, including G5 the simulation without non-orographic gravity wave parameterisation, a striking warm bias feature at 60°S and a vertical extension from 100 hPa to 1 hPa can be determined. At the stratopause levels at roughly 1-5 hPa this warm bias is comparably large for all simulations and can exceed 10 K. However, the stratospheric part of this feature is strongly dependent on the choice of the *rmscon* parameter and the warm bias here rises with an increasing *rmscon* parameter.

In the G5 (Fig. 4.17(a)) sensitivity simulation the pattern of the anomalies is also dominated by a strong cold-pole bias situated at latitudes higher than 60°S and with a vertical extent from the upper tropopause to the lower mesosphere. In middle stratospheric levels at roughly 10 hPa values can drop more than 20 K below the corresponding temperature in ERA-Interim.

Accounting for the effects of non-orographic gravity waves this cold pole bias reduces. Qualitatively the Southern hemispheric warm bias increases with an increasing *rmscon* parameter. In particular, at the polar latitudes from roughly 90°S - 60°S the middle atmospheric warm bias seems to be strongly correlated to the effects of the gravity wave parameterisation. However, the temperature rise in the lower stratosphere is accompanied by an increase in  $\bar{v}'T'$ , which was demonstrated above. Therefore, temperature changes here can be very likely attributed to an enhanced planetary wave activity. The corresponding warm bias at upper levels from stratosphere at 30 hPa to the mesosphere are probably rather induced by other effects, presumably to effects which are related to gravity wave activity. For example, Boville (1984) demonstrated a major role of gravity waves in the contribution of warming the middle atmosphere with a significant influence down to 30 km height during winter season.

Nevertheless, with regard to the warm bias feature at the 60°S latitude, alterations of gravity wave activity seem to play only a minor role, since this feature remain in all sensitivity simulations independently from the setting of the *rmscon* parameter.

Similar to the JJA mean, a warm bias feature at 60°S appears independently from non-orographic gravity wave parameterisation in the temperature anomalies of the SON season (see Figures 4.18(a)-(f)). But in SON only the stratopause proportion remains. Interestingly a similar feature can be found in the Northern hemisphere at 60°N.

During Austral spring season (SON) for all gravity wave sensitivity simulations a characteristic anomaly pattern of the polar Southern hemisphere can be identified. This structure can be described as a positive anomaly in the upper tropospheric, lower stratospheric levels followed by a negative anomaly aloft.

In G5 (Fig. 4.18(a)), which does not account for non-orographic gravity waves, a warm bias with a maximum of 4 K centred around 100 hPa level can be detected. From 30 hPa onward to 0.1 hPa a cold bias of maximum 8 K occurs. The positive anomaly at 100 hPa intensifies with an increasing *rmscon* parameter. The maximum of this warm bias in G1 (Fig. 4.18(b)) is 6 K and gradually rises between the individual sensitivity simulations and eventually reaches values of 14 K in the G4 simulation (Fig. 4.18(b)-(f)). This amplification goes along with an vertical spread, beginning with G1 where a vertical extent of this warm

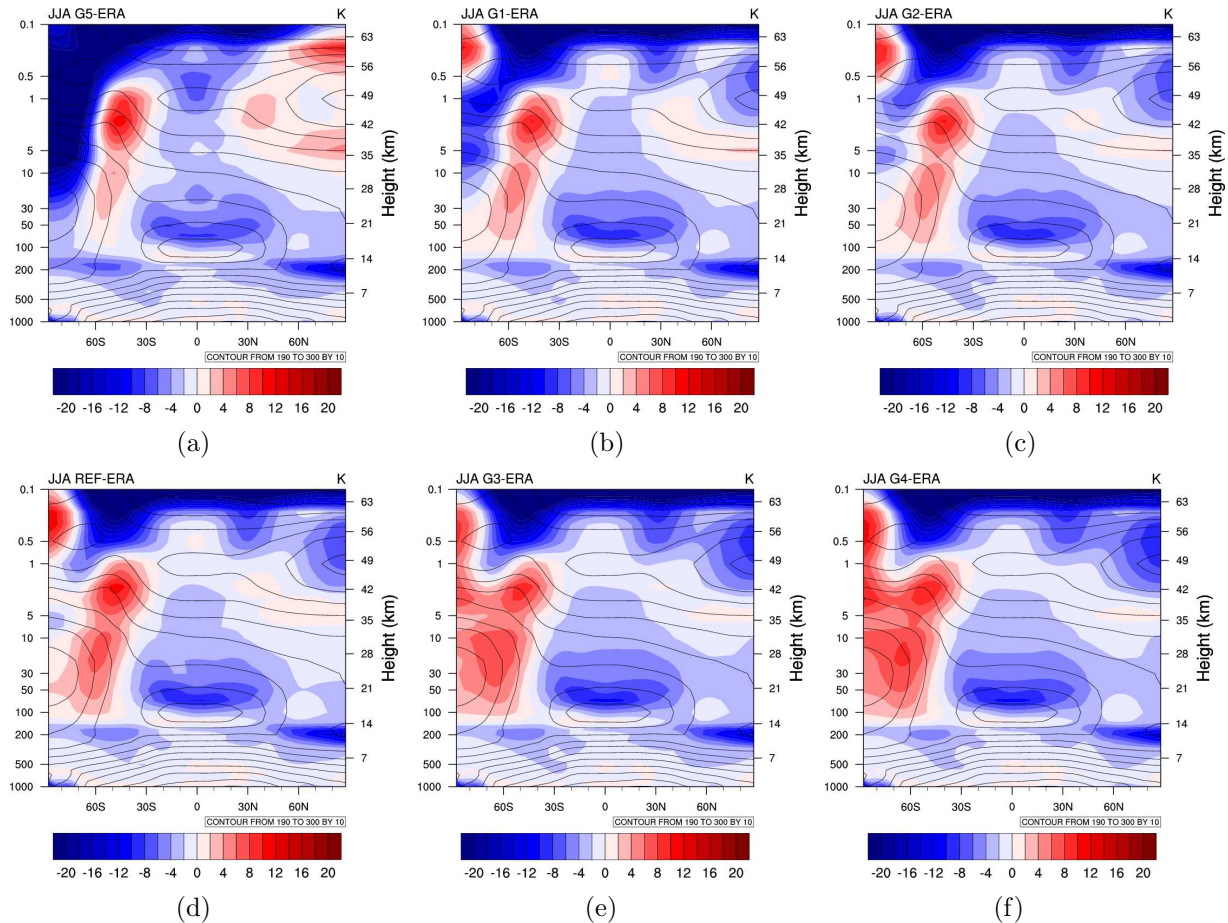


Abbildung 4.17: Latitude-height cross section of seasonal mean JJA temperature anomaly of simulation minus ERA-Interim given in K for a)G5, b)G1, c)G2, d)REF, e)G3 and f)G4. Black contour lines refer to ERA-Interim only values.

anomaly forms roughly from 200 hPa to 30 hPa and evolving in G4 to a warm bias with a vertical extent from 200 hPa to 10 hPa. In parallel, analogous to the described warm bias, an intensification of the cold bias can be seen. For G1 the lower mesospheric minimum at 0.5 hPa is approximately -6 K and for G4 it is -12 K, respectively.

Considering the above analysed  $v' T'$ , which shows an underestimation compared to the reanalysis data, the detected warm bias during SON probably is not caused by planetary wave activity such as it was the case during the JJA season. A comparable morphology to the Southern hemispheric SON temperature anomalies presented here, is reported by Labitzke (1972) for the Northern hemisphere. She demonstrated that after vortex breakdown within a so called mid winter warming event, polar stratospheric temperature up to approximately 40 km height increases and beyond that level entering the mesospheric levels temperature decreases (see Fig. 11 in Labitzke (1972)). Regarding the fact that the SON season is the period when winter turns into spring and, thus, the polar vortex breaks down, the findings in Labitzke (1972) could be an indication for a premature conversion of polar vortex winter properties to spring conditions.

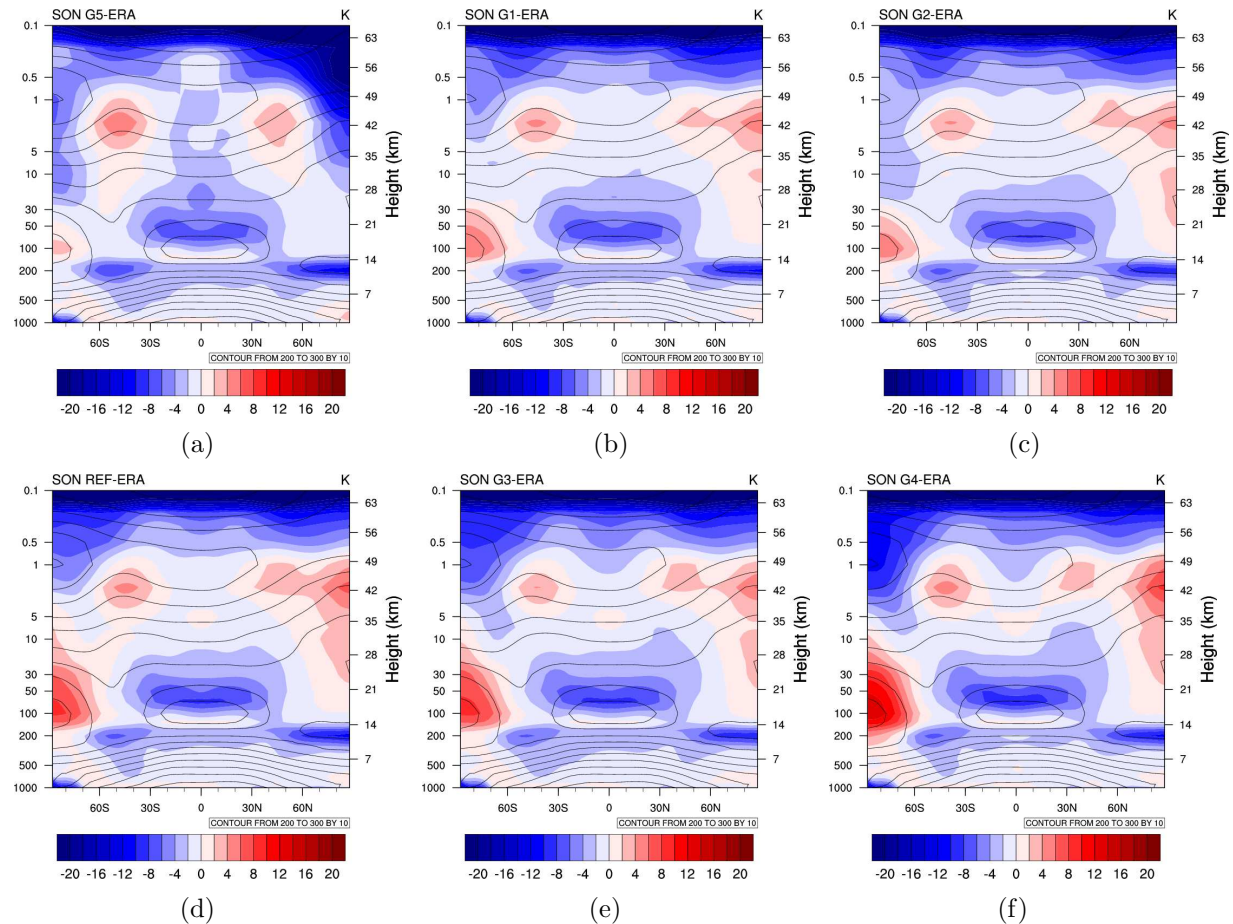


Abbildung 4.18: Analogous to 4.17, but for SON season.

#### 4.2.5 Discussion of Gravity Wave Sensitivities

The analysis of SST sensitivity studies gave indications, that the Southern hemispheric winter polar vortex is weakened remarkably by gravity wave activity. Therefore, sensitivity simulations with altered *rmscon* parameters are conducted. It can be demonstrated that a raised *rmscon* parameter leads on average to stronger gravity wave fluxes as well as an enhanced gravity wave drag in the polar regions of the stratosphere. These changes in the effects of the parameterised gravity waves lead to striking changes in the temperature anomaly field across the individual sensitivity simulations.

By means of the annual cycle of polar cap (90°S - 60°S) temperature anomalies, which is considered as a measure for the strength of polar vortex, it is illustrated that the model warm bias during Austral winter and spring intensifies with increasing the *rmscon* parameter. Due to the linear correlation of planetary wave activity and lower stratospheric temperature as determined by Newman et al. (2001), this intensification of the warm bias can partly be attributed to the changes in planetary wave activity analysed by  $\overline{v'T'}$ . The annual cycle of  $\overline{v'T'}$  undergoes a gradual temporal shift of approximately one month ahead towards ERA-Interim data, if *rmscon* values are enlarged. The consequences of this shift can be broadly described as an enhancement of planetary wave activity during JJA and a decrease in the spring season SON. Thus, following the arguments of Newman et al. (2001), late winter positive temperature anomalies of lower stratospheric level up to roughly 50 hPa, can be assigned to implications of planetary wave activity, whereas during spring other drivers must contribute to the positive anomalies detected in the models.

For polar winter temperature anomalies located at higher altitudes, such as from middle stratospheric to stratopause level, the implications of gravity waves play a more important role (Hitchman et al., 1989; Boville, 1984). Mesospheric gravity wave dissipation induces a dynamical downwelling leading to an adiabatic heating. Such dynamical heating effects can propagate downward to middle stratospheric levels of approximately 30 km height (Boville, 1984). This means that enhanced gravity wave dissipation during winter terms can explain an increased warming at atmospheric heights above 30 km. The Figures 4.19(a)-(b) illustrates polar gravity wave drag and flux of the individual sensitivity simulations at 60°S for the JJA season. A consistent picture is presented, since simulations with larger *rmscon* parameter such as G3 and G4 evince in the entire stratosphere and lower mesosphere (roughly up to 0.1 hPa) larger gravity wave fluxes than compared to G1 and G2, which has smaller *rmscon* parameters. Above 0.1 hPa the situation is reversed and gravity wave fluxes of G3 and G4 are smaller than in G1 and G2. This circumstance can be explained by the corresponding gravity wave drag (Fig. 4.19(b)). The gravity wave drag at mesospheric levels (about levels above 1 hPa) shows larger that values for G3 and G4 are larger compared to G1 and G2, which leads to a stronger attenuation of the respective gravity wave flux. Above 0.1 hPa situation for gravity wave drag again is different, but integrating the wave drag over the entire vertical extent of the mesospheric domain, the obtained gravity wave drag in simulations with larger *rmscon* parameter is stronger compared to simulations with smaller *rmscon* parameter.

Generally, in the winter months JJA increasing the *rmscon* parameter leads to an

amplification of the overall non-orographic gravity wave activity, which is accompanied by enhanced planetary wave activity depicted as  $\bar{v'}\bar{T'}$ . A considerable relationship between resolved planetary wave activity and unresolved parameterised waves in GCMs is discussed in some previous studies (Cohen et al., 2013, 2014; Gerber, 2012). Cohen et al. (2013) present in their work an effect, where implications of planetary wave driving is balanced by unresolved parameterised wave driving. This compensational effect is demonstrated in particular by orographically induced gravity waves and planetary waves. However, they also discussed a possible increase of net planetary wave driving, as a result of a weakened polar vortex induced by the alteration of the non-orographic gravity wave scheme, which would qualitatively support the results presented here for the JJA season. In addition, Cohen et al. (2014) confirmed this assumption, showing that non-orographic gravity waves are not compensated by planetary waves but rather enhance the weakening of the polar vortex during winter terms.

In contrast to the winter season, polar temperature anomaly fields in spring months SON, are characterised by a lower stratospheric positive anomaly with a negative anomaly aloft. If the *rmscon* parameter is raised, the amplitudes of positive as well as negative anomalies are increased, and the lower stratospheric warm bias enlarges vertically. Numerical as well as observational studies can show that this characteristic anomaly pattern is also detectable after a vortex breakup, during the so-called mid winter warming events (e.g. Labitzke, 1972; Limpasuvan et al., 2012). This finding and the fact that planetary wave activity is shifted by one month ahead, give strong indications for a premature transition of polar vortex properties from winter to spring season.

In addition, the analyses of parameterised non-orographic gravity waves reveal a similar picture. The strongest decrease of gravity wave flux during SON can be found at stratospheric heights around 30 hPa (Fig. 4.19(c)), whereas corresponding gravity wave drag is the largest at the lower mesospheric level (Fig. 4.19(d)). Considering middle atmospheric altitudes, gravity wave fluxes of configurations with larger *rmscon* parameter (i.e. G3 and G4) decrease the strongest with height.

Following McLandress and Scinocca (2005), gravity wave flux only can be changed as a result of two different mechanisms. The first type is referred to as critical-level (CL) filtering. This is the case when the wind speed of the background field and phase velocity are close together. Hence, waves which have undergo CL filtering do not contribute to the further upward propagating wave spectrum. Consequently, the background wind field is only permeable for certain waves.

The second mechanism alternating gravity wave flux can be described by non-linear effects, which occur when the amplitudes of vertically propagating waves increase until they become unstable and break. This breaking causes a force to the background mean flow, which is reflected in the gravity wave drag. Comparing gravity wave flux and drag of SON season (see Fig. 4.19(c), Fig. 4.19(d)) it becomes clear that critical-level filtering is very likely the cause of the detected strong reduction of gravity wave flux. As mentioned above the largest wave drag is detected at mesospheric levels whereas the largest reduction of wave fluxes can be seen at the lower stratospheric levels.

Possible causes for this considerable critical-level filtering can be induced by a dramatic

change in the background wind field, which is the case when the polar vortex undergoes the transition from winter to spring and westerlies turn into easterlies. So analyses of gravity wave sensitivity studies give further indications for a premature conversion from winter to spring season.

It should be born in mind that the results of gravity wave sensitivity are based on 6 year simulations and therefore more years have to be taken into account for statistical relevance. However, all simulations were performed in time-slice mode, signifying annual repeated boundary conditions which keeps the externally forced uncertainties low. Furthermore, systematically consistent changes in the anomaly fields are detected when altering the *rmscon* parameter. These changes can be related to physical processes and therefore the underlying causes can be explained. In this sense, the results presented for gravity waves sensitivity are qualitatively robust.

Regarding the decadal climate prediction system the findings of gravity wave sensitivity studies clearly shows the importance of gravity parameterisation regarding the representation of Southern hemispheric polar vortex. However, the interplay of the effects of parameterised waves and resolved planetary waves remains unclear and deeper researches are required in order to improve model simulations.

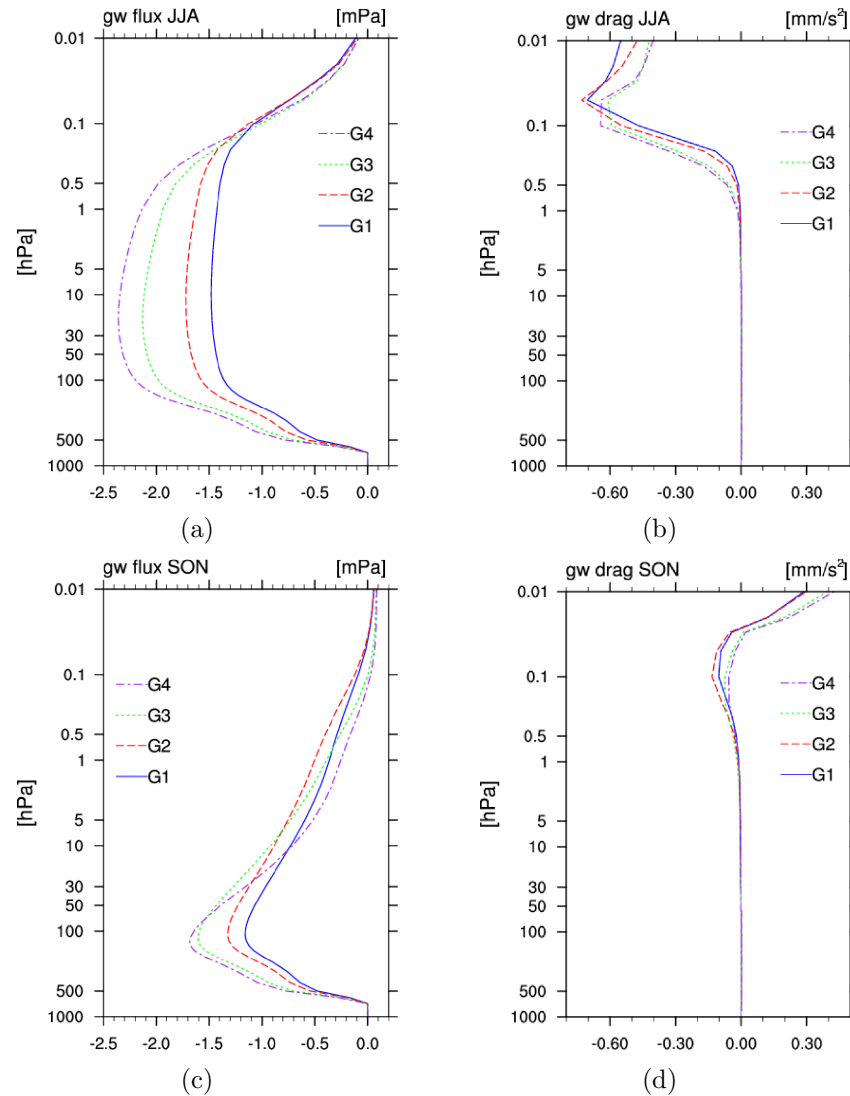


Abbildung 4.19: Height cross section of seasonal mean gravity wave flux and wave drag averaged at  $60^{\circ}\text{S}$ . a), b) are seasonal mean of JJA and c), d) for SON, respectively.

#### 4.2.6 Resolution Sensitivity

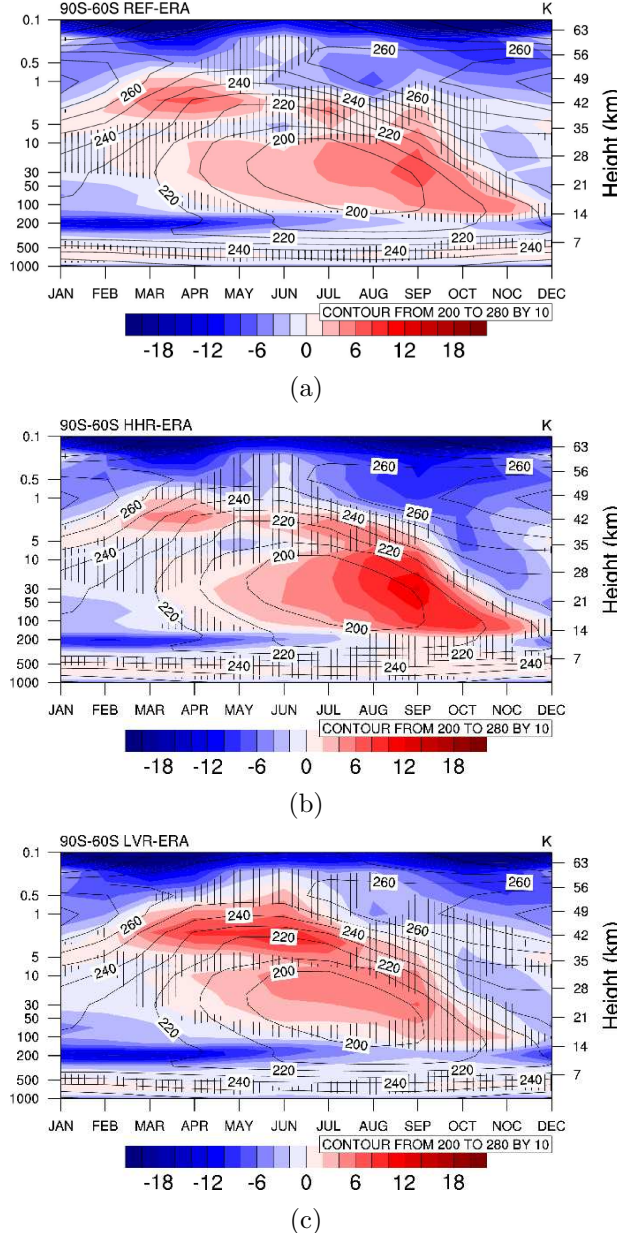


Abbildung 4.20: As in Fig. 4.11, but for a)REF, b)HHR and c)LVR. Shaded areas are not significant according to 2 sided t-test with a 95% confidence level.

son. At the stratopause level between 1-5 hPa the warm bias already can occur in the

The previous sections demonstrated considerable effects of SSTs and non-orographic gravity waves on the model dynamics. Apart from these two drivers model resolution can also have significant implications on the atmospheric general circulation. For example, planetary wave activity can be affected by vertical as well as horizontal resolution (Roeckner et al., 2006), but also gravity waves and in particular their wave spectra are influenced by model resolution and therefore interactions between gravity waves and the background mean flow are dependent on resolution (Andrews et al., 1987; Hayashi et al., 1989; Hamilton, 1996). This section analyses the effects of different model resolutions on the dynamics of the Southern hemispheric polar vortex.

Apart from the REF simulation with a T42L90 configuration two further resolution sensitivity simulations were performed. One simulation with **H**igher **H**orizontal **R**esolution T63L90 named **HHR** and a second with **L**ower **V**ertical **R**esolution with T42L47 configuration named **LVR**. For details and description of the corresponding simulation setups see Sec. 2.2.3.

The Fig. 4.20 show the ten year climatological mean annual cycle of the Antarctic polar cap ( $90^{\circ}\text{S}$  -  $60^{\circ}\text{S}$ ) temperature anomalies, considered as the differences of the respective model resolution to ERA-Interim. Positive anomaly values refer to overestimated modelled temperature compared to reanalysis data, and negative ones to an underestimated temperature accordingly. Similar to the previously discussed sensitivity studies, all resolution simulations suffer from a considerable warm bias at stratospheric altitudes during winter to spring sea-

autumn (MAM). Statistical evidence for these model deviations are given by a two sided Student t-test. As mentioned before, due to sponge layer effects the levels above 0.5 hPa are not taken into consideration.

Qualitatively the arising anomaly pattern of the individual models have similar characteristics. However, differences particularly occur in the amplitudes of the warm bias. For example, in the low vertical resolution configuration LVR (Fig. 4.20(c)) a significant warm bias in the stratopause level with maximum values about 10 K is stronger compared to REF and HHR. Furthermore, stratopause anomalies in LVR persist constantly without any interruptions from autumn to the onset of spring, whereas in the other model configuration the significant warm bias is predominantly confined to the MAM season. Looking at middle stratospheric to upper tropospheric altitudes at roughly 10-100 hPa the warm bias in LVR is now weaker than in REF. The largest positive deviations to ERA-Interim in LVR are 4 K, however, in REF maximum values can reach 8 K, especially in September during the winter to spring transition. In LVR the anomalies here are statistically not significant in this region.

Comparing the higher horizontal resolution simulation HHR (Fig. 4.20(b)) with REF the gravest differences in the anomaly pattern arise during the spring migration period in September and its following months. Maximum values in REF here are about 8 K, whereas in HHR locally the positive anomaly can exceed 10 K. This intensification of the warm bias is already indicated in the winter terms JJA, where the positive anomalies in HHR temporarily develop more strongly than in REF. Furthermore, the negative anomalies in the upper stratospheric levels during SON of the HHR configuration tend to be generally stronger than in REF.

The described polar vortex temperature anomalies of the different model simulations arise from their individual resolution configurations. As previously mentioned vertical as well as horizontal resolution has considerable implications on the model dynamics. Therefore, possible dynamical drivers of these anomalies are analysed and discussed below.

### Meridional Eddy Heat Flux

In the previous sensitivity studies of this work it is demonstrated that the largest fraction of Southern hemispheric planetary wave activity is regarded as the meridional eddy heat flux at 100 hPa for the latitudinal mean of  $80^{\circ}\text{S}$  -  $40^{\circ}\text{S}$  ( $\overline{v'T'}$ ), which is dominated by its planetary wavenumber 1 compound. For this reason in this section solely the planetary wavenumber 1 compound of  $\overline{v'T'}$  is considered. Analysing the annual cycle of  $\overline{v'T'}$  substantial differences appear between the different model simulations (Fig. 4.21). As previously discussed, the annual course of eddy heat flux in the REF simulation is less pronounced and shifted by 1 month ahead compared to ERA-Interim. Additionally, it can now be noticed that during the winter seasons JJA the corresponding standard deviation of REF is approximately twice as large as in the reanalysis data. This could be analogous to the Boreal winter situation, where the Northern hemispheric polar vortex evinces a large inter-annual variability due to a comparatively high planetary wave activity.

The seasonal evolution of  $\overline{v'T'}$  in the HHR configuration (Fig. 4.21(b)) resembles the

sensitivity simulations with an enlarged gravity wave parameter (see Sec. 4.2.4). Similar to the REF simulation the annual absolute maximum is shifted by one month ahead compared to reanalysis data. However, in contrast to the REF setup maximum values of  $\overline{v'T'}$  in HHR are now about  $-8 \text{ Kms}^{-1}$ , which is roughly the same magnitude as in ERA-Interim. The resemblance of meridional eddy heat flux in the HHR configuration to gravity wave sensitivity simulations could be explained by the fact, that an increased horizontal resolution can enhance the effects of gravity waves (Hayashi et al., 1989; Hamilton, 1996).

The annual cycle characteristics of the low vertical resolution configuration LVR are clearly distinguishable from the other simulations with different resolution. From January to September the temporal evolution of planetary wave activity agrees fairly well with ERA-Interim. The largest detected deviations of LVR from reanalysis can be found within the  $1\sigma$ -standard deviation of ERA-Interim. But from September onwards  $\overline{v'T'}$  is underestimated. For example, during October the values in LVR are about  $-5 \text{ Kms}^{-1}$  whereas in ERA-Interim  $-8 \text{ Kms}^{-1}$  are reached. But the largest differences between model and reanalysis occurs, when the  $1\sigma$ -standard deviation during winter months JJA are regarded. For ERA-Interim the standard deviation here is about  $1 \text{ Kms}^{-1}$  and for LVR values larger than  $3 \text{ Kms}^{-1}$  can be detected, which is also larger than the corresponding standard deviation derived from the REF simulation.

Generally the migration periods from winter to spring in all model configurations is shifted by one month ahead compared to ERA-Interim. This is reflected on the one hand by an overestimation of  $\overline{v'T'}$  during JJA and on the other by the underestimation in SON. This is most clearly seen in the HHR simulation whereas in LVR differences are the smallest. However, in JJA the inter-annual variability considered as the  $1\sigma$  standard deviation of the models is distinctly larger than in the reanalysis. In particular the inter-annual variability of the LVR configuration is strongly over represented compared to its mean value of  $\overline{v'T'}$  and therefore could contribute to the afore described model warm bias.

### Latitude-Height Cross Section of Temperature

In addition to polar cap mean temperature, latitude-height cross sections are also analysed, in order to give a more complete picture of the three dimensional structure of the polar vortex. In figure 4.22 the differences of the climatological mean of zonal mean temperature to ERA-Interim for the JJA mean are shown. Positive anomalies refer to a model warm bias and negative anomalies to a cold bias, respectively. In the Southern hemispheric winter stratosphere a prominent warm bias feature occurs in all model configurations. It is roughly located at  $60^\circ\text{S}$  with a vertical extent from the upper troposphere to the stratopause. The largest difference can be found at the stratopause level around 1 hPa with a maximum of approximately 12 K. The significant deviations in the upper tropospheric to middle stratospheric altitudes can reach values up to 8 K, but the HHR configuration anomalies here are the most pronounced compared to the other resolution setups.

Beside the fact of this Southern hemispheric warm bias feature, a cold bias at the tropopause level occurs in all model configurations. As discussed above this bias is a common feature of many GCM (IPCC, 2007; CCMVal, 2010). Righi et al. (2014) conducted

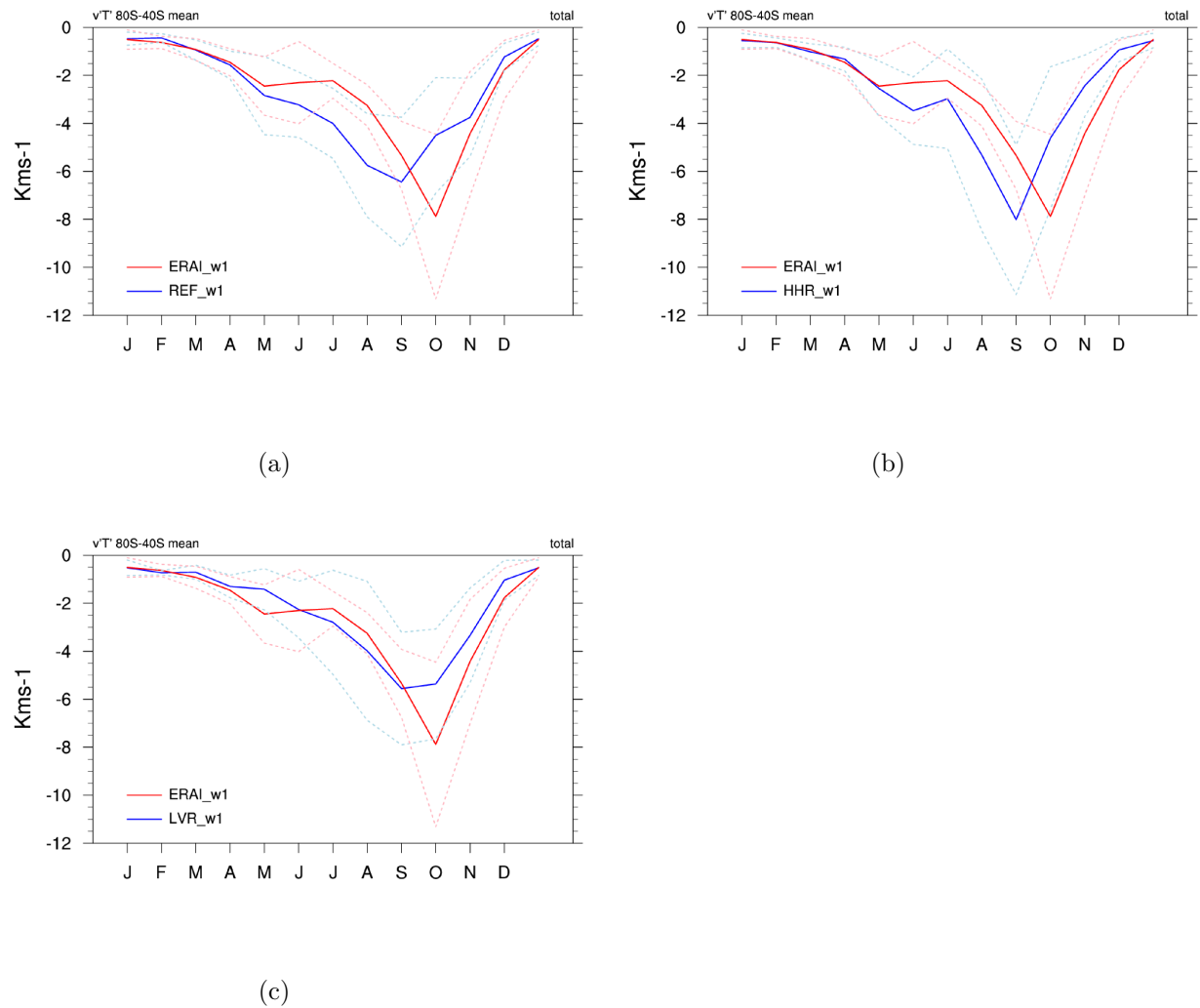


Abbildung 4.21: Wavenumber 1 component of the annual cycle of  $\bar{v}'T'$  at 100 hPa for  $80^{\circ}\text{S} - 40^{\circ}\text{S}$  mean given as  $\text{Kms}^{-1}$ . Dashed lines are the corresponding  $1\sigma$ -standard deviation. a) REF, b) HHR and c) LVR.

a comparable simulation to the REF configuration, and detected a similar temperature anomaly pattern. They could attribute the tropopause cold bias to an overestimation of water vapour in this region. As mentioned above water vapour here has a net cooling effect.

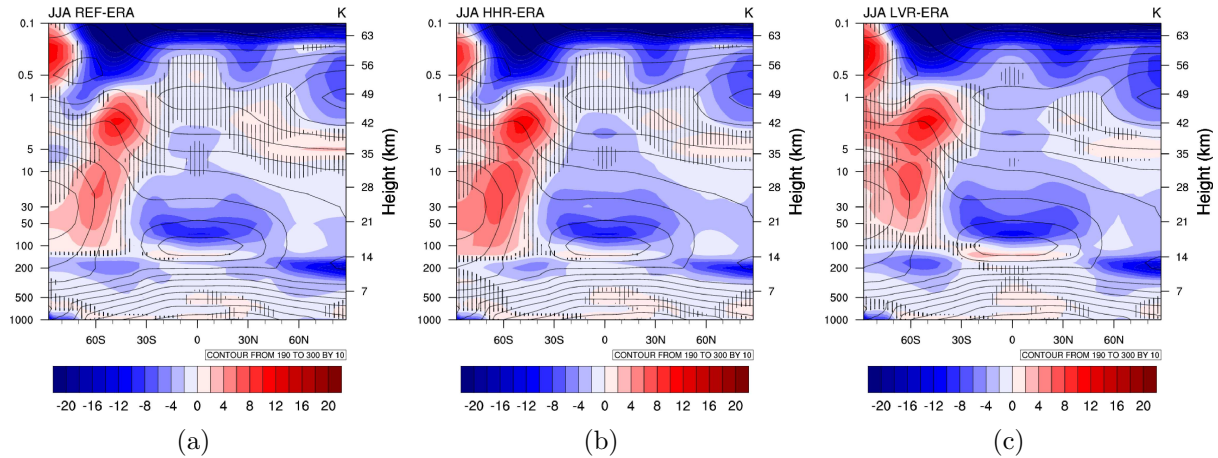


Abbildung 4.22: Analogous to Fig. 4.17. a)REF, b)HHR and c)LVR. Shaded areas are not significant at the 95 % level according a 2 sided t-test.

For the Austral spring season SON temperature anomalies are given in Fig. 4.23. The Southern hemispheric polar regions are characterised by a distinct warm bias in the lower stratospheric and upper tropospheric levels roughly from 100 to 30 hPa and a considerable cold bias aloft in the upper stratospheric lower mesospheric levels. In the HHR simulation these anomalies are most pronounced with maximum positive values up to 14 K and largest negative deviations of about -12 K. In REF the largest positive values can be found around 50 and 100 hPa with values about 10 K and negative anomalies at upper stratospheric levels are about -8 K large. In contrast to REF and HHR the corresponding temperature differences of LVR to ERA-Interim located in the Southern hemispheric middle atmosphere are predominately statistically not significant. However, remarkably the maximum stratopause warm bias feature in the JJA months situated between 60°S to 30°S and 5 and at 1 hPa altitude, also remains attenuated in the SON season for all model simulations. Significant values here can reach 6 K.

Regarding the Northern hemisphere for REF and LVR, a considerable warm bias in the middle to upper stratospheric levels and in particular the stratopause region can also be detected. Maximum anomalies here can reach 10 K. Considering the gravity waves sensitivity simulation without the parameterisation of non-orographic gravity waves, a pronounced cold bias arises in this region (see Fig. 4.18(a)). Therefore this model bias is very likely attributable to the effects of non-orographic gravity waves. Corresponding anomalies in HHR are also detectable but they are less pronounced and statistically not significant.

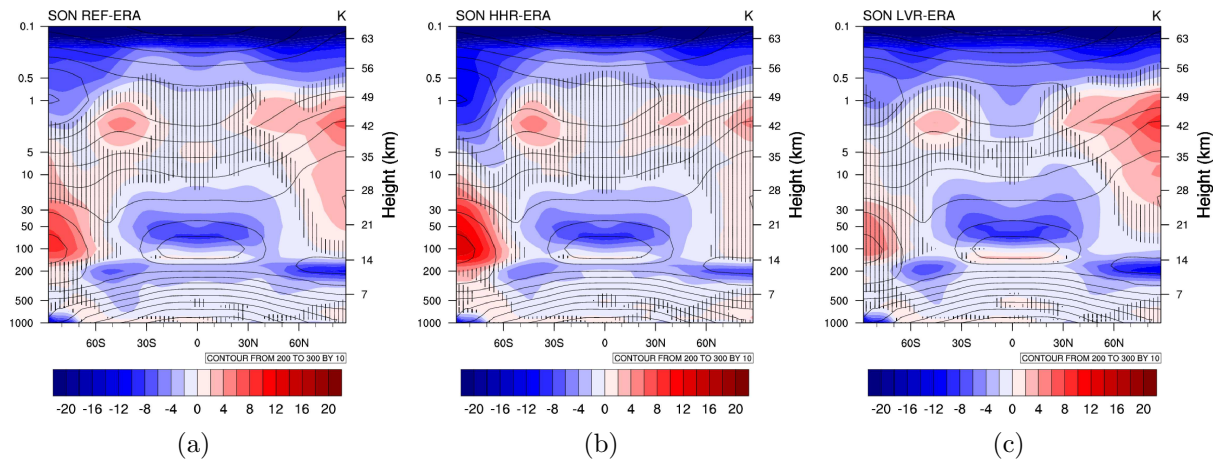


Abbildung 4.23: Analogous to Fig. 4.22, but for SON season. a)REF, b)HHR, c)LVR

### TEM Diagnostics

The diagnostics of the transformed Eulerian mean (TEM) equations are applied for studying the large-scale global zonal mean circulation of the stratosphere. Its concepts and theoretical background can be found in the Appendix C. Essential elements of the TEM diagnostics are the Eliassen-Palm (EP)-Flux analysis and the so called residual mass stream function  $\bar{\chi}^*$ .

In the following EP-Flux analyses are conducted in order to investigate atmospheric (predominantly planetary) wave propagation and its interaction with the background mean flow in more detail. The EP-Flux qualitatively represents the net propagation of planetary waves in the atmosphere, whereas the EP-Flux divergence describes the interaction between the eddies and the mean background flow, quantifying the transfer of momentum from atmospheric waves to the mean flow. For visualisation purposes EP-Fluxes are scaled following the recommendations of Edmon et al. (1980) (for details see Appendix C).

The Fig. 4.24 gives the seasonal, climatological mean of scaled EP-Fluxes and its corresponding divergences for JJA and SON derived from ERA-Interim. During solstice season (JJA) considerable EP-Fluxes can predominantly be found in the mid-latitudinal region of the Austral winter hemisphere (Fig. 4.24(a)). They originate in the troposphere and propagate upwards into middle atmospheric altitudes. In the middle atmosphere they can either be ducted towards the tropics or dissipate and deposit momentum, which is indicated by EP-Flux divergence. In the SON season the situation for planetary waves is different. Now, in both hemispheres vertically propagating waves occur. This is due to the fact that during solstice season the winds in the Northern as well as in the Southern hemisphere are mainly westerlies (see black contours Fig. 4.9(f) and Fig. 4.9(h)), which is the preferred background condition for the vertical propagation of large scale planetary waves (e.g. Holton and Hakim, 2013).

Strong tropospheric EP-Flux divergence especially in the vicinity of the tropopause are attributable to damping of synoptic scale waves and for the majority of their energy

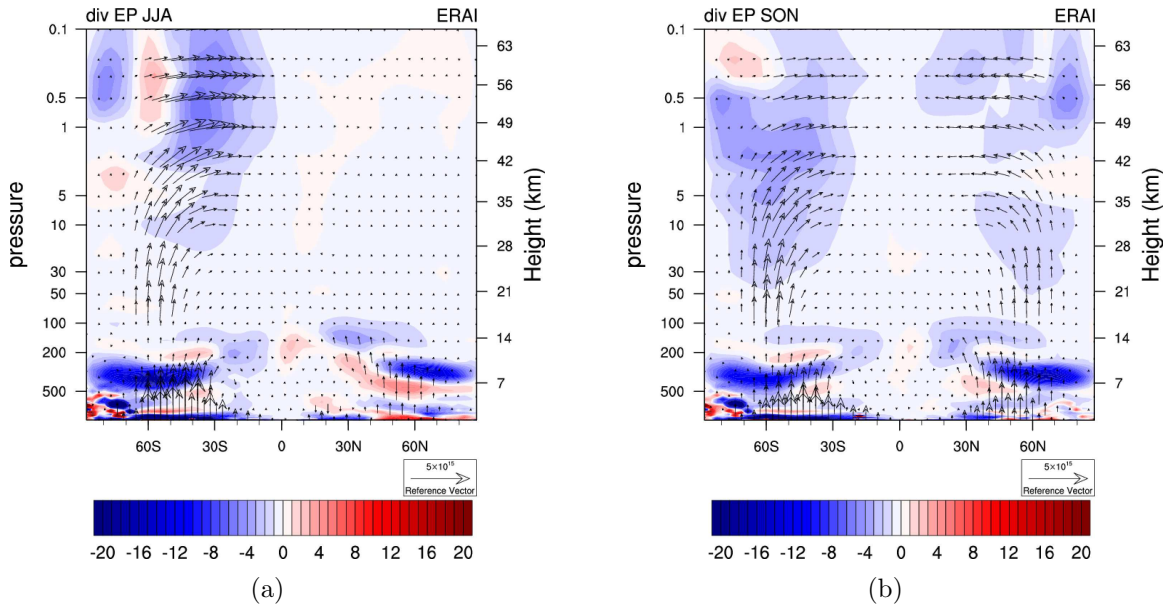


Abbildung 4.24: Scaled EP-Flux (arrows) and corresponding EP-Flux divergence (coloured) given in  $m/s/day$ . Underlying data are climatological means of ERA-Interim for a) JJA and b) SON. The horizontal arrow scale at bottom right is in units  $m^3$ . A vertical arrow of the same lengths is given in units  $m^3 Pa$ . For details see text and Appendix C.

remains in the troposphere (e.g. Holton and Hakim, 2013).

For the solstice season JJA differences of EP-Fluxes and divergence between simulations and reanalysis data are given in Fig. 4.25. Differences are derived from a ten year climatological mean. In all model configurations Southern hemispheric upward propagating planetary waves in the middle atmospheric region are overestimated. This is in agreement to the analysis of  $\bar{v'}T'$  given in Fig. 4.21. Larger EP-Fluxes are also accompanied by a significantly enhanced EP-Flux divergence at the upper stratospheric and lower mesospheric levels around  $60^{\circ}\text{S}$ . Southwards at higher latitudes significant positive EP-Flux divergence patterns can be found. The negative deviations of EP-Fluxes divergence can be associated with a deceleration and positive ones with an acceleration of the mean westerlies, respectively (Andrews et al., 1987). Consistent with this, the corresponding zonal wind anomalies e.g. of the REF simulation show for the Southern hemispheric polar night jet an acceleration southward of  $60^{\circ}\text{S}$  and a strong deceleration equator-wards (see Fig. 4.9(g)). Moreover, in contrast to the LVR simulation it can be noticed that model configurations with higher vertical resolution (i.e. REF and HHR) have a stronger upward and equator-ward wave flux in the middle atmosphere, particularly in the lower mesospheric upper and stratospheric altitudes and additionally their corresponding EP-Flux divergence can spread to lower latitudes, covering also subtropical regions. Differences here may arise from interactions with orographic gravity waves, which is discussed later.

Generally, changes in planetary wave activity, which are represented by wave propagation as well as wave dissipation, can lead to an alteration of the large-scale circulation of the

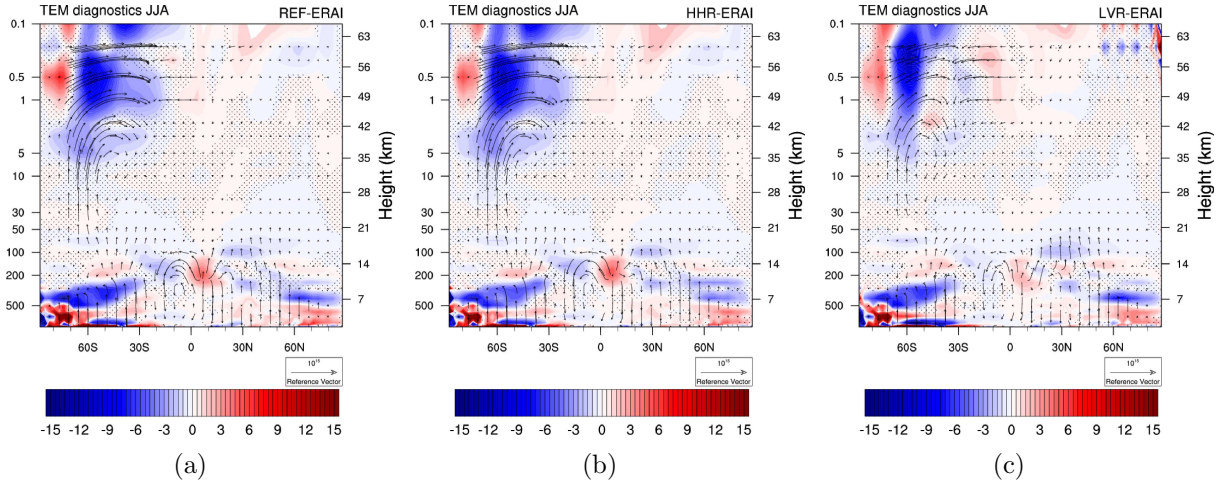


Abbildung 4.25: Differences of EP-Flux and divergence, model minus ERA-Interim for JJA mean. Scaling conventions and units are identical to Fig. 4.24. Shaded areas refer to EP-Flux divergence, which are statistically not significant to 95% level according to a 2 sided t-test. a) REF, b) HHR and c) LVR.

middle atmosphere. The implications of an overall too strong planetary wave activity by all model configurations during JJA season is analysed by means of the residual mass stream function  $\chi^*$ . The  $\chi^*$  is a measure for the zonal mean of large-scale meridional circulation in the middle atmosphere. The Fig. 4.26 gives the relative differences of model simulations compared to reanalysis data. Black contour lines denote the values of ERA-Interim only. Negative values indicate a southward transport and positive values a northward transport, respectively. In the JJA mean two cells can be identified, with a dominant circulation from the tropics into the Southern hemisphere (black dashed lines). Regarding the relative differences of the individual resolution configurations to ERA-Interim a similar anomaly pattern arises.

In particular significant negative deviations (exceeding 0.5%) in the Southern hemisphere roughly from 1 hPa to 100 hPa around the 60°S latitude have to be emphasised. Negative values here correspond to an enhanced downwelling over the Antarctic region. Descending air masses in turn can lead to a considerable adiabatic warming in the Southern hemispheric stratosphere during winter terms (e.g. Garcia and Boville, 1994). Regarding the simulated temperature differences shown in Fig. 4.22 the overestimated downwelling here is in a very good agreement to the above described model warm bias in the middle atmosphere during JJA.

However, the large negative Antarctic values (exceeding -2.5%) in the upper tropospheric and lower stratospheric region have to be considered with reservation. Here the residual mass stream function is dominated by its vertical component. However, in particular for the upper tropospheric, lower stratospheric region the calculation of  $\chi^*$  for ERA-Interim is based on different vertical levels than in the numerical model configurations. Since the vertical component of  $\chi^*$  is dependent on the vertical gradient of potential temperature,

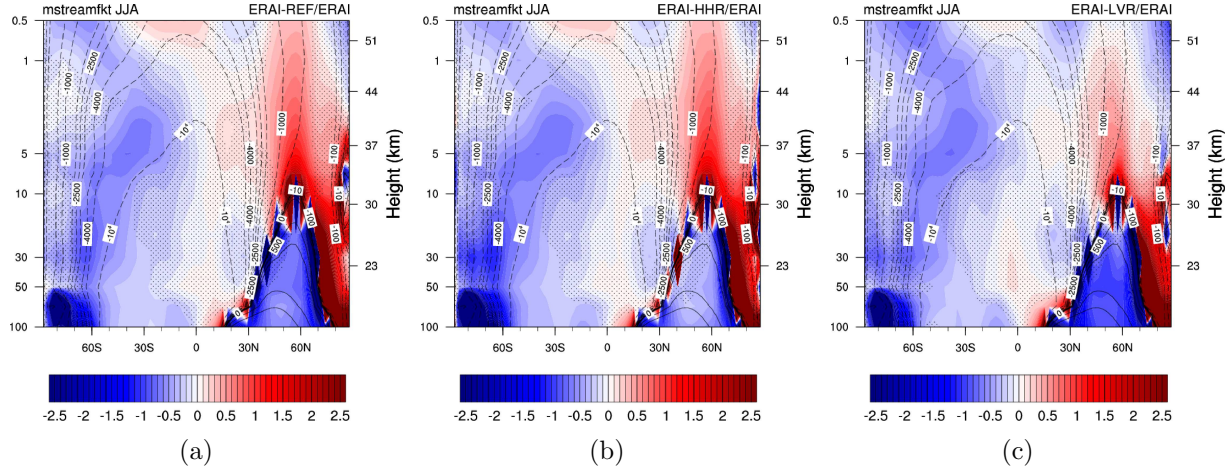


Abbildung 4.26: JJA mean of relative differences between model and ERA-Interim of  $\bar{\chi}^*$  given in %. Black contour lines refer to ERA-Interim only, given in  $10^9 \text{ kg/s}$ . Dashed contours indicates southward transport and solid contours northwards, respectively. Shaded areas are statistically not significant to 95% level according to a 2 sided t-test. a) REF, b) HHR and c) LVR.

this difference in the calculation can lead to spurious signals and therefore should not be taken into consideration.

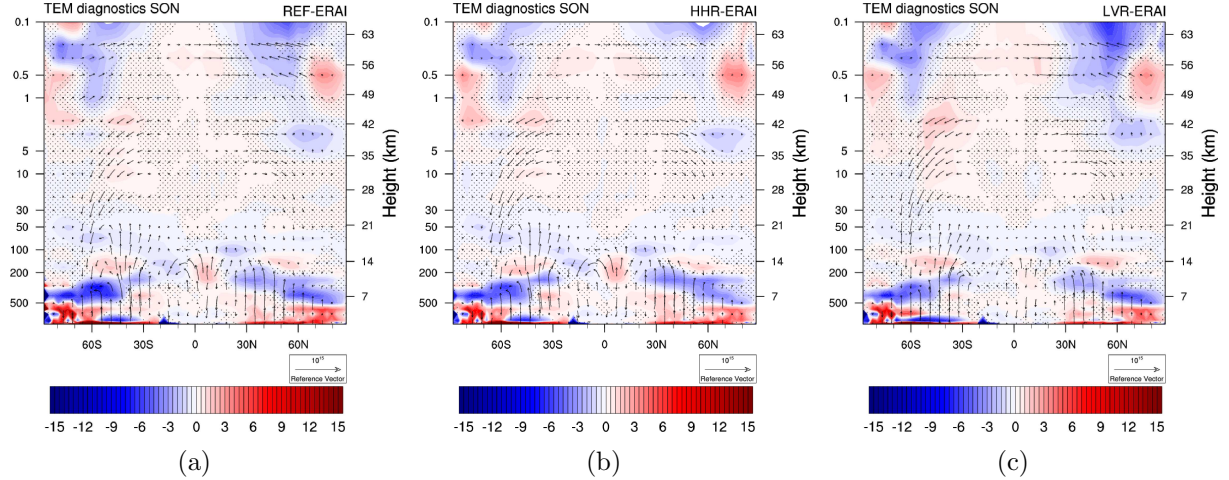


Abbildung 4.27: Same as in Fig. 4.25, but for SON season.

The situation constituting the TEM analysis during SON season is completely different to the Austral winter conditions. Southern hemispheric, polar planetary waves in the middle atmosphere are now underestimated in all model configurations compared to ERA-Interim. This is indicated by the clearly downward pointing EP-Fluxes in the entire Antarctic stratosphere given in Fig. 4.27. The corresponding deviations of EP-Flux divergence are mainly statistically not relevant particularly in the polar region of middle atmospheric altitudes. However, in the mid-latitudes to subtropical region at altitudes

from roughly 100 to 1 hPa level significant differences in the EP-Flux divergence occur in all model configurations. These differences can be categorised into a minor weakening up to  $1.5 \text{ m/s/day}$  at stratospheric levels from roughly 10 hPa - 1 hPa and a strengthening of similar magnitude in upper tropospheric, lower stratospheric altitudes between 100 hPa - 30 hPa.

Relative differences between models and reanalysis of  $\chi^*$  are given in Fig. 4.28 reflecting possible implications of planetary waves on the large-scale stratospheric circulation. In contrast to the JJA season the alterations of planetary wave activity during SON do not considerably affect the Southern hemispheric branch of the mean residual circulation. For the REF and LVR model setup the Southern hemispheric middle atmospheric deviations of  $\chi^*$  from ERA-Interim are predominantly statistically not distinguishable. However, in the HHR configuration a significant weakening (by roughly 30%) of the downwelling in the Southern polar region at 5 hPa - 1 hPa can be seen. This weakening is mainly determined by anomalies occurring during November (not shown). November is also the month when Austral winter conditions in the middle stratosphere turn into spring conditions (CCMVal, 2010). Thus, differences in the  $\chi^*$  described here are possibly related to the migration of winter to spring season.

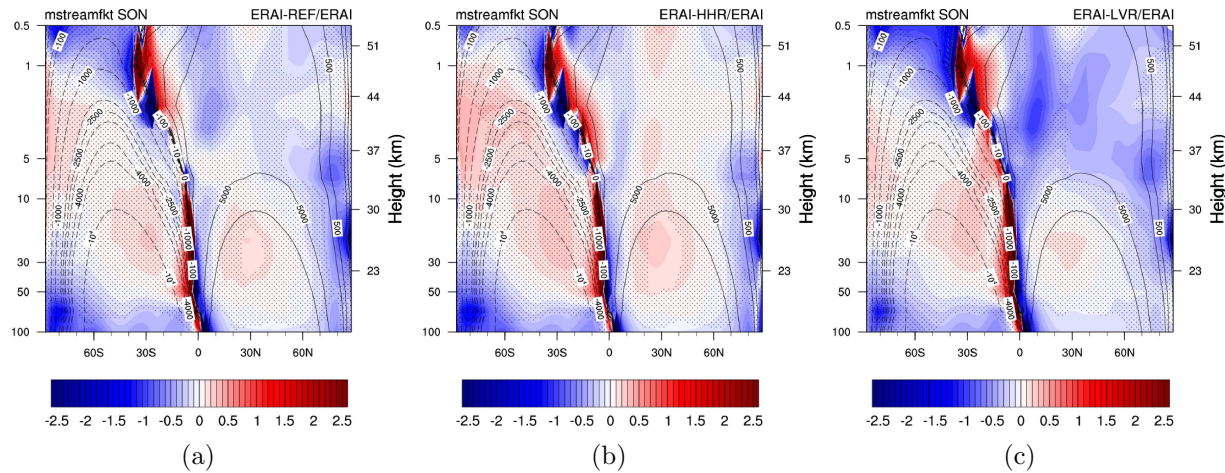


Abbildung 4.28: Same as Fig. 4.26, but for SON season.

The Southern hemispheric winter to spring transition is analysed by means of the climatological mean of the annual cycle of zonal mean wind at  $60^\circ\text{S}$ . The zonal mean wind at  $60^\circ\text{S}$  is commonly used to define the date of spring term onset (Andrews et al., 1987; Hurwitz et al., 2010; CCMVal, 2010). Strong westerlies are dominating the stratospheric wind field whereas during summer easterlies prevail. The zero-wind line denotes the spring onset, when westerlies turn into easterlies. The Fig. 4.29 gives the time-height cross section of the temporal evolution of zonal mean wind at  $60^\circ\text{S}$  of ERA-Interim and the corresponding resolution sensitivity model setup. Data are based on daily means (smoothed by a 30 day running average) derived from a time series of minimum 10 years.

Regarding the modelled zero-wind line, it becomes clear that all model configurations

suffered from a premature spring onset. The wind reversal in all models occurs faster than in the ERA-Interim data set. In the simulations with higher vertical resolution (REF and HHR) the transition from winter to spring at the middle and upper stratospheric levels takes place on average 20 days ahead of the date derived from reanalysis data. This is considerably earlier than in ERA-Interim since the inter-annual standard deviation of the onset date of spring term is about 8 days, which is comparable to the findings of CCMVal (2010). Further, easterly wind regimes in the model simulations also can reach lower altitudes than in ERA-Interim. In the REF configuration the zero-wind line spreads below the 70 hPa level whereas in the reanalysis the lowest point of the easterly regime is above 50 hPa. Similar characteristics of the zero-wind line in the LVR can be identified, however deviations here are comparatively small and are predominantly in the range of the one sigma standard deviation of ERA-Interim.

Considering now the Antarctic temperature bias of each model configuration during SON season (see Fig. 4.23), the pattern of temperature deviations agree well with the fact of a premature spring onset. The distribution of temperature anomalies in the Antarctic here resembles anomaly patterns which occur after so-called mid winter warming events, which is characterised by a temporary collapse of the polar vortex (e.g. Labitzke, 1972; Limpasuvan et al., 2012). However, in the case of the sensitivity simulations here the polar vortex breaks down permanently due to the too early migration of winter to spring conditions. Consistent with the significant Southern hemispheric temperature bias in the REF and HHR configurations the zero-wind line appears considerably earlier compared to ERA-Interim, whereas in LVR the differences of the spring onset date to the reanalysis data are within the range of the one sigma standard deviation and consequently, in accordance with this the middle atmospheric Antarctic temperature bias is statistically not relevant.

#### 4.2.7 Discussion of Resolution Sensitivities

In the previous sections the implications of model resolution on the Southern hemispheric polar vortex were analysed. The occurring effects on model dynamics can be primarily distinguished between JJA and SON season.

During Austral winter terms JJA the Antarctic temperature warm bias is qualitatively comparable in all model configurations. It is caused by an over representation of planetary wave activity, which leads to an enhanced downwelling over the Southern Polar region (represented by the mean residual circulation  $\chi^*$ ). This downwelling is associated with a considerable adiabatic warming. Equivalent causal links, such as the alterations of wave activity and their consequential implications on the large-scale background circulation are well known and described (e.g. Andrews et al., 1987; Holton et al., 2003). While the temperature bias and  $\chi^*$  give a similar picture among the model setups substantial differences arise in the characteristics of planetary waves. In particular, differences of EP-Flux divergence to ERA-Interim in the LVR simulation are considerably smaller compared to the simulations with higher vertical resolution. In a preliminary consideration this is in conflict to the detected similar differences of  $\chi^*$  and the resulting warm bias, since EP-Flux divergence is a parameter for the available momentum in order to force the meridional

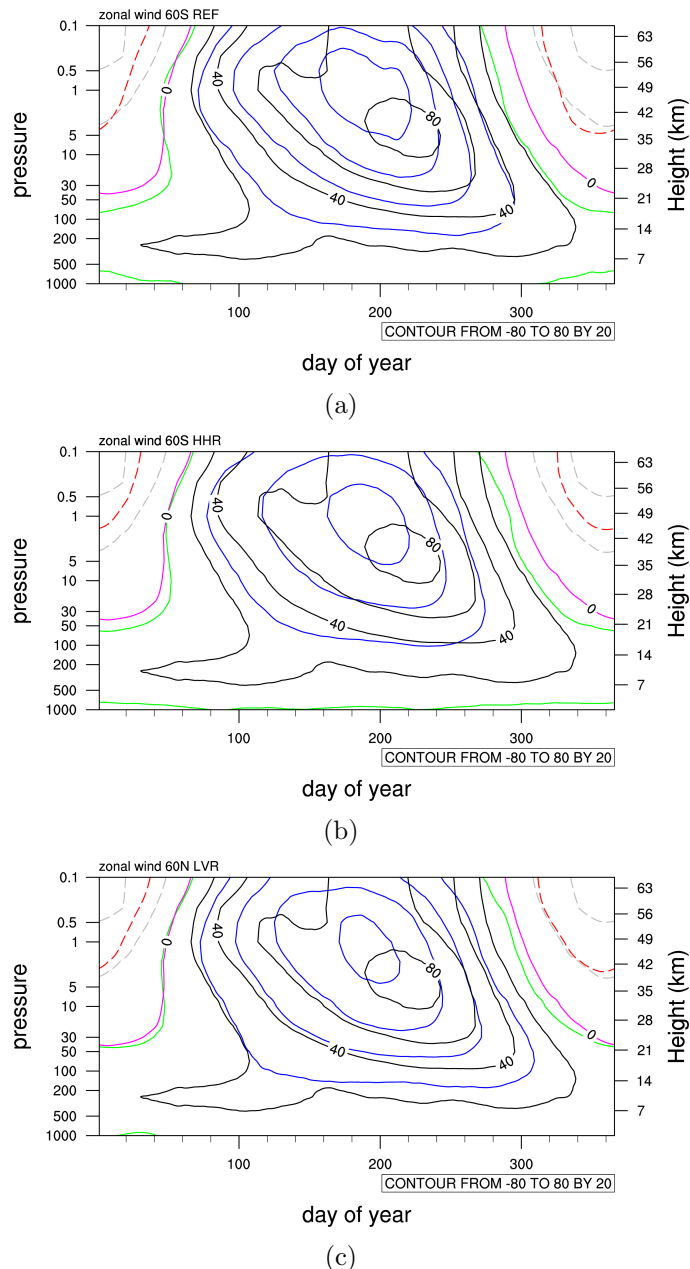


Abbildung 4.29: Time-height cross section of annual cycle of the climatological mean of zonal mean wind at 60°S given in m/s for a)REF, b)HHR and c)LVR. Blue, red and green contours refer to model data, whereas black, grey and pink contours refer to ERA-Interim. Pink and green depict the corresponding zero wind lines.

circulation. Apart from planetary waves, gravity waves can also contribute to force the large-scale circulation. Regarding the relatively strong inter-annual variability of planetary waves in LVR (which is given as the  $1\sigma$  standard deviation of  $\bar{v}'T'$ ) first indications can be constituted for an enhanced interaction of planetary waves and unresolved gravity waves. The Fig. 4.30 give the temperature tendency due to orographic gravity wave drag for the individual model configurations. It can now be determined that the effect of orographic gravity waves are the largest for the LVR simulation, in particular in regions where EP-Flux divergence anomalies are small compared to model simulations with higher vertical resolution. Since the Southern hemispheric polar warm bias is similar in all model configurations it can be concluded that the detected relatively small planetary wave activity (represented by the EP-Flux divergence) in LVR is balanced by its enhanced orographic gravity wave activity. This is in accordance with the findings in Cohen et al. (2013), where total wave activity remains constant due to compensational effects of orographic gravity waves and planetary waves.

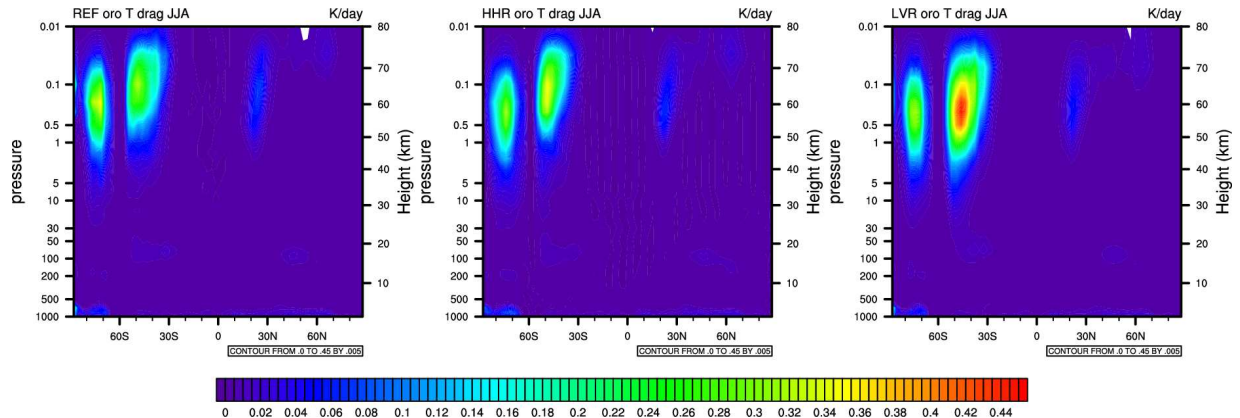


Abbildung 4.30: Climatological mean of JJA for temperature tendency due to orographic gravity wave drag in K/day. Left REF, middle HHR and right LVR.

The situation during Austral spring terms SON is different to JJA. In contrast to Austral winter the temperature bias here is not driven primarily by planetary wave activity, which is reflected by the TEM analysis. The modelled deviations from the reanalysis are predominately not significant. The Southern hemispheric temperature bias more likely arises from a premature transition of winter to spring season. The onset of spring is signified by the migration of stratospheric westerlies into easterlies, which takes place too early in each model setup. In accordance with this, models with larger deviations in the spring onset date have a stronger temperature bias, namely configurations with higher vertical resolution REF and HHR, whereas in LVR the Antarctic temperature bias is not significant and the corresponding winter to spring transition shows only small deviations to ERA-Interim within the  $1\sigma$  standard deviation.

However, the underlying processes of the early spring onset in the numerical models discussed remain unknown. There are many factors affecting polar vortex persistence and

thus spring onset. Some studies have explored the relationship between polar vortex dynamics and chemistry. In particular it could be shown that planetary wave activity is linearly correlated to polar ozone (Weber et al., 2011) and thus, a misrepresentation of this species in the models could have spurious implications on the dynamics. The ozone chemistry however, is prescribed in all model simulations here considering observational data sets and hence, uncertainties concerning interactions between the dynamics and ozone chemistry can be assumed to be comparatively small.

Another branch of research interest has focused on the role of atmospheric wave driving (planetary as well as gravity waves) on the breakup of the polar vortices. It is demonstrated that planetary waves play a considerable role in the breakup of the Southern hemispheric polar vortex. Particularly it is demonstrated that the timing of the maximum  $\overline{v'T'}$  is important for a qualitatively well representation of the spring onset date (Hurwitz et al., 2010). However, the simulations presented here show a maximum  $\overline{v'T'}$  which is shifted by one month ahead compared to reanalysis data. This shift probably has implications on the modelled spring onset. Apart from planetary waves momentum deposition by unresolved gravity waves can also weaken the polar jets and initialise breakup of the polar vortices in spring (e.g. Limpasuvan et al., 2007). Furthermore recent studies also showed strong interaction between planetary and unresolved gravity waves (Cohen et al., 2013, 2014). Relations between planetary waves and orographic gravity waves could also be detected in the model simulations here and the wrong timing of  $\overline{v'T'}$  could be a result from these interactions. Nonetheless, the exact underlying processes which determine the effects of gravity waves on planetary waves (and vice versa) are still unclear and are subject of current research (Fritts and Alexander, 2003; Cohen et al., 2014).



# Kapitel 5

## Summary and Conclusions

The need for reliable information on the climate system at time scales of up to a decade is an ever growing demand. MiKlip provides initial sets of simulations that consider the needs of decadal climate predictions. However, in general the progress made by numerical model systems in order to meet the requirements for decadal climate predictions remain at an early stage of development and many challenges occur.

This thesis contributes to the knowledge production with regard to the role of the stratosphere on decadal time scales. In particular the understanding and representation of the variability induced by dynamical processes are essential points.

### **How to describe atmospheric variability on intra-decadal time scales and what are the relevant processes?**

One task was the characterisation of atmospheric variability on intra-decadal time scales. Variability is a key parameter for the description of atmospheric dynamics. A new approach to the analysis of intra-decadal variability is presented. Therefore, the methodology and theoretical considerations of the well known and tested intra-seasonal power spectra analysis (Hayashi, 1971) are adapted to a decadal time horizon.

External / deterministic variability such as QBO and ENSO can be detected and predominately contribute to the power spectra for periods larger than 12 months. For example, the QBO can partly be responsible for 80% of total variability for time scales of about 24 months. Contrarily, chaotic / internal variability which can be caused by interaction between waves and the atmospheric background field dominates the variability patterns on time scales shorter than 12 months. Especially, at the stratospheric level, the larger values of variability contributed by internal variability are highly likely to be related to processes concerning the dynamics of polar vortices, since the dynamical properties of the polar winter vortices are characterised by the interaction of atmospheric waves with the background mean flow. A further prominent feature of decadal PSA arises at the 12 month period, representing the annual cycle.

One weakness of the here presented analysis is the lacking statistical significance. However, by means of the a multiple linear regression (MLR) model certain fractions of the

power spectra could be distinctly attributed to certain atmospheric processes. For example the relatively large power at the 24 months period at stratospheric levels clearly can be assigned to effects of the QBO; or the high variability structures in stratospheric polar regions occurring in the decadal PSA attributed to the polar vortices. This gives more confidence distinguishing between relevant and non-relevant structures in the variability pattern. Furthermore, strong deviations of the decadal power spectra between the models and reanalysis data occur predominantly in regions where the MLR analysis can clearly attribute variability to certain atmospheric processes. In particular, the detected large differences in the power spectrum for the atmospheric features like the QBO and the Southern hemispheric polar vortex are in line with previous studies, which demonstrated shortcomings of the regarded model systems in simulating QBO or the Antarctic polar night jet (e.g. Giorgetta et al., 2002; Deckert, 2012; Khosrawi et al., 2009). Therefore this new approach applying the power spectral analysis on decadal time scales lead to useful and reasonable results.

**What are the challenges numerical models are faced with decadal variability and what are the causes and drivers of model shortcomings reflecting-intra decadal variability?**

Regarding the analysed simulations of the numerical model systems MiKlip and EMAC clear deviations with respect to ERA-Interim arises in the decadal power spectra. In stratospheric levels this is most pronounced in the tropical region around the 24 months period and as well as in the polar regions with periods shorter than 12 months differences are comparatively large. Model simulations here can overestimate variability by 30% of the values detected for the reanalysis data.

The detected modeled shortcomings in the decadal PSA give rise to the assumption that the underlying causes mainly can be found on intra-seasonal time scales. For this reason analysis of intra-seasonal time scales were conducted.

### Tropical Variability

For example tropical variability depicted by the QBO is known to be forced by Kelvin and Mixed-Rossby-Gravity (MRG) waves. These waves typically have a time horizon shorter than a season (Holton and Hakim, 2013). Conduction of a power spectral analysis gives rise that problems occurring in the representation of simulated QBO can largely be attributed to issues related to the MRG waves. Calling in, linear wave theory it becomes apparent that in the case of low vertical resolution configuration, a considerable amount of MRG wave cannot be resolved and therefore necessary momentum to force the QBO is missing. The findings here reveal a minimum vertical resolution of at least 1 km in order to resolve the required wave spectra. This is in accordance to numerical experiment of Giorgetta et al. (2006), who found out by varying the vertical resolution of numerical models that the QBO is solely generated if vertical resolution is higher than 1 km.

Extending analysis of tropical variability in the vertical up to mesospheric levels, a

further leading variability pattern of the middle atmosphere arises, the SAO. All regarded model systems in this thesis can qualitatively capture the characteristics of the SAO. Bearing in mind the strong influence of QBO on the SAO (e.g. the QBO significantly alters the spectra of vertical propagating waves which is available to drive the SAO (Mayr et al., 2010), it is not surprising that models with a qualitative good representation of the QBO also reflect a qualitative good pattern of the SAO. In contrast the low vertical resolution model LR where no QBO was detected, a relatively strong SAO signature occurs. This is due to the fact that the driving mechanisms of the SAO, are overestimated in the LR model, i.e. PSA has been shown that the contribution of planetary waves is enhanced compared to the reanalysis data and therefore available momentum to force the SAO is overestimated.

In the context of numerical decadal prediction systems the results of tropical intra-seasonal variability clearly show the need for a well resolved vertical structure of middle atmosphere. Models with a high vertical resolution (resolving vertical structures up to 1 km) are superior to low vertical resolution models due to the fact that essential processes accounting for tropical variability cannot be captured correctly by a low vertical resolution. Therefore, numerical model predictions spanning a time scales of a decade, need to consider a high vertical resolved representation of the atmosphere in order to provide the 'technical boundary conditions' reproducing the required variability, particularly in the equatorial region.

As stated above, apart from the tropics the decadal PSA shows challenges of the numerical models which are reflected in the representation of the variability in the polar stratospheric regions. Obvious deviations of the models to ERA-Interim can reach up to 30% of the values of the reanalysis data and are predominantly located at periods on intra-annual time scale shorter than 12 months. The MLR analysis could attribute these differences of decadal PSA to internal variability, which is characterised by interactions of atmospheric waves and the background mean flow. Prominent atmospheric feature of the high-latitudes are the polar vortices. They are known to be sensitive to the effects of internal variability (e.g. Holton and Hakim, 2013; Andrews et al., 1987). Hence, the detected differences of decadal PSA are related to the polar vortices.

## Southern Polar Variability

In particular, previous studies (e.g. Khosrawi et al., 2009; Deckert, 2012; Righi et al., 2014) have demonstrated that the underlying numerical models of the here regarded simulations suffer from a too weak Southern hemispheric polar vortex. Notably Deckert (2012) demonstrated that EMAC as well as ECHAM6 (the model component of MiKlip hosting atmospheric processes) significantly underestimate zonal wind speed of Antarctic polar vortex during Austral winter season JJA, which results in a warm bias of stratospheric temperatures and thus the Southern hemispheric polar night jet arising in the models are too weak. Concerning the Northern hemispheric polar vortex, differences to reanalysis data set of polar stratospheric zonal wind speed are relatively small, and deviations are predominantly statistically not significant (Righi et al., 2014 and personal communication by

Deckert). Therefore, analyses in this thesis are concentrated on the Southern hemispheric phenomenon.

In order to investigate the causes of the too weak Southern hemispheric polar vortex in more detail, sensitivity studies with EMAC were carried out. The advantage of EMAC is its modular structure which allows a fast and efficient implementation of sensitivity simulations. Furthermore EMAC and MiKlip utilise a related atmospheric base model and essential parameterisations such as the non-orographic gravity wave parameterisation or the treatment of convection are consistent in both numerical model systems. Therefore findings gain with EMAC simulations can qualitatively adapted to MiKlip decadal prediction model system.

The conducted sensitivity studies are structured in three categories constituting a systematic research into the causes of model deficits representing the Southern hemispheric polar vortex.

### SST sensitivity studies

Based on the studies of Deckert (2012), who detected a correlation between enhanced planetary wave activity and a too weak Austral winter polar vortex in the EMAC model simulations, a first set of SST sensitivity simulations are conducted. SSTs are known to have implications on planetary wave activity (e.g. Garny et al., 2009; Garny, 2010; Cai et al., 2012) as so three sensitivity studies were performed. Each of them utilising a different prescribed SST data set. The main findings are:

- Independent from chosen SST data set, the main characteristics of model bias concerning the Southern hemispheric polar vortex (such as too high polar temperatures and too slow zonal mean winds) remain unaffected.
- The simulated tropospheric planetary wave activity entering the stratosphere, considered as  $\bar{v' T'}$  is distinctly overestimated during Austral winter season. However, its absolute values and annual evolution are clearly distinguishable between the particular sensitivity simulations.
- The slopes of the corresponding regression lines derived from the Newman-correlation indicates a general model problem with the representation of gravity waves, which contributes to the model bias.

### Gravity Wave Sensitivity Studies

As presented in Austin et al. (2003), the calculated Newman-correlations can vary in a wide range among different numerical models. Following the argumentation of Shepherd (2006) this large variability is a result of the different treatment of non-resolved gravity waves in the models. With regard to the SST sensitivity studies, deviations of the Newman-correlation to reanalysis data sets suggest problems in the gravity wave parameterisation. The second category of sensitivity studies investigates the effects of the non-orographic parameterisation. The main results can be concluded as follows:

- With increasing non-orographic gravity wave activity, model biases regarding Southern hemispheric polar vortex intensifies.
- The intensification of model bias in stratospheric levels during JJA is correlated to an enhanced planetary wave activity.
- During SON season model bias cannot be explained by atmospheric wave activity. Neither planetary waves nor gravity waves can be attributed to the detected model bias.

### Resolution Sensitivity Studies

The third set of sensitivity studies comprises the investigation of model resolution on model dynamics. Previous studies demonstrated that the contribution of gravity waves could be enhanced by an increased horizontal model resolution (Hayashi et al., 1989; Hamilton, 1996) and also planetary wave activity can be significantly be affected by vertical as well as horizontal model resolution (Roeckner et al., 2006). Sensitivity studies are carried out altering horizontal and vertical resolution, respectively. The resulting findings are summarised:

- TEM diagnostics can now demonstrate that model bias during JJA emerges from an overestimated wave activity (predominantly planetary wave activity), which leads to an enhanced downwelling over Southern hemispheric polar region accompanied by an exaggerated polar warming.
- The higher horizontal resolution model shows similar characteristics to experiments with enhanced gravity wave activity, which is in accordance to the afore mentioned studies.
- The low resolution model offers a relatively small model bias regarding planetary wave activity. However, in particular during JJA this circumstance is compensated by an enlarged gravity wave, resulting in an overestimated total wave activity.
- Model bias in the SON season is a consequence of a premature spring on set of all model configurations. Nonetheless the underlying drivers remain unclear.

Southern hemispheric polar vortex hosts a large fraction of variability and therefore decadal prediction system, such as MiKlip need to be able to give a good representation of this atmospheric feature. The conducted sensitivity studies help to shed more light on the problem, which model simulations have with the description of Austral winter polar vortex. With respect to the here obtained findings interaction of planetary waves and gravity waves but also gravity waves themselves have great implications on representation of simulated Southern hemispheric polar vortex. The small-scale gravity waves however, are largely not resolved by the model system and thus have to be parameterised. With this parameterisation several challenges emerge. For example gravity waves are constrained by

a lack of observations and therefore the numerical models are faced with an undesirably large degree of freedom (Fritts and Alexander, 2003). Further the implications of gravity waves on planetary waves and vice versa are very recently discussed and first possible driving mechanisms are suggested (Cohen et al., 2013, 2014).

In general the decadal prediction system MiKlip would benefit from a refinement of the gravity wave parameterisation. Therefore a larger number of observations are required in order to obtain a reliable gravity wave spectrum. Recent measurement campaigns such as DEEPWAVE (Deep Propagating Gravity Wave Experiment over New Zealand) are a first step to contribute to such an observational data basement, but many more, in particular worldwide as well as long term continuing measurements are needed.

From a global model perspective, the simulation quality would take advantage from a more robust observational constraint of the source spectra (which describe the initial state of gravity wave spectra at the launch level), i.e. it is shown that rather the properties of the source spectra plays a larger role on the GCM response, than the specifics of the implemented gravity wave dissipation (McLandress and Scinocca, 2005).

## Outlook

Due to statistical relevance, in this work analysis concentrates on the tropical and Southern polar regions. However, decadal PSA and the TEM diagnostic give some indications for distinct difficulties of the numerical models representing the Northern polar vortex. The determined lacking statistical significance could be a consequence from the high inter-annual variability, which complicate the identification of robust signals in Northern hemisphere (Holton et al., 2003). One possibility to tackle this problem is the extension of simulated years. So future work with focal points on the Northern hemispheric polar vortex need to conduct longer time-series in order to obtain a larger data fundament, which is mandatory to extract statistically robust signals.

Another point, which needs further clarification is an issue related to reanalysis data. In this work predominantly ERA-Interim is utilised as a reference data set in order to validate numerical simulation results. One advantage of this data set is the longterm experience. Many problems of this ERA-Interim could be identified and are documented (e.g. Dee et al., 2011).

Apart from ERA-Interim a couple of other current reanalysis data sets are in use by the scientific community. For middle atmospheric studies, in particular at upper stratospheric and mesospheric levels the usage of current reanalysis data sets are subject of uncertainties. Among other things, this is due to the fact that the individual reanalysis data sets show an increasing disagreement between each other, when upper stratospheric and mesospheric levels are regarded (Mitchell et al., 2014). Research efforts to understand the causes of these differences among the various reanalysis data sets are just evolving, and intercomparison activity regarding the middle atmospheric processes of the individual reanalysis data set have been started in the recent years (Fujiwara and Jackson, 2013).

The here introduced method of decadal PSA can be utilised to analyse the internal as well as external variability of the individual reanalysis data set; and the resulting findings

could contribute to a better understanding of the arising differences among the respective reanalysis data.

To conclude, this work is a further contribution, which documents and highlights the importance of the stratosphere in the context of the Earth system. The Earth system is commonly considered as the combinations of atmosphere, ocean, cryosphere and biosphere, whereby the atmosphere in this case is often refer to the troposphere only. However, following the knowledge production of this thesis my personal opinion is that the 4 categories of the Earth system have to be extended by a fifth one, namely the stratosphere. In particular, when regarding decadal climate prediction, the stratosphere and its variability plays a significant role and therefore relevant processes need to be considered in an adequate manner.



# Anhang A

## Methods of Power Spectral Analysis (PSA)

### A.1 Hayashi Method

The Power Spectral Analysis (PSA) provides information of a certain process by means of wavelength and frequency. The first theoretical concepts were provided by Deland (1964) and Kao (1968, 1970). Hayashi (1979), Hayashi (1982) and Pratt (1976) adapted their methods by taking into consideration of the stochastic nature of the analysed wave fields. In the following a very brief description of Hayashi's Method is given.

Let us consider  $w(x, t)$  as a space-time dependent process on a longitudinal circle ( $x$ ) and limited in time ( $0 < t < T$ ). Then

$$\begin{aligned} w(x, t) &= \sum_k F_k(t) e^{ikt} \\ &= \sum_k [C_k(t) - iS_k(t)] e^{ikx}, \end{aligned} \tag{A.1}$$

and

$$\begin{aligned} \hat{w}_{k,\omega} &= \frac{1}{T} \int_0^T F_k(t) - e^{i\omega t} dt \\ &= \hat{F}_k/2 \\ &= [\hat{C}_k - i\hat{S}_k]/2. \end{aligned} \tag{A.2}$$

The  $\hat{w}_{k,\omega}$  is the complex space-time transformed.  $F_k(t)$  is the space complex Fourier coefficient and  $\hat{F}_k(t)$  is its time complex Fourier transform. The  $C_k$  and  $S_k$  are the corresponding cosine and sine coefficients and  $\hat{C}_k$  and  $\hat{S}_k$ , respectively. Here, the positive and negative frequencies correspond to westward and eastward phase velocity.

The power spectra  $P_{k,\omega}$  is defined as the variance of the space time coefficient  $\hat{w}$ , which is given as

$$P_{k,\omega}(w) = \frac{1}{2} \langle |\hat{w}_{k,\omega}|^2 \rangle, \quad (\text{A.3})$$

After insertion of A.2 in A.3 gives following formula.

$$\begin{aligned} 4P_{k,\pm\omega}(w) &= P_{k,\pm\omega}(\hat{F}_k) \\ &= P_\omega(\hat{C}_k) + P_\omega(\hat{S}_k) \pm 2Q_\omega(\hat{C}_k, \hat{S}_k), \end{aligned} \quad (\text{A.4})$$

$P$  and  $Q$  are the power and quadrature spectral densities. Now it is clear that power spectra of eastward  $H_E$  and westward  $H_W$  propagating waves can be inferred from the sign of the quadrature spectra.

$$\begin{aligned} H_E(k, \omega) &= P_\omega(\hat{C}_k) + P_\omega(\hat{S}_k) + 2Q_\omega(\hat{C}_k, \hat{S}_k), \\ H_W(k, \omega) &= P_\omega(\hat{C}_k) + P_\omega(\hat{S}_k) - 2Q_\omega(\hat{C}_k, \hat{S}_k). \end{aligned} \quad (\text{A.5})$$

The total variance  $H_T$  is the sum of eastward and westward contributions and is given as

$$H_T(k, \omega) = [P_\omega(\hat{C}_k) + P_\omega(\hat{S}_k)]/2. \quad (\text{A.6})$$

So total variance provides very detailed information of the contribution of the individual waves, dependent on their wavelenghts and frequencies and thus Hayashi's method presents a powerful tool in order to identify the characteristic of variability.

In this work Hayashi PSA is displayed dependent on the period with a logarithmic scale. In order to illustrate the power distribution correctly the power has to be scaled by frequency (Zangvil, 1977). The reason for this is to preserve area fidelity.

## A.2 Wheeler Method

The QBO is driven by equatorial Kelvin and Mixed-Rossby-Gravity waves. A method to illustrate such equatorial waves was presented by Wheeler and Kiladis (1999). This method makes use of a symmetric and antisymmetric decomposition of the atmospheric field (e.g. temperature, zonal wind), which is a function of latitude  $\phi$ . So the atmospheric field  $A$  can be written as:

$$A(\phi) = A_{sym}(\phi) + A_{asym}(\phi), \quad (\text{A.7})$$

where the asymmetric component is given as

$$A_{asym}(\phi) = [A(\phi) - A(-\phi)]/2, \quad (\text{A.8})$$

and the symmetric component respectively

$$A_{sym}(\phi) = [A(\phi) + A(-\phi)]/2, \quad (\text{A.9})$$

In this work only the latitude around the equator from  $15^{\circ}\text{N}$  to  $15^{\circ}\text{S}$  are taken into account and their discrete Fourier transformed are calculated. The Fourier transformed are two dimensional, since the decomposed fields are considered to be determined at  $M$  equally spaced points around a latitude circle given as  $x_M$  and  $N$  equally spaced points in time given as  $t_n$  respectively. Thus the space-time Fourier transformed of the decomposed field  $f(t_n, x_m)$  can be written :

$$F(k, \omega) = \frac{1}{M} \sum_{m=1}^M \frac{1}{N} \sum_{n=1}^N f(x_m, t_n) \exp[i(kx_m - \omega t_n)], \quad (\text{A.10})$$

For the power  $P$  it follows:

$$P(k, \omega) = F^* F, \quad (\text{A.11})$$

where the asterix denotes the complex conjugate and  $-1 = \sqrt{i}$ . To plot the Wheeler PSA no scaling is applied, since linear axes were utilised.



## Anhang B

# Linear Least Square Regression Model

The different drivers of variability in geophysical processes can be analysed by the use of regression models. In this work implications of QBO or ENSO on the zonal wind field are diagnosed in order to estimate their contributions to the power spectra. Theory and method of the applied linear least square regression model is described here.

Let  $y(t)$  be a time-series of a quantity which is assumed to be represented by one or more independent processes. The most simple assumption is that the relation between  $y(t)$  and these processes are linear. Then  $y(t)$  can be written as (Von Storch and Zwiers, 2001):

$$y(t_i) = \sum_{k=1}^M a_k x_k(t_i) + r(t_i), \quad (i = 1 \dots N) \quad (\text{B.1})$$

where  $a_k$  are the so called regression coefficients and  $x_k$  are the basis functions representing processes that are believed to play a role in the variability of  $y(t)$ .  $M$  is the number of basis function and  $N$  is the length of the time-series. The difference between the calculated quantity (derived from regression coefficients and base functions) and the initially 'observed' quantity is denoted in the residual term  $r(t)$ . Linearity is accounted for regression coefficients  $a_k$  and not necessary for the basis functions. Equation B.1 can be given in matrix form as:

$$\mathbf{y} = \mathbf{X}\mathbf{a} + \mathbf{r}. \quad (\text{B.2})$$

Here  $X$  a  $N \times M$  matrix is called the 'design-matrix', which contains the basis functions at time  $t_i$  as  $k$ th column. The time dependent quantities  $y(t)$  and  $r(t)$  are expressed as vectors  $\mathbf{y}$  and  $\mathbf{r}$  with the length  $N$ . The vector  $\mathbf{a}$  is built by the  $M$  coefficients  $a_k$ . To determine the parameters  $a_k$ , the sum of the squared residuals ( $\chi^2$ ) has to be minimised.  $\chi^2$  can be written as:

$$\begin{aligned} \chi^2 &= \mathbf{r}^T \mathbf{r} \\ &= (\mathbf{y} - \mathbf{X}\mathbf{a})^T (\mathbf{y} - \mathbf{X}\mathbf{a}) \\ &= \mathbf{y}^T \mathbf{y} - 2(\mathbf{X}^T \mathbf{y})^T \mathbf{a} - \mathbf{a}^T \mathbf{X}^T \mathbf{X} \mathbf{a}. \end{aligned} \quad (\text{B.3})$$

The partial derivative of  $\chi^2$  according to  $\mathbf{a}$  is set to be zero, yielding

$$2(X^T \mathbf{y} + X^T X \mathbf{a}) = 0. \quad (\text{B.4})$$

The solution of B.4 gives the sought coefficients  $\mathbf{a}$ . Now the modeled quantity is expressed by  $y_m = \mathbf{X}\mathbf{a}$ . Further details of the theory can be found in Garny (2010).

The regression model in this work is formulated as follows:

$$\begin{aligned} y_m(\phi, t) = & a_1(\phi, t) + \\ & a_2(\phi, t) \cdot \text{Trend}(t) + \\ & a_3(\phi, t) \cdot \text{QBO}(t + \Delta t) + \\ & a_4(\phi, t) \cdot \text{Solar}(t) + \\ & a_5(\phi, t) \cdot \text{ENSO}(t), \end{aligned} \quad (\text{B.5})$$

where  $\phi$  is latitude,  $t$  is given in a monthly time step and  $y_m(\phi, t)$  is the calculated zonal wind field. As base functions the mean annual cycle, the trend, the QBO, the solar cycle and ENSO were included. The trend is realised as the least squares linear trend of the time series. The QBO is the mean zonal wind in the tropics ( $15^\circ\text{N}$  to  $15^\circ\text{S}$ ) at 50 hPa. The  $\Delta t$  accounts for the possible different wind regimes occurring at different altitudes during a QBO phase. Technically an additionally QBO term is implemented, which is orthogonal in time to the original one. The base function for the solar cycle is derived as the 10.7 cm solar irradiance time series provided by CCMVal and ENSO is the NINO3.4 index from NOAA. In order to account for the seasonal variability, a Fourier expansion of all fit coefficients  $a_i$  is applied:

$$\begin{aligned} a_i(\phi, t) = & a_{i0}(\phi) + \sum_{k=1}^M [a_{ik}s(\phi)\sin(2\pi k(t - 0.5)/12) + \\ & a_{ikc}(\phi)\cos(2\pi k(t - 0.5)/12)]. \end{aligned} \quad (\text{B.6})$$

In this work  $N$  is set to 4 for the constant term  $a_1$ , and for the remaining coefficients it is set to 2. The setting of  $N$  equal to 4 for the constant term allows for accurate representation of the annual cycle which is simply the Fourier expansion of the constant term, whereas restricting  $N$  to 2 for the other terms allows for a more explicit annual and semi-annual variability in the coefficients without over-fitting the regression model.

## Anhang C

# The Transformed Eulerian Mean (TEM) Framework

In order to investigate the global mean circulation of middle atmosphere the concept of the Transformed Eulerian Mean (TEM) equations are briefly introduced. The foundation of this theory is laid in the following problem: the mean meridional circulation described by the conventional Eulerian Mean sets of equations is cancelled out by motions induced by non-dissipative waves. This fact is also named the Eliassen-Palm theorem or the Non-transport theorem (Andrews and McIntyre, 1976; Andrews et al., 1987). To consider implications of eddy induced forces to the mean circulation it is convenient to transform the Eulerian meridional circulation equations to an alternative form, namely the TEM equations.

First a residual meridional mean circulation is defined with a meridional component:

$$\bar{v}^* = \bar{v} - \frac{\partial}{\partial p} \left( \bar{v}' \theta' / \frac{\partial \theta_0}{\partial p} \right) \quad (C.1)$$

and a vertical component:

$$\bar{w}^* = \bar{w} + \frac{1}{r \cos \phi} \frac{\partial}{\partial \phi} \left( \bar{v}' \theta' / \frac{\partial \theta_0}{\partial p} \right). \quad (C.2)$$

Here  $v, w$  are the wind velocities in meridional and vertical direction, respectively. The potential temperature is given as  $\theta$ ,  $r$  is the Earth's radius,  $p$  is the pressure and  $\phi$  is latitude. With this definition the TEM equations can now be obtained:

$$\frac{\partial \bar{u}}{\partial t} + \hat{f} \bar{v}^* + \bar{w}^* \frac{\partial \bar{u}}{\partial p} = \bar{X} + \frac{1}{r \cos \phi} \nabla \cdot F, \quad (C.3)$$

$$\frac{\partial \bar{\theta}}{\partial t} + \frac{\partial \bar{\theta}_0}{\partial p} \bar{w}^* = \bar{Q}, \quad (C.4)$$

$$\frac{1}{r \cos \phi} \frac{\partial \bar{v}^* \cos \phi}{\partial \phi} + \frac{\partial \bar{w}^*}{\partial p} = 0, \quad (C.5)$$

with  $\hat{f} = f - 1/(rcos\phi)\frac{\partial}{\partial\phi}(\bar{u}cos\phi)$ ,  $\bar{X}$  is a forcing term representing small scale eddies (e.g. gravity waves forcing),  $\bar{Q}$  diabatic heating term and  $\nabla \cdot F$  denotes the divergence of the EP-Flux  $F$ , which are defined as:

$$\nabla \cdot F = \frac{1}{rcos\phi} \frac{d}{d\phi} (F_\phi cos\phi) + \frac{d}{dp} F_p, \quad (\text{C.6})$$

with

$$F_\phi = rcos\phi \left( -\bar{u}'v' + \bar{v}'\theta' / \theta_p \frac{du}{dp} \right), \quad (\text{C.7})$$

and

$$F_p = rcos\phi \left( (f - \frac{du}{d\phi}) \bar{v}'\theta' / \theta_p - \bar{u}'w' \right). \quad (\text{C.8})$$

$F_\phi$  and  $F_p$  give the meridional and vertical direction of planetary wave activity, and it divergence reflects the forcing on the mean flow by dissipating waves. For a correct illustration of EP-Flux, scaling have to be applied (Edmon et al., 1980). In this work EP-Fluxes are scaled following the conventions provided by the American National Oceanic and Atmospheric Administration, which generally follows the procedure described in Edmon et al. (1980). Therefore the above given EP-Flux is recalculated to:

$$\hat{F}_\phi = 2\pi rcos\phi / g \cdot F_\phi, \quad (\text{C.9})$$

$$\hat{F}_p = 2\pi r^2 cos\phi / g \cdot \sqrt{\frac{p_0}{p}} \cdot F_p. \quad (\text{C.10})$$

Additionally scaling in the vertical is allowed to enhance visibility of the vectors in the middle atmospheric levels. All vectors above 100 hPa are multiplied by a scale factor 5 (This method is commonly adopted, e. g. Bunzel (2013)). Due to the mass scaling, the units of the EP-Flux is given as  $[m^3 rad, m^3 Pa]$  and the divergence in  $m/s/day$  (Edmon et al., 1980).

Large scale stratospheric circulation can be quantified by analysing the residual mean circulation  $(\bar{v}^*, \bar{w}^*)$ . Considering the continuity equation for  $(\bar{v}^*, \bar{w}^*)$ , the mass-weighted residual streamfunctions  $\bar{\chi}^*$  can be obtained:

$$(\bar{v}^*, \bar{w}^*) = \frac{g}{2\pi rcos\phi} \left( -\frac{\partial \bar{\chi}^*}{\partial p}, \frac{1}{r} \frac{\partial \bar{\chi}^*}{\partial \phi} \right), \quad (\text{C.11})$$

which can be rewritten as:

$$\bar{\chi}^*(\phi, p) = \int_{\phi'=90^\circ}^{\phi} \frac{2\pi r^2 cos\phi'}{g} \bar{w}^*(\phi', p) d\phi'. \quad (\text{C.12})$$

So residual mean meridional circulation can be calculated from the residual vertical velocity.

# Literaturverzeichnis

Akiyoshi, H., Zhou, L., Yamashita, Y., Sakamoto, K., Yoshiki, M., Nagashima, T., Takahashi, M., Kurokawa, J., Takigawa, M., and Imamura, T. (2009). A CCM simulation of the breakup of the Antarctic polar vortex in the years 1980–2004 under the CCMVal scenarios. *Journal of Geophysical Research: Atmospheres (1984–2012)*, 114(D3).

Andrews, D. and McIntyre, M. E. (1976). Planetary waves in horizontal and vertical shear: The generalized Eliassen-Palm relation and the mean zonal acceleration. *Journal of the Atmospheric Sciences*, 33(11):2031–2048.

Andrews, D. G., Holton, J. R., and Leovy, C. B. (1987). *Middle atmosphere dynamics*. Number 40. Academic press.

Austin, J., Shindell, D., Beagley, S., Brühl, C., Dameris, M., Manzini, E., Nagashima, T., Newman, P., Pawson, S., Pitari, G., et al. (2003). Uncertainties and assessments of chemistry-climate models of the stratosphere. *Atmospheric Chemistry and Physics*, 3(1):1–27.

Baldwin, M. P. and Dunkerton, T. J. (2001). Stratospheric harbingers of anomalous weather regimes. *Science*, 294(5542):581–584.

Baldwin, M. P. and Gray, L. J. (2005). Tropical stratospheric zonal winds in ECMWF ERA-40 reanalysis, rocketsonde data, and rawinsonde data. *Geophysical Research Letters*, 32(9).

Balmaseda, M. A., Mogensen, K., and Weaver, A. T. (2013). Evaluation of the ECMWF ocean reanalysis system ORAS4. *Quarterly Journal of the Royal Meteorological Society*, 139(674):1132–1161.

Boville, B. A. (1984). The influence of the polar night jet on the tropospheric circulation in a GCM. *Journal of the Atmospheric Sciences*, 41(7):1132–1142.

Boville, B. A. and Randel, W. J. (1992). Equatorial waves in a stratospheric GCM: Effects of vertical resolution. *Journal of the Atmospheric Sciences*, 49(9):785–801.

Bunzel, F. (2013). *Numerical studies of stratosphere–troposphere dynamical coupling in a changing climate*. PhD thesis, University of Hamburg.

Cagnazzo, C., Manzini, E., Calvo, N., Douglass, A., Akiyoshi, H., Bekki, S., Chipperfield, M., Dameris, M., Deushi, M., Fischer, A., et al. (2009). Northern winter stratospheric temperature and ozone responses to ENSO inferred from an ensemble of Chemistry Climate Models. *Atmospheric Chemistry and Physics*, 9(22):8935–8948.

Cai, D., Dameris, M., Garny, H., and Runde, T. (2012). Implications of all season Arctic sea-ice anomalies on the stratosphere. *Atmospheric Chemistry and Physics*, 12(24):11819–11831.

CCMVal, S. (2010). SPARC Report on the Evaluation of Chemistry-Climate Models, edited by: Eyring, V., Shepherd, T.G., and Waugh, D.W. Technical report, SPARC Report.

Charney, J. G. and Drazin, P. G. (1961). Propagation of planetary-scale disturbances from the lower into the upper atmosphere. *Journal of Geophysical Research*, 66(1):83–109.

Cohen, N. Y., Gerber, E., and Oliver Bühler, E. P. (2013). Compensation between resolved and unresolved wave driving in the stratosphere: Implications for downward control. *Journal of the Atmospheric Sciences*, 70(12):3780–3798.

Cohen, N. Y., Gerber, E. P., and Bühler, O. (2014). What Drives the Brewer–Dobson Circulation? *Journal of the Atmospheric Sciences*, 71(10):3837–3855.

Courtier, P., Thépaut, J.-N., and Hollingsworth, A. (1994). A strategy for operational implementation of 4D-Var, using an incremental approach. *Quarterly Journal of the Royal Meteorological Society*, 120(519):1367–1387.

Dameris, M. and Ebel, A. (1990). The quasi-biennial oscillation and major stratospheric warmings-A three-dimensional model study. *Annales Geophysicae*, 8:79–85.

Dameris, M., Matthes, S., Deckert, R., Grewe, V., and Ponater, M. (2006). Solar cycle effect delays onset of ozone recovery. *Geophysical Research Letters*, 33(3):L03806.

Dameris, M., Peter, T., Schmidt, U., and Zellner, R. (2007). Das Ozonloch und seine Ursachen. *Chemie in unserer Zeit*, 41(3):152–168.

Deckert, R. (2012). Why no antarctic polar vortex in echam5? 3rd International Conference on Earth System Modelling (3ICESM), Hamburg, Germany.

Dee, D. and Uppala, S. (2008). *Variational bias correction in ERA-Interim*. ECMWF, Technical Memoranda.

Dee, D., Uppala, S., Simmons, A., Berrisford, P., Poli, P., Kobayashi, S., Andrae, U., Balmaseda, M., Balsamo, G., Bauer, P., et al. (2011). The ERA-Interim reanalysis: Configuration and performance of the data assimilation system. *Quarterly Journal of the Royal Meteorological Society*, 137(656):553–597.

Deland, R. J. (1964). Travelling planetary waves. *Tellus*, 16(2):271–273.

Dell'Aquila, A., Lucarini, V., Ruti, P. M., and Calmanti, S. (2005). Hayashi spectra of the northern hemisphere mid-latitude atmospheric variability in the NCEP–NCAR and ECMWF reanalyses. *Climate Dynamics*, 25(6):639–652.

Dickinson, R. E. (1968). Planetary Rossby waves propagating vertically through weak westerly wind wave guides. *Journal of the Atmospheric Sciences*, 25(6):984–1002.

Dunkerton, T. J. (1982). Theory of the mesopause semiannual oscillation. *Journal of the Atmospheric Sciences*, 39(12):2681–2690.

Dunkerton, T. J. (1997). The role of gravity waves in the quasi-biennial oscillation. *Journal of Geophysical Research: Atmospheres (1984–2012)*, 102(D22):26053–26076.

Dunkerton, T. J. and Delisi, D. P. (1997). Interaction of the quasi-biennial oscillation and stratopause semiannual oscillation. *Journal of Geophysical Research: Atmospheres (1984–2012)*, 102(D22):26107–26116.

Edmon, H., Hoskins, B., and McIntyre, M. (1980). Eliassen-Palm cross sections for the troposphere. *Journal of the Atmospheric Sciences*, 37(12):2600–2616.

Ern, M. and Preusse, P. (2009). Wave fluxes of equatorial Kelvin waves and QBO zonal wind forcing derived from SABER and ECMWF temperature space-time spectra. *Atmospheric Chemistry and Physics*, 9(12):3957–3986.

Fraedrich, K. and Böttger, H. (1978). A wavenumber-frequency analysis of the 500 mb geopotential at 50 N. *Journal of the Atmospheric Sciences*, 35(4):745–750.

Fritts, D. C. and Alexander, M. J. (2003). Gravity wave dynamics and effects in the middle atmosphere. *Reviews of Geophysics*, 41(1):1003.

Fujiwara, M. and Jackson, D. (2013). SPARC Reanalysis Intercomparison Project (S-RIP) Planning Meeting 29 April–1 May, 2013, Exeter, UK. *SPARC*, page 52.

Garcia, R. R. (2000). The role of equatorial waves in the semiannual oscillation of the middle atmosphere. *Atmospheric Science across the Stratopause*, pages 161–176.

Garcia, R. R. and Boville, B. A. (1994). 'Downward control' of the mean meridional circulation and temperature distribution of the polar winter stratosphere. *Journal of the Atmospheric Sciences*, 51(15):2238–2245.

Garcia, R. R., Dunkerton, T. J., Lieberman, R. S., and Vincent, R. A. (1997). Climatology of the semiannual oscillation of the tropical middle atmosphere. *Journal of Geophysical Research: Atmospheres (1984–2012)*, 102(D22):26019–26032.

Garny, H. (2010). *Causes and impacts of changes in the stratospheric meridional circulation in a chemistry-climate model*. PhD thesis, Ludwig–Maximilian Universität München.

Garny, H., Dameris, M., and Stenke, A. (2009). Impact of prescribed SSTs on climatologies and long-term trends in CCM simulations. *Atmospheric Chemistry and Physics*, 9(16):6017–6031.

Gerber, E. P. (2012). Stratospheric versus tropospheric control of the strength and structure of the Brewer-Dobson circulation. *Journal of the Atmospheric Sciences*, 69(9):2857–2877.

Giorgetta, M., Manzini, E., Roeckner, E., Esch, M., and Bengtsson, L. (2006). Climatology and forcing of the quasi-biennial oscillation in the MAECHAM5 model. *Journal of Climate*, 19(16):3882–3901.

Giorgetta, M. A., Manzini, E., and Roeckner, E. (2002). Forcing of the quasi-biennial oscillation from a broad spectrum of atmospheric waves. *Geophysical Research Letters*, 29(8):86–1.

Goldenberg, S. B., Landsea, C. W., Mestas-Nuñez, A. M., and Gray, W. M. (2001). The recent increase in Atlantic hurricane activity: Causes and implications. *Science*, 293(5529):474–479.

Hamilton, K. (1996). Comprehensive meteorological modelling of the middle atmosphere: A tutorial review. *Journal of Atmospheric and Terrestrial Physics*, 58(14):1591–1627.

Hayashi, Y. (1971). A generalized method of resolving disturbances into progressive and retrogressive waves by space Fourier and time cross-spectral analyses. *J. Meteor. Soc. Japan*, 49:125–128.

Hayashi, Y. (1979). A generalized method of resolving transient disturbances into standing and traveling waves by space-time spectral analysis. *Journal of the Atmospheric Sciences*, 36(6):1017–1029.

Hayashi, Y. (1982). Space-time spectral analysis and its applications to atmospheric waves. *J. Meteor. Soc. Japan*, 60(1):156–171.

Hayashi, Y., Golder, D., Mahlman, J., and Miyahara, S. (1989). *The effect of horizontal resolution on gravity waves simulated by the GFDL "SKYHI" general circulation model*. Springer.

Hendon, H. H., Wheeler, M. C., and Zhang, C. (2007). Seasonal dependence of the MJO-ENSO relationship. *Journal of Climate*, 20(3):531–543.

Hines, C. O. (1997a). Doppler-spread parameterization of gravity-wave momentum deposition in the middle atmosphere. Part 1: Basic formulation. *Journal of Atmospheric and Solar-Terrestrial Physics*, 59(4):371 – 386.

Hines, C. O. (1997b). Doppler-spread parameterization of gravity-wave momentum deposition in the middle atmosphere. Part 2: Broad and quasi monochromatic spectra, and implementation. *Journal of Atmospheric and Solar-Terrestrial Physics*, 59(4):387 – 400.

Hirota, I. (1978). Equatorial waves in the upper stratosphere and mesosphere in relation to the semiannual oscillation of the zonal wind. *Journal of the Atmospheric Sciences*, 35(4):714–722.

Hirota, I. (1980). Observational evidence of the semiannual oscillation in the tropical middle atmosphere—a review. *Pure and Applied Geophysics*, 118(1):217–238.

Hitchman, M. H., Gille, J. C., Rodgers, C. D., and Brasseur, G. (1989). The separated polar winter stratopause: A gravity wave driven climatological feature. *Journal of the atmospheric sciences*, 46(3):410–422.

Holton, J. R. (1973). On the frequency distribution of atmospheric Kelvin waves. *Journal of the Atmospheric Sciences*, 30(3):499–501.

Holton, J. R. (1975). The dynamic meteorology of the stratosphere and mesosphere. In *Research supported by the National Science Foundation Boston, American Meteorological Society (Meteorological Monograph. Volume 15, No. 37), 1975. 224 p*, volume 15.

Holton, J. R. (1984). The generation of mesospheric planetary waves by zonally asymmetric gravity wave breaking. *Journal of the atmospheric sciences*, 41(23):3427–3430.

Holton, J. R., Curry, J. A., and Pyle, J. A. (2003). *Encyclopedia of atmospheric sciences*, volume 1. Academic Press.

Holton, J. R. and Hakim, G. J. (2013). *An introduction to dynamic meteorology*. Academic press.

Holton, J. R. and Mass, C. (1976). Stratospheric vacillation cycles. *Journal of the Atmospheric Sciences*, 33(11):2218–2225.

Holton, J. R. and Tan, H.-C. (1980). The influence of the equatorial quasi-biennial oscillation on the global circulation at 50 mb. *Journal of the Atmospheric Sciences*, 37(10):2200–2208.

Holton, J. R. and Wehrbein, W. M. (1980). A numerical model of the zonal mean circulation of the middle atmosphere. *Pure and Applied Geophysics*, 118(1):284–306.

Hurrell, J. W., Hack, J. J., Shea, D., Caron, J. M., and Rosinski, J. (2008). A new sea surface temperature and sea ice boundary dataset for the Community Atmosphere Model. *Journal of Climate*, 21(19):5145–5153.

Hurwitz, M., Newman, P., Li, F., Oman, L., Morgenstern, O., Braesicke, P., and Pyle, J. (2010). Assessment of the breakup of the Antarctic polar vortex in two new chemistry-climate models. *Journal of Geophysical Research: Atmospheres (1984–2012)*, 115(D7).

IPCC (2007). IPCC, 2007: Climate change 2007: The physical science basis. *Contribution of Working Group I to the fourth assessment report of the Intergovernmental Panel on Climate Change*, edited by: Solomon, S., Qin, D., Manning, M., Chen, Z., Marquis, M., Averyt, K.B., Tignor, M. and Miller, H.L.

Jöckel, P., Kerkweg, A., Pozzer, A., Sander, R., Tost, H., Riede, H., Baumgärtner, A., Gromov, S., and Kern, B. (2010). Development cycle 2 of the Modular Earth Submodel System (MESSy2). *Geoscientific Model Development*, 3(2):717–752.

Jungclaus, J. H., Fischer, N., Haak, H., Lohmann, K., Marotzke, J., Matei, D., Mikolajewicz, U., Notz, D., and von Storch, J. S. (2013). Characteristics of the ocean simulations in the Max Planck Institute Ocean Model (MPIOM) the ocean component of the MPI-Earth system model. *Journal of Advances in Modeling Earth Systems*, 5(2):422–446.

Kao, S. (1968). Governing equations and spectra for atmospheric motion and transports in frequency, wave-number space. *Journal of the Atmospheric Sciences*, 25(1):32–38.

Kao, S. (1970). Wavenumber-frequency spectra of temperature in the free atmosphere. *Journal of the Atmospheric Sciences*, 27(7):1000–1007.

Kasahara, A. (1980). Effect of zonal flows on the free oscillations of a barotropic atmosphere. *Journal of the Atmospheric Sciences*, 37(5):917–929.

Kawatani, Y., Watanabe, S., Sato, K., Dunkerton, T. J., Miyahara, S., and Takahashi, M. (2010a). The roles of equatorial trapped waves and internal inertia-gravity waves in driving the quasi-biennial oscillation. Part I: Zonal mean wave forcing. *Journal of the Atmospheric Sciences*, 67(4):963–980.

Kawatani, Y., Watanabe, S., Sato, K., Dunkerton, T. J., Miyahara, S., and Takahashi, M. (2010b). The roles of equatorial trapped waves and internal inertia-gravity waves in driving the quasi-biennial oscillation. Part II: Three-dimensional distribution of wave forcing. *Journal of the Atmospheric Sciences*, 67(4):981–997.

Kerkweg, A. and Jöckel, P. (2012). The 1-way on-line coupled atmospheric chemistry model system MECO (n)–Part 1: Description of the limited-area atmospheric chemistry model COSMO/MESSy. *Geoscientific Model Development*, 5(1):87–110.

Kern, B. (2013). *Chemical interaction between ocean and atmosphere*. PhD thesis, Johannes Gutenberg-Universität Mainz.

Khosrawi, F., Müller, R., Proffitt, M. H., Ruhnke, R., Kirner, O., Jöckel, P., Grooß, J.-U., Urban, J., Murtagh, D., and Nakajima, H. (2009). Evaluation of CLaMS, KASI-MA and ECHAM5/MESSy1 simulations in the lower stratosphere using observations of Odin/SMR and ILAS/ILAS-II. *Atmospheric Chemistry and Physics*, 9(15):5759–5783.

Kobayashi, S., Ota, Y., and Harada, Y. (2015). The JRA-55 Reanalysis: General specifications and basic characteristics. *Journal of the Meteorological Society of Japan*, 93(1):5–48.

Labitzke, K. (1972). Temperature changes in the mesosphere and stratosphere connected with circulation changes in winter. *Journal of the Atmospheric Sciences*, 29(4):756–766.

Limpasuvan, V., Richter, J. H., Orsolini, Y. J., Stordal, F., and Kvissel, O.-K. (2012). The roles of planetary and gravity waves during a major stratospheric sudden warming as characterized in WACCM. *Journal of Atmospheric and Solar-Terrestrial Physics*, 78:84–98.

Limpasuvan, V., Wu, D. L., Joan Alexander, M., Xue, M., Hu, M., Pawson, S., and Perkins, J. R. (2007). Stratospheric gravity wave simulation over Greenland during 24 January 2005. *Journal of Geophysical Research: Atmospheres (1984–2012)*, 112(D10).

Lindzen, R. D. (1967). Planetary waves on beta-planes. *Monthly Weather Review*, 95(7):441–451.

Lindzen, R. S. and Holton, J. R. (1968). A theory of the quasi-biennial oscillation. *Journal of the Atmospheric Sciences*, 25(6):1095–1107.

Lindzen, R. S. and Matsuno, T. (1968). On the nature of large scale wave disturbances in the equatorial lower stratosphere. *J. Meteor. Soc. Japan*, 46:215–221.

Mager, F. (2004). *Untersuchung der Anregung und Ausbreitung planetarer Wellen in meteorologischen Analysen und einem Klima-Chemie-Modell*. PhD thesis, Bergische Universität Wuppertal, Fachbereich Physik.

Maier-Reimer, E., Kriest, I., Segschneider, J., and Wetzel, P. (2005). The hamburg ocean carbon cycle model hamocc5. 1-technical description release 1.1.

Manzini, E. and McFarlane, N. A. (1998). The effect of varying the source spectrum of a gravity wave parameterization in a middle atmosphere general circulation model. *Journal of Geophysical Research: Atmospheres*, 103(D24):31523–31539.

Marsland, S., Haak, H., Jungclaus, J., Latif, M., and Röske, F. (2003). The Max-Planck-Institute global ocean/sea ice model with orthogonal curvilinear coordinates. *Ocean modelling*, 5(2):91–127.

Matsuno, T. (1966). Quasi-geostrophic motions in the equatorial area. *J. Meteor. Soc. Japan*, 44(1):25–43.

Mauritsen, T., Stevens, B., Roeckner, E., Crueger, T., Esch, M., Giorgi, M., Haak, H., Jungclaus, J., Klocke, D., Matei, D., et al. (2012). Tuning the climate of a global model. *Journal of Advances in Modeling Earth Systems*, 4(3).

Mayr, H., Mengel, J., Chan, K., and Huang, F. (2010). Middle atmosphere dynamics with gravity wave interactions in the numerical spectral model: Zonal-mean variations. *Journal of Atmospheric and Solar-Terrestrial Physics*, 72(11):807–828.

McFarlane, N. and Manzini, E. (1997). Parameterization of gravity wave drag in comprehensive models of the middle atmosphere. *Advances in Space Research*, 20(6):1241–1251.

McLandress, C. and McFarlane, N. (1993). Interactions between orographic gravity wave drag and forced stationary planetary waves in the winter Northern Hemisphere middle atmosphere. *Journal of the Atmospheric Sciences*, 50(13):1966–1990.

McLandress, C. and Scinocca, J. F. (2005). The GCM response to current parameterizations of nonorographic gravity wave drag. *Journal of the Atmospheric Sciences*, 62(7):2394–2413.

Miralles, D. G., Teuling, A. J., van Heerwaarden, C. C., and de Arellano, J. V.-G. (2014). Mega-heatwave temperatures due to combined soil desiccation and atmospheric heat accumulation. *Nature Geoscience*, 7(5):345–349.

Mitchell, D. M., Gray, L. J., Fujiwara, M., Hibino, T., Anstey, J. A., Ebisuzaki, W., Harada, Y., Long, C., Misios, S., Stott, P. A., and Tan, D. (2014). Signatures of naturally induced variability in the atmosphere using multiple reanalysis datasets. *Quarterly Journal of the Royal Meteorological Society*, 10.1002/qj.2492.

Monitor, D. (2014). Drought monitor: state-of-the-art blend of science and subjectivity.

Newman, P. A., Nash, E. R., and Rosenfield, J. E. (2001). What controls the temperature of the Arctic stratosphere during the spring? *Journal of Geophysical Research: Atmospheres (1984–2012)*, 106(D17):19999–20010.

Orr, A., Bechtold, P., Scinocca, J., Ern, M., and Janiskova, M. (2010). Improved middle atmosphere climate and forecasts in the ECMWF model through a nonorographic gravity wave drag parameterization. *Journal of Climate*, 23(22):5905–5926.

Paul, J., Fortuin, F., and Kelder, H. (1998). An ozone climatology based on ozonesonde and satellite measurements. *Journal of Geophysical Research: Atmospheres (1984–2012)*, 103(D24):31709–31734.

Pawson, S., Kodera, K., Hamilton, K., Shepherd, T., Beagley, S., Boville, B., Farrara, J., Fairlie, T., Kitoh, A., Lahoz, W., et al. (2000). The GCM-Reality Intercomparison Project for SPARC (GRIPS): Scientific issues and initial results. *Bulletin of the American Meteorological Society*, 81(4):781–796.

Plumb, R. (1982). The circulation of the middle atmosphere. *Australian Meteorological Magazine*, 30(1):1961.

Pohlmann, H., Müller, W., Kulkarni, K., Kameswarao, M., Matei, D., Vamborg, F., Kadow, C., Illing, S., and Marotzke, J. (2013). Improved forecast skill in the tropics in the new MiKlip decadal climate predictions. *Geophysical Research Letters*, 40(21):5798–5802.

Pratt, R. W. (1976). The interpretation of space-time spectral quantities. *Journal of the Atmospheric Sciences*, 33(6):1060–1066.

Raddatz, T. J., Reick, C. H., Knorr, W., Kattge, J., Roeckner, E., Schnur, R., Schnitzler, K.-G., and P. Wetzel, J. J. (2007). Will the tropical land biosphere dominate the climate-carbon cycle feedback during the twenty-first century? *Climate Dynamics*, 29:565 – 574.

Ray, E. A., Alexander, M. J., and Holton, J. R. (1998). An analysis of the structure and forcing of the equatorial semiannual oscillation in zonal wind. *Journal of Geophysical Research: Atmospheres (1984–2012)*, 103(D2):1759–1774.

Rayner, N., Parker, D. E., Horton, E., Folland, C., Alexander, L., Rowell, D., Kent, E., and Kaplan, A. (2003). Global analyses of sea surface temperature, sea ice, and night marine air temperature since the late nineteenth century. *Journal of Geophysical Research: Atmospheres (1984–2012)*, 108(D14).

Reed, R. J. (1965). The quasi-biennial oscillation of the atmosphere between 30 and 50 km over Ascension Island. *Journal of the Atmospheric Sciences*, 22(3):331–333.

Reick, C. H., Raddatz, T., Brovkin, V., and Gayler, V. (2013). Representation of natural and anthropogenic land cover change in MPI-ESM. *Journal of Advances in Modeling Earth Systems*, 5(3):459–482.

Richter, J. H. and Garcia, R. R. (2006). On the forcing of the Mesospheric Semi-Annual Oscillation in the Whole Atmosphere Community Climate Model. *Geophysical research letters*, 33(1).

Rienecker, M. M., Suarez, M. J., Gelaro, R., Todling, R., Bacmeister, J., Liu, E., Bosilovich, M. G., Schubert, S. D., Takacs, L., Kim, G.-K., et al. (2011). MERRA: NASA’s modern-era retrospective analysis for research and applications. *Journal of Climate*, 24(14):3624–3648.

Righi, M., Eyring, V., Gottschaldt, K.-D., Klinger, C., Frank, F., Jöckel, P., and Cionni, I. (2014). Quantitative evaluation of ozone and selected climate parameters in a set of EMAC simulations. *Geoscientific Model Development Discussions*, 7(5):6549–6627.

Roeckner, E., Bäumle, G., Bonaventura, L., Brokopf, R., Esch, M., Giorgetta, M., Hagemann, S., Kirchner, I., Kornblueh, L., Manzini, E., Rhodin, A., Schlese, U., Schulzweida, U., and Tompkins, A. (2003). *The atmospheric general circulation model ECHAM5: Part 1. Model description*, volume 349. Max-Planck-Institut für Meteorologie.

Roeckner, E., Brokopf, R., Esch, M., Giorgi, M., Hagemann, S., Kornblueh, L., Manzini, E., Schlese, U., and Schukzweida, U. (2006). Sensitivity of simulated climate to horizontal and vertical resolution in the ECHAM5 atmosphere model. *Journal of Climate*, 19(16):3771–3791.

Roff, G., Thompson, D. W., and Hendon, H. (2011). Does increasing model stratospheric resolution improve extended-range forecast skill? *Geophysical Research Letters*, 38(5).

Runde, T. (2012). *Ursachen und Wirkung der dynamischen Kopplung von Stratosphäre und Troposphäre*. PhD thesis, Ludwig–Maximilian Universität München.

Sassi, F. and Garcia, R. R. (1997). The role of equatorial waves forced by convection in the tropical semiannual oscillation. *Journal of the atmospheric sciences*, 54(15):1925–1942.

Scaife, A., Arribas, A., Blockley, E., Brookshaw, A., Clark, R., Dunstone, N., Eade, R., Fereday, D., Folland, C., Gordon, M., et al. (2014). Skillful long-range prediction of european and north american winters. *Geophysical Research Letters*, 41(7):2514–2519.

Scott, R. and Haynes, P. (2000). Internal vacillations in stratosphere-only models. *Journal of the atmospheric sciences*, 57(19):3233–3250.

Shaw, T. A. and Shepherd, T. G. (2007). Angular momentum conservation and gravity wave drag parameterization: Implications for climate models. *Journal of the atmospheric sciences*, 64(1):190–203.

Shepherd, T. (2006). Can we trust the simulated gravity–wave response to climate change?

Sigmond, M., Scinocca, J., Kharin, V., and Shepherd, T. (2013). Enhanced seasonal forecast skill following stratospheric sudden warmings. *Nature Geoscience*, 6(2):98–102.

Smith, D. M., Scaife, A. A., and Kirtman, B. P. (2012). What is the current state of scientific knowledge with regard to seasonal and decadal forecasting. *Environ. Res. Lett*, 7(015,602).

Stenke, A., Grewe, V., and Ponater, M. (2008). Lagrangian transport of water vapor and cloud water in the ECHAM4 GCM and its impact on the cold bias. *Climate dynamics*, 31(5):491–506.

Stevens, B., Giorgi, M., Esch, M., Mauritsen, T., Crueger, T., Rast, S., Salzmann, M., Schmidt, H., Bader, J., Block, K., Brokopf, R., Fast, I., Kinne, S., Kornblueh, L., Lohmann, U., Pincus, R., Reichler, T., and Roeckner, E. (2013). Atmospheric component of the MPI-M Earth System Model: ECHAM6. *Journal of Advances in Modeling Earth Systems*, 5(2):146–172.

Sundqvist, H. (1978). A parameterization scheme for non-convective condensation including prediction of cloud water content. *Quarterly Journal of the Royal Meteorological Society*, 104(441):677–690.

Sundqvist, H., Berge, E., and Kristjánsson, J. E. (1989). Condensation and cloud parameterization studies with a mesoscale numerical weather prediction model. *Monthly Weather Review*, 117(8):1641–1657.

Svoboda, M., LeComte, D., Hayes, M., Heim, R., Gleason, K., Angel, J., Rippey, B., Tinker, R., Palecki, M., Stooksbury, D., et al. (2002). The drought monitor. *Bulletin of the American Meteorological Society*, 83(8):1181–1190.

Taylor, K. E., Stouffer, R. J., and Meehl, G. A. (2012). An overview of CMIP5 and the experiment design. *Bulletin of the American Meteorological Society*, 93(4):485–498.

Tiedtke, M. (1989). A Comprehensive Mass Flux Scheme for Cumulus Parameterization in Large-Scale Models. *Monthly Weather Review*, 117(8):1779–1800.

Uppala, S. M., Källberg, P., Simmons, A., Andrae, U., Bechtold, V., Fiorino, M., Gibson, J., Haseler, J., Hernandez, A., Kelly, G., et al. (2005). The ERA-40 re-analysis. *Quarterly Journal of the Royal Meteorological Society*, 131(612):2961–3012.

Valcke, S., Caubel, A., Declat, D., and Terray, L. (2003). Oasis3 ocean atmosphere sea ice soil user's guide. *Prism project report*, 2.

Vamborg, F. S. E., Brovkin, V., and Claussen, M. (2011). The effect of a dynamic background albedo scheme on Sahel/Sahara precipitation during the mid-Holocene. *Climate of the Past*, 7(1):117–131.

Von Storch, H. and Zwiers, F. W. (2001). *Statistical analysis in climate research*. Cambridge university press.

Warner, R. M. (1998). *Spectral analysis of time-series data*. Guilford Press.

Weber, M., Dikty, S., Burrows, J. P., Garny, H., Dameris, M., Kubin, A., Abalichin, J., and Langematz, U. (2011). The Brewer-Dobson circulation and total ozone from seasonal to decadal time scales. *Atmospheric Chemistry and Physics*, 11(21):11221–11235.

Wheeler, M. and Kiladis, G. N. (1999). Convectively coupled equatorial waves: Analysis of clouds and temperature in the wavenumber-frequency domain. *Journal of the Atmospheric Sciences*, 56(3):374–399.

Yoden, S., Taguchi, M., and Naito, Y. (2002). Numerical studies on time variations of the troposphere-stratosphere coupled system. *Journal of the Meteorological Society of Japan*, 80(4B):811–830.

Zangvil, A. (1977). On the presentation and interpretation of spectra of large-scale disturbances. *Monthly Weather Review*, 105(11):1469–1472.



# Danksagung

An erster Stelle danke ich herzlichst meinem Betreuer und Mentor Prof. Dr. Martin Dameris, der mich trotz meiner Eigenheiten und gelegentlicher Authoritätsproblemen akzeptierte und mich stets unterstützte. Er gab mir jegliche Freiheiten meinen wissenschaftlichen Interessen nachzugehen und begleitete mich mit vollem Elan durch Höhen und Tiefen meiner Promotionszeit.

Prof. Dr. Bernhard Mayer möchte ich für die Übernahme des Zweitgutachtens und der damit verbundenen Arbeit, Zeit und vorbereitenden Gesprächen danken.

Bedanken möchte ich mich bei Institutsdirektor Prof. Dr. Markus Rapp für die Möglichkeit diese Arbeit am Institut für Physik der Atmosphäre des DLR anzufertigen.

Zu ausgesprochen großem Dank bin ich Hella Garry verpflichtet, die mir stets mit großer Geduld und Passion bei jeglichen wissenschaftlichen, wie auch technischen Fragen zur Seite stand und sich immer für meine Arbeit interessierte.

Patrick Jöckel danke ich für seine unermüdliche Unterstützung hinsichtlich des EMAC Modellsystems.

Felix Bunzel danke ich für die Unterstützung zu den TEM-Diagnostiken.

Winfried Beer danke ich für verlässlichen, ausgezeichneten, hervorragenden IT support. Meinem langjährigen Bürokollegen, -mitbewohner und -freund Phoebe Graf möchte ich für die schöne Zeit danken.

Hiroshi Yamashita danke ich für sein offenes Ohr zu jeglichen Belangen.

Den Kollegen Roland Eichinger, Lisa Bock, Bastian Kern, Katrin Dahlmann, Chris Kaiser, Andreas Pfeifer, Sabine Brinkop, Theresa Runde und Rudi Deckert möchte ich für deren Unterstützung und hilfreiche Diskussionen jeglicher Art danken!

Anne Kubin danke ich für die gute Zusammenarbeit im MiKlip Projekt, sowie für die kritischen und hilfreichen Kommentare zu meiner Arbeit.

Thank you so much Steven, providing the perspective of a native speaker.  
Danke Dave, Besch, Katrin, Lieserl, allen Omas und Opas für das Bespaßen der Kinder und die Unterstützung!

Danke Mino! Danke Yoshi! Danke Amely!